

RADIATION FROM EXTREME SOURCES: STUDYING ULTRA-HIGH DOSE RATE
RADIOBIOLOGY WITH LASER-DRIVEN ION ACCELERATORS

By

Jared De Chant

A DISSERTATION

Submitted to
Michigan State University
in partial fulfillment of the requirements
for the degree of

Physics — Doctor of Philosophy

2025

ABSTRACT

Advances in laser-plasma acceleration have enabled the generation of intense ion beams from compact, table-top laser systems. These laser-driven ion accelerators (LDIAs) can produce high intensity proton pulses with ultra-short duration and extremely high dose rates, presenting new opportunities for radiobiological research in previously inaccessible regimes. This thesis investigates the use of LDIA as novel radiation sources for studying ultra-high dose rate radiobiology, with a focus on enabling controlled, repeatable investigations into the FLASH effect—a phenomenon where radiation delivered at dose rates exceeding 40 Gy/s appears to spare normal tissue while maintaining tumor control.

A major component of this work is the design, simulation, and experimental implementation of compact, permanent magnet-based beam transport systems for LDIA-generated protons at the BELLA iP2 beamline at the Lawrence Berkeley National Laboratory. These transport systems address the challenges posed by the large divergence and broad energy spectra of LDIA beams, enabling efficient delivery of high-intensity proton beams to biological targets. Multiple exposure platforms, including both LDIA and conventional sources, were established and characterized across the laboratory to support interdisciplinary radiobiological experiments. Significant work on dosimetry was done to verify the doses delivered to biological samples exposed at these sources through Monte Carlo modeling and the use of radiochromic film.

Through this integration of high power lasers, accelerator physics, and radiobiology, the work presented here establishes new capabilities for investigating dose delivery, beam quality, and biological responses in the ultra-high dose rate regime. The results support the viability of LDIA as a research tool for advancing the understanding of the FLASH effect and exploring the future of compact, high-impact radiotherapy platforms.

TABLE OF CONTENTS

Chapter 1. Introduction	1
1.1 Motivation	1
1.2 Overview of content	4
 Chapter 2. Theory	 8
2.1 Laser-driven ion acceleration	8
2.1.1 Target Normal Sheath Acceleration (TNSA)	9
2.1.2 Other acceleration mechanisms	12
2.2 Ion beam transport and delivery	15
2.2.1 Curvilinear coordinates	15
2.2.2 Transport maps	17
2.2.3 Magnetic optics	18
2.3 Radiation transport in matter	19
2.3.1 X-ray absorption and attenuation in matter	20
2.3.2 Stopping power and linear-energy transfer (LET) of massive particles	22
2.3.3 Monte Carlo radiation transport	25
 Chapter 3. Exploring the extremes of radiobiology across different modalities and exposure environments	 28
3.1 Introduction to radiation therapy	28
3.1.1 The FLASH effect	29
3.2 Dosimetry methods	30
3.2.1 Radiochromic film	31
3.3 Characterizing exposure environments for radiobiology research	34
3.3.1 X-ray tube (X-RAD320) for reference dosimetry and low dose detection	34
3.3.2 Synchrotron radiation at the Advanced Light Source (ALS)	36
3.3.2.1 ALS Beamline 3.2.1	37
3.3.2.2 ALS Beamline 3.3.1	42
3.3.3 Laser driven proton beams	44
 Chapter 4. Modeling and design of compact permanent magnet-based transport systems for laser driven ion acceleration	 45
4.1 Permanent magnet-based optical elements	45
4.1.1 Permanent magnet quadrupoles (PMQ)	47
4.1.2 Permanent Magnet Dipoles	48
4.2 Transport design and simulation methodology	50
4.2.1 COSY INFINITY	50
4.2.2 Monte Carlo-based radiation transport and particle tracking	51
4.2.3 Input beam parameters	52
4.3 Beam transport designs for applications of LDIA	54
4.3.1 Configuration design and performance	54
4.3.1.1 Doublet	54

4.3.1.2	Triplet configuration improves beam size symmetry	58
4.3.1.3	Improving magnification symmetry of the transport system with a quartet configuration	60
4.3.1.4	Mirrored design for 1 to 1 imaging	63
4.3.2	Controlling energy spread	63
4.4	10 and 30 MeV Collimator designs for radiobiology at iP2	66
4.5	Discussion	69
Chapter 5. Implementation of beam transport for laser driven ion acceleration at the BELLA Center		71
5.1	The BELLA PetaWatt (PW) laser system	74
5.1.1	High intensity beamline and target chamber, iP2	74
5.2	Experimental setup and beam transport	75
5.2.1	Magnet characterization and installation	77
5.3	Beam transport performance	79
5.3.1	Improved charge collection	80
5.3.2	Uniform beam profile	82
5.4	Dosimetry of laser-driven protons for <i>in vivo</i> samples	86
5.4.1	Online dose monitoring with an Integrating Current Transformer	86
5.4.2	Absolute dosimetry using radiochromic film	88
5.5	Biological results	93
5.6	Discussion	96
Chapter 6. Conclusion		97
BIBLIOGRAPHY		99

Chapter 1. Introduction

1.1 Motivation

The goal of this work is to more effectively deliver radiation from extreme sources to biological samples in order to explore novel forms of radiotherapy, specifically by leveraging laser-driven ion acceleration. Radiotherapy (RT), the use of ionizing radiation to kill or control the growth of malignant cells, is the standard of care for over half of all cancer patients [1, 2]. The radiation is either generated by radioactive material inserted inside the patient body, such as in brachytherapy, or by accelerating charged particles (e.g. electrons, protons, and ions) to high energy and focusing them into beams to be delivered to the patient body, as in external beam radiotherapy (EBRT). Particle accelerators of all types have been used in the past to generate these beams while the most commonly used today are linear accelerators (LINACs) for accelerating electrons and cyclotrons for protons/ions. Over the past century, advances in RT—such as Intensity Modulated Radiotherapy (IMRT) and Computed Tomography (CT) guided radiotherapy—have significantly improved treatment precision and outcomes [3, 4].

Despite these advancements, conventional radiotherapy is constrained by two major challenges. First, the collateral damage to surrounding healthy tissues limits the total dose that can be safely delivered, often leading to late-onset toxicity and radiation-induced secondary cancers, particularly in pediatric patients. Second, conventional external beam sources require large and expensive particle accelerators, which are not only over-subscribed for clinical use but are also designed for current clinical standards, making them unsuitable or inaccessible for research into novel techniques [5].

Laser-driven ion acceleration (LDIA) offers a way to address both challenges. In LDIA,

a high intensity laser pulse ($> 10^{19}$ W/cm²) interacts with a thin solid target and generates a plasma that can sustain high accelerating gradients (10s-1000s GeV/cm) [6, 7]. A large number of ions can be accelerated in these fields to very high energies over short distances (sub mm) through various different mechanisms. Conventional radio frequency (RF) accelerators are limited to accelerating gradients of ~ 100 MV/m as voltages higher than this will cause electrical breakdown, i.e. electrons will be extracted from the accelerating structure's walls, disrupting the acceleration field.

In contrast, LDIA systems are compact and cost-effective, representing a dramatic reduction in the size and infrastructure required to accelerate particles to the same energies. This compactness can provide broader access for users of research accelerators as they can be set up in smaller labs. Thus, LDIA is uniquely suited for both laboratory-based research in radiotherapy and potentially clinical use, addressing the critical issue of accessibility [8, 9, 10, 11].

This acceleration technique further stands out from its more conventional counterparts due to its high ion production ($\sim 10^{13}$ ions per shot) and ultra short bunch length (\sim ps at the source). With these advantages, LDIA systems can deliver radiation to biological tissue at dose rates ($> 10^7$ Gy/s) much higher than those used in clinical practice and thus are well suited to explore this previously inaccessible ultra-high dose rate regime. These systems are also well suited to be used in other applications in the fields of material science [12] and warm dense matter physics [13, 14, 15].

The use of ultra-high dose rates in radiotherapy has garnered significant attention in the larger community due to the FLASH effect which refers to the remarkable ability of ultra-high dose rate radiation to selectively spare normal (healthy) tissues while maintaining the effectiveness of tumor control [16, 17]. Put another way, delivering the same amount of radiation (dose), but over a shorter time, appears to reduce the damage to healthy tissue but

not to cancerous tissue. This effect is significant as it could be used to minimize the harmful side effects of conventional radiotherapy while improving patient outcomes, representing a promising breakthrough in cancer treatment [18]. While FLASH RT has become a hot topic[19], with numerous publications coming out each year, the exact mechanism behind this phenomenon is not well understood. This is in part due to the lack of facilities that are capable and available to explore this high dose rate regime mentioned previously.

Researchers at the Lawrence Berkeley National Laboratory (LBNL) in Berkeley, CA are among those interested in studying this effect. An interdisciplinary group composed of researchers at the Berkeley Lab Laser Accelerator (BELLA) Center, the Advanced Light Source (ALS), and the BioSciences Area (BSA) have come together to investigate this at LBNL. In collaboration with this effort, this work aims to characterize, establish, and enhance exposure environments at LBNL for studying this high dose rate regime with the use of both novel sources and more conventional sources.

The BELLA Center has a long history of using high power, short pulse lasers to explore advanced accelerator techniques. The BELLA PetaWatt (PW) laser [20] has been used to set records in multi-GeV laser plasma acceleration (LPA) of electron beams [21, 22]. Much of the work presented here was done at the recently commissioned short focal length laser beamline and test chamber, known as BELLA iP2, dedicated to exploring advanced laser-driven ion acceleration and high energy density science and applications (HEDSA) [23, 24, 25].

To utilize the LDIA at BELLA iP2 for radiotherapy, the beams must be efficiently collected and transported to the sample location while maintaining their high intensity to achieve a high dose rate and uniform beam profile. This is challenging due to the high initial divergence and broadband energy spread of the LD beams. Presented as a large part of this work is an attempt to address this challenge through the design, simulation, and im-

plementation of compact, permanent magnet-based beam transport systems used to deliver LDIA proton beams generated at BELLA iP2 to *in vivo* biological samples. These beam transport systems were used in multiple recent experiments to explore ultra-high dose rate radiobiology.

By coupling the multiple accelerator capabilities at LBNL with state-of-the-art biological research, this work aims to establish new platforms to study ultra-high dose rate radiobiology and advance the understanding of the FLASH effect and its potential applications in cancer treatment research. Specifically, this work establishes the ability of BELLA iP2 to produce high intensity, controlled laser-driven ion beams to open new opportunities for investigating dose delivery, beam quality, and radiobiological responses at ultra-high dose rates.

1.2 Overview of content

This thesis presents an interdisciplinary investigation into the application of laser-driven ion acceleration for ultra-high dose rate radiobiology, with a particular focus on enabling and studying the FLASH effect. The work integrates advancements in laser-plasma acceleration, beam transport design, and radiobiological experimentation to address key challenges in modern research in radiotherapy. The experimental work was primarily performed at the BELLA Center's PW laser system [20] and its iP2 beamline at LBNL [24]. Following the theory laid out in Chapter 2 that underlies it, the rest of the work will be presented as follows:

Chapter 3: Exploring the extremes of radiobiology across different modalities and exposure environments

This chapter gives further background on the field of radiobiology and serves as an overview of the use of particle accelerators in cancer treatment while establishing the platforms and tools used in later work. There is a long history of radiation therapy research, specifically at the Lawrence Berkeley National Laboratory (LBNL). The 184-inch cyclotron at LBNL was the site of the first use of protons beams in cancer treatment back in 1958, work led by John H. Lawrence, the brother of the founder Ernest O. Lawrence [26]. Radiobiology research continues at LBNL with evermore sophisticated radiation sources. Presented here is the work to establish these new radiation sources (or exposure environments) to serve as platforms for radiobiological research. This includes characterizing and performing dosimetry on multiple exposure environments at LBNL including the Advanced Light Source's 3.2.1 and 3.3.1 beamlines. Due to the differences between the exposure environments, such as the particle type and energy spectrum, dosimetry has to be performed specifically in each environment before they can be used for research purposes. This work was vital for using these platforms to study dose rate effects on oxidative damage to peptides [27] and the long-term effects of low-dose ionizing radiation exposure [28]. This chapter will also introduce the dosimetry techniques used in establishing these exposure environments.

Chapter 4: Modeling and design of compact permanent magnet-based transport systems for laser driven ion acceleration

For any application utilizing LD ion beams, a beam transport system is required to collect and deliver the beam to a specific sample. While they are generated from a micron-scale

source, the large divergence and energy spread of LD ion beams present a unique challenge to transporting them compared to beams from conventional accelerators. This chapter gives an overview of proposed compact transport designs using permanent magnets satisfying different requirements depending on the application for the iP2 proton beamline such as radiation biology, material science, and high energy density science. These designs are optimized for different parameters such as energy spread and peak proton density according to the applications need. The various designs consist solely of permanent magnet elements, which can provide high magnetic field gradients on a small footprint. While the field strengths are fixed, we have shown that the beam size is able to be tuned effectively by varying the placement of the magnets. The performance of each design was evaluated based on high order particle tracking simulations of typical LD proton beams. We also examine the ability of certain configurations to tune and select beam energies, critical for specific applications. A more detailed investigation was carried out for a design to deliver 10 MeV LD accelerated ions for radiation biology applications.

Chapter 5: Implementation of beam transport for laser driven ion acceleration at the BELLA Center

At the BELLA Center's iP2 beamline, we implemented two compact, permanent magnet-based beam transport configurations for delivering 10 or 30 MeV protons to a biological sample. The beam transports were used in two radiobiological experiments to study the radiation damage to both normal tissue *in vivo* and peptides with laser-driven protons at ultra-high instantaneous dose rates. With the transports installed, the BELLA iP2 beamline was able to deliver significantly more charge to the samples, increasing the dose per shot and minimizing the total exposure time required. The transports also effectively delivered

a uniform dose over the samples. This chapter will give an overview of the setup of these experiments, the installation of the beam transports, and the work done to characterize their performance.

Concurrently, we implemented a suite of diagnostics used for dosimetry including multiple integrating current transformers (ICTs) for indirect, online dose monitoring and calibrated radiochromic films (RCFs) to record the absorbed dose and profile. Monte-Carlo (MC) simulations of the beamline allow us to predict the dose received by the sample and correct the linear energy transfer (LET)-dependent response of the RCFs. This chapter not only further establishes the practicality of utilizing LDIA for radiobiological research but also highlights the BELLA Center's capability to accommodate further experiments in this domain.

Chapter 2. Theory

This work spans multiple distinct disciplines of physics and biology and stands at the intersection of lasers, plasmas, and accelerators. There is a significant body of work on the theory behind each of these fields. Presented here is a subset that is relevant to the use of laser driven ion beams in biological research. The basic process of using laser driven ion beams for radiotherapy is described as follows:

First, a large number of ions are accelerated in the electromagnetic fields generated in a plasma created by the interaction between a high intensity laser and solid target. This collection of ions are then collected and focused into a beam by a carefully designed arrangement of magnetic fields in the beam transport system. The ion beam propagates toward a biological sample and the constituent particles deposit their kinetic energy as dose as the particles interact with the matter in the sample.

This chapter aims to mathematically describe the motion of these particles and relevant physics at each stage of this process.

2.1 Laser-driven ion acceleration

Laser-driven ion acceleration has become a very attractive area of research due to the unique properties of the ion beams generated being particularly relevant to a variety of applications. Compared to conventional radio-frequency (RF) accelerators, laser-driven ion beams exhibit unique properties, including a large number of protons per shot (10^{13} /shot), a low emittance (< 0.1 mm mrad), and an ultra-short pulse duration (10^{-12} s at the source) [6, 7].

A significant advantage of laser-ion accelerators is their large accelerating gradient which is four orders of magnitude greater than in a traditional RF cavity (10^6 MV/m vs. 10^2 MV/m).

The large accelerating gradient allows ions to be accelerated to a higher energy over a shorter distance. This property makes such accelerators advantageous for applications that need to be compact and can provide broader access for users of research accelerators as they can be set up in smaller labs. The ultra-short pulse duration and high energy density of laser-driven ion beams also makes them suitable for ultra high dose-rate radiobiological studies related to cancer therapy [9, 29, 30]. Other applications can be found in the fields of material science [12] and warm dense matter physics [13, 10, 14].

The laser acceleration of ions from solid targets is a complicated, multidimensional process involving relativistic effects, non-linearities, and collective and kinetic effects.

While there are multiple ion acceleration mechanisms that have been explored, this work will focus on Target Normal Sheath Acceleration (TNSA) as it poses less stringent requirements to laser and target conditions than the other mechanisms and thus is the most dominant mechanism demonstrated experimentally. Theoretical methods for the various physical mechanisms involved in TNSA range from analytical approaches [31, 32] for simplified scenarios over fluid models up to fully relativistic, collisional three-dimensional computer simulations. Crucial features such as the maximum ion energy, as well as the maximum ion energy, can be obtained analytically, but a full dynamic description of the process has to be obtained numerically.

2.1.1 Target Normal Sheath Acceleration (TNSA)

When an ultra-intense laser pulse (intensity $I > 10^{18}$ W/cm²) strikes a solid target, it drives a violent laser-plasma interaction at the front surface. A significant fraction of the laser energy is absorbed by target electrons via mechanisms such as $J \times B$ heating, producing a population of hot electrons with quasi-Maxwellian energies (typically in the MeV range). These hot

electrons penetrate through the target and erupt from the rear surface into vacuum. As the hot electrons escape, they leave behind the immobile, positively charged ions, thereby setting up an intense electrostatic sheath field at the target rear surface. This sheath field points outward, normal to the target surface, and it accelerates ions (especially protons or other light ions present on the back surface) to high energies in the target-normal direction. This Target Normal Sheath Acceleration (TNSA) process can be summarized as:

- **Plasma formation:** Before the main peak of the laser pulse arrives at the target, the laser pre-pulse has sufficient intensity to ionize the atoms in the front surface of the target, generating a plasma. While an individual photon in the laser pulse does not have enough energy to ionize a target atom, ionization can still occur due to multi-photon ionization, tunneling, and barrier suppression. The now free electrons go on to further ionize the surrounding atoms through collisions.
- **Electron heating and transport:** The main part of the laser pulse heats the free electrons at the front surface through a variety of heating mechanisms. These electrons, with a temperature T_e , stream through the target unimpeded due to their high velocity and build up an electron cloud beyond the back surface.
- **Sheath formation and ion acceleration:** The spatial separation of hot electrons and the remaining target ions creates a quasi-static electron (Debye) sheath. This sheath field (typically a few MV/ μm over a scale of a few microns) drives ions at the rear surface to accelerate outward along the target normal.

Characteristics of TNSA ion beams

TNSA ion beams have several distinctive properties:

Broad energy spread: The ion energy distribution is roughly exponential in shape with a continuous spectrum up to a maximum cutoff energy E_{max} [33]. The cutoff energy generally scales with laser power P_L as $E_{max} \propto \sqrt{P_L}$ [24].

$$\frac{dN}{dE} = \frac{N_0}{E_{th}} e^{-E/E_{th}} \quad \text{for } E < E_{max}, \quad (2.1)$$

Large divergence: Typical TNSA proton beams have half-angle divergences on the order of $\theta_{div} \sim 20^\circ - 40^\circ$ which is quite large compared to The spatial and angular distributions of the ion beam are determined by the spatial distribution (shape) of the electron sheath [34] which can be described as bell-shaped [35]. Ions will be accelerated in the direction of the electric field pointing normal to the electron density gradient of the sheath [36].

Low transverse emittance: Experiments have measured normalized transverse emittances as low as $0.004 - 0.1$ mmmrad for TNSA protons [37]. The origin of this ultralow emittance is the rapid, space-charge-neutralized acceleration in the sheath: ions are accelerated from rest to high velocity in an extremely short distance, and the presence of co-moving electrons keeps the beam quasi-neutral during acceleration suppressing Coulomb explosion [6]. The result is a highly laminar beam that appears to originate from a point-like source (much smaller than the physical ion-emitting area). This excellent emittance is a major advantage of laser-driven ion beams, as it promises superior beam focusability and transportability.

Bunch duration: The ion bunch accelerated in TNSA is very short in time. Essentially, the ions are accelerated in a single burst during the rise of the sheath field (on the order of the laser pulse duration, tens of femtoseconds to a few picoseconds). The resulting ion bunch can be picosecond-scale at the source, leading to ultrashort pulses of ions. As the

ions have a velocity spread, the bunch will stretch in time as it propagates (longer flight time for lower energies), but close to the source the ion pulse duration is extremely short (much shorter than conventional accelerator beams). This ultrashort, high peak current ion burst is of interest for applications requiring short time scales such as ultra-high dose rate radiobiology and isochoric heating.

In summary, TNSA produces high-charge, MeV-energy ion beams with low emittance but large divergence and a broad energy spectrum. These characteristics have driven a great deal of research into beam control (using magnetic optics or novel targets to collimate or focus the beam) and into alternative acceleration mechanisms that might intrinsically deliver higher energies or narrower spectra.

2.1.2 Other acceleration mechanisms

While TNSA is the most prevalent and experimentally demonstrated mechanisms of LDIA, its limitations—particularly the broad energy spread, high divergence, and limited achievable energy—have motivate explorations of other acceleration mechanisms. Two important mechanisms that may promise higher ion energies and improved beam quality are Magnetic Vortex Acceleration (MVA) [38, 39] and Radiation Pressure Acceleration (RPA) [40, 41].

Magnetic Vortex Acceleration is a regime that occurs when an ultra-intense laser interacts with a near-critical-density (NCD) plasma target - i.e. a plasma with electron density n_e on the order of the lasers critical density ($n_c \sim 10^{21} \text{ cm}^{-3}$ for 800 nm light). In this scenario, the laser penetrates into the target, expelling electrons ponderomotively, forming a low density channel. Electrons are accelerated in the laser's wake forming high current filament through the center of the channel. The current induces a strong azimuthal magnetic which co-propogates with the laser and electron filament through the channel (acting as a

waveguide) to the rear side of the target. As the electron filament and magnetic vortex escapes into vacuum, a strong longitudinal and transverse electric field is created due to the charge separation and expanding magnetic field that accelerates and focuses ions in the channel. Simulations predict that MVA can accelerate protons to hundreds of MeV with high laser-to-ion energy conversion efficiency [24].

Radiation Pressure Acceleration is a fundamentally different scheme in which the lasers light pressure directly drives the acceleration of ions. In this mechanism, the laser behaves like a piston or light sail, pushing on the plasma as a whole. When an intense laser is reflected or absorbed by a medium, it imparts momentum equal to the radiation pressure.

The theoretical advantages of RPA lie in its scaling and beam quality. Unlike TNSA (where energy comes from a thermal process and saturates), RPA offers a much more favorable scaling of maximum energy with laser parameters. In fact, for light-sail RPA the energy per ion can scale in proportion to the laser pulse fluence (intensity \times time) - meaning one could reach GeV ion energies by using sufficiently intense, long pulses. Moreover, if the foil accelerates as one piece, all ions gain nearly the same energy, yielding a monoenergetic beam rather than an exponential spectrum. In simulations, RPA with circular polarization has indeed produced narrow energy-spread ion bunches (sometimes with a quasi-monoenergetic peak) instead of the broad TNSA spectrum [6].

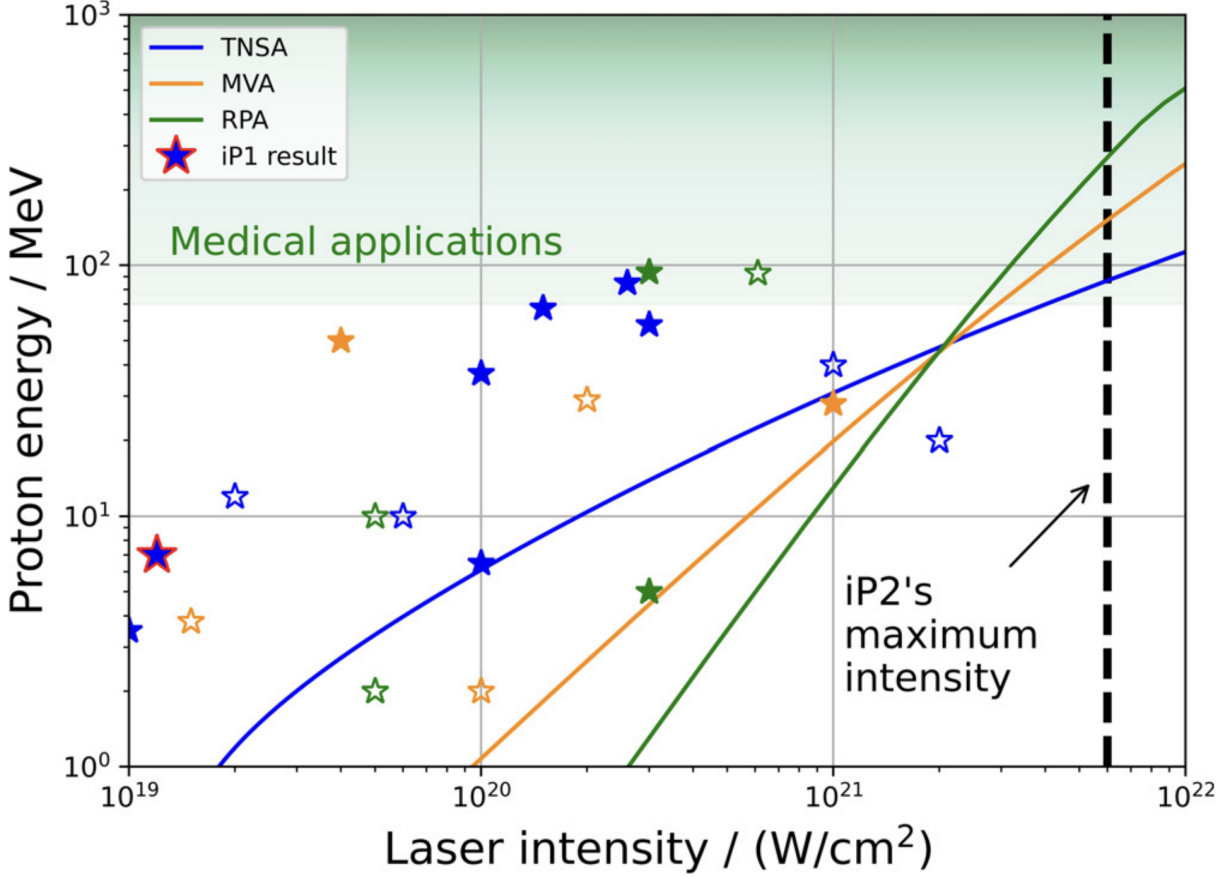


Figure 2.1: Scaling laws for different acceleration mechanisms are shown for a pulse duration of ~ 35 fs along with a collection of experimental data on maximum proton energies at various laser intensities. Experiments in the TNSA regime are shown in blue, and experiments reporting on the onset of advanced mechanisms are shown in green. The maximum proton energy generated using the BELLA PW (iP1) is shown with a blue/red star. Experiments conducted with a pulse duration of < 50 fs are shown with hollow stars. The range of proton energies relevant to medical applications is displayed in green. The maximum on-target peak intensity of the BELLA iP2 beamline is marked with a dashed black line. From [24].

Each alternative mechanism (MVA, RPA, as well as others like collisionless shock acceleration and break-out afterburner) comes with its own requirements and challenges. MVA requires near-critical plasma targets and carefully tuned laser propagation through them, while RPA requires ultra-thin targets and good laser temporal contrast. The theoretical promise of these schemes is significant: both MVA and RPA offer more efficient ion acceleration and higher ultimate energies than conventional TNSA. Developing these alternative

mechanisms is important for the future use of laser driven sources in applications.

2.2 Ion beam transport and delivery

After being generated in the laser-plasma accelerator through the processes outlined above, the particle beam needs to be collected and transported by a beam transport system before it can be used for an application. Particle beam transport refers to the process of guiding and focusing beams of charged particles from one location to another. This is achieved using special arrangements of electromagnetic fields designed to steer and focus the beam. The goal is to ensure the beam maintains its desired trajectory and quality while being transported to its target location, whether it's an experimental target, a medical patient, or another accelerator.

This section will give a brief overview of the relevant beam physics, the mathematics describing the motion of ensembles of particles in accelerator structures. Much of this is adapted from *An Introduction to Beam Physics* by M. Berz, K. Makino, and W. Wan [42].

2.2.1 Curvilinear coordinates

In order to describe the propagation of an ensemble of particles as a beam mathematically, it is useful to describe their motion relative to a reference trajectory that follows the desired main beam path. The motion of a given particle in the beam can be described in six

coordinates combined into one vector \vec{z} ,

$$\vec{z} = \begin{pmatrix} x \\ a = \frac{dx}{ds} = \frac{px}{p_0} \\ y \\ b = \frac{dy}{ds} = \frac{py}{p_0} \\ l = \kappa(t - t_0) \\ \delta = \frac{K - K_0}{K_0} \end{pmatrix} \quad (2.2)$$

The first four terms (x, a, y, b) describe the motion of a particle in the plane transverse to the beam propagation s , with x and y representing the displacement from s and a and b representing the angular divergence from the reference trajectory. The energy deviation δ represents the deviation of a given particle's initial kinetic energy K from that the reference particle's, K_0 .

The variable l represents the deviation of the time-of-flight t from that of the reference particle, but is in units of length as it multiplied by a constant κ that has the dimension of velocity. Specifically,

$$\kappa = -v_0 \frac{\gamma_0}{1 + \gamma_0} \quad (2.3)$$

using the absolute value of the velocity of the reference particle v_0 and the associated γ_0 .

This defines a curvilinear coordinate system where the frame moves along a reference trajectory, or curve, where the reference particle is always centered.

2.2.2 Transport maps

The motion of a particle moving through a beam transport can be described by a transfer map M , relating its final phase-space vector \vec{z}_f to its initial phase-space vector \vec{z}_0 ,

$$\vec{z}_f = M\vec{z}_0. \quad (2.4)$$

To first order, this mapping can be represented as a transfer matrix

$$\begin{pmatrix} x \\ a \\ y \\ b \\ l \\ \delta \end{pmatrix}_f = \begin{pmatrix} (x|x) & (x|a) & (x|y) & (x|b) & (x|l) & (x|\delta) \\ (a|x) & (a|a) & (a|y) & (a|b) & (a|l) & (a|\delta) \\ (y|x) & (y|a) & (y|y) & (y|b) & (y|l) & (y|\delta) \\ (b|x) & (b|a) & (b|y) & (b|b) & (b|l) & (b|\delta) \\ (l|x) & (l|a) & (l|y) & (l|b) & (l|l) & (l|\delta) \\ (\delta|x) & (\delta|a) & (\delta|y) & (\delta|b) & (\delta|l) & (\delta|\delta) \end{pmatrix} \begin{pmatrix} x \\ a \\ y \\ b \\ l \\ \delta \end{pmatrix}_i \quad (2.5)$$

where each element in M represents coupling between elements in the particle's state vector \vec{z} . For example, $M_{12} = (x|a)$ represents the effect a particle's initial transverse momentum (a) has on its final position (x). Having the elements $M_{12} = (x|a)$ and $M_{34} = (y|b) = 0$ stipulates that the initial transverse momentum has no impact on its final position (to first order). This is necessary to achieve point-to-point focusing which delivers the highest intensity beams at the focal plane.

To study higher order or nonlinear effects, this mapping can be Taylor expanded. For example, the expansion for x is given as

$$x_f = \sum^n (x|x^{i_x} a^{i_a} y^{i_y} b^{i_b} l^{i_l} \delta^{i_\delta}) x_0^{i_x} a_0^{i_a} y_0^{i_y} b_0^{i_b} l_0^{i_l} \delta_0^{i_\delta} \quad (2.6)$$

where the sums go over all six-tuples $(i_x, i_a, i_y, i_b, i_l, i_\delta)$ up to arbitrary order $n = i_x + i_a + i_y + i_b + i_l + i_\delta$. Each element represents a specific aberration that distorts a particles motion described by the linear map. For example, the term $M_{126} = (x|a\delta)$ is a chromatic aberration that causes the focal plane of an imaging system to shift according to a particles energy δ .

2.2.3 Magnetic optics

A beam transport is made up of magnetic optical elements used to steer and focus the beam. These are specially designed arrangements of magnetic fields that manipulate the trajectories of charged particle beams. Magnetic optics can act similarly on particle beams as glass optics act on beams of light (i.e. lensing), and are often using a similar framework.

The simplest magnetic optical element is the dipole magnet, which are used to steer the beam. A dipole magnet is made of two poles that create a constant magnetic field between them. A particle with charge q and momentum p will move inside a uniform magnetic field B in a circular orbit of radius ρ equal to the Larmor radius

$$\rho = \frac{p}{qB}. \quad (2.7)$$

Off-momentum particles will be deflected at different angles from the reference trajectory according to their magnetic rigidity $B\rho = p/q$.

Quadrupole magnets are linear elements used to focus charged particle beams.

$$\vec{B} = \begin{pmatrix} Gy \\ Gx \\ 0 \end{pmatrix} \quad (2.8)$$

Quadrupole magnets are focusing in one plane while defocusing in the other. By including a drift section between two of them, they can achieve overall focusing.

2.3 Radiation transport in matter

After acceleration and beam transport, the laser driven ion beams are delivered to a sample where they deposit their energy into the material.

Radiation transport refers to the physical mechanisms by which energy is transferred from ionizing radiation—such as photons and charged particles—to the atoms and molecules of a medium. The specific modes of interaction depend on both the type and energy of the radiation and the properties of the target material. These interactions govern the spatial distribution and magnitude of energy deposition, forming the basis of dosimetry and radiobiological modeling.

This section outlines the physical principles of radiation transport relevant to the systems and exposures used in this work. It begins by examining the attenuation and absorption of X-rays in matter, followed by a treatment of the stopping power and linear energy transfer (LET) for massive charged particles like protons, and concludes with a discussion of Monte Carlo radiation transport methods used to simulate dose deposition from broadband laser-accelerated beams. Understanding this interaction is essential not only for accurate dose

delivery but also for interpreting the biological effects of radiation, particularly in the context of ultra-high dose rate exposure.

2.3.1 X-ray absorption and attenuation in matter

X-ray photons have sufficient energy to ionize atoms. They can interact with the nuclei and electrons in matter through incoherent scattering, coherent scattering, photoelectric absorption, and pair production. A photon has a certain probability of interacting depending on the photon energy and elemental makeup of the material it is passing through. The cross section σ is a measure of this probability. The cross sections for the different types of interaction are well documented across a wide range of photon energies and elemental compositions.

A more useful metric for the absorption of X-rays is the linear attenuation coefficient μ . This quantity is related to the cross section and can be defined as the probability per unit path length that a photon will interact with a medium.

Fig. 2.2 shows the linear attenuation coefficient in water as a function of photon energy separated by the different interaction types.

The intensity of an X-ray beam decreases exponentially with distance into a material as the photons randomly interact and are absorbed. Assuming the material is of uniform density and composition, the intensity I can be calculated at a certain distance z into the material using

$$I(z) = I_0 e^{-\mu z}, \quad (2.9)$$

where I_0 is the original photon intensity.

This is relevant for dose rate characterization of the X-ray sources outlined in Ch. 3.

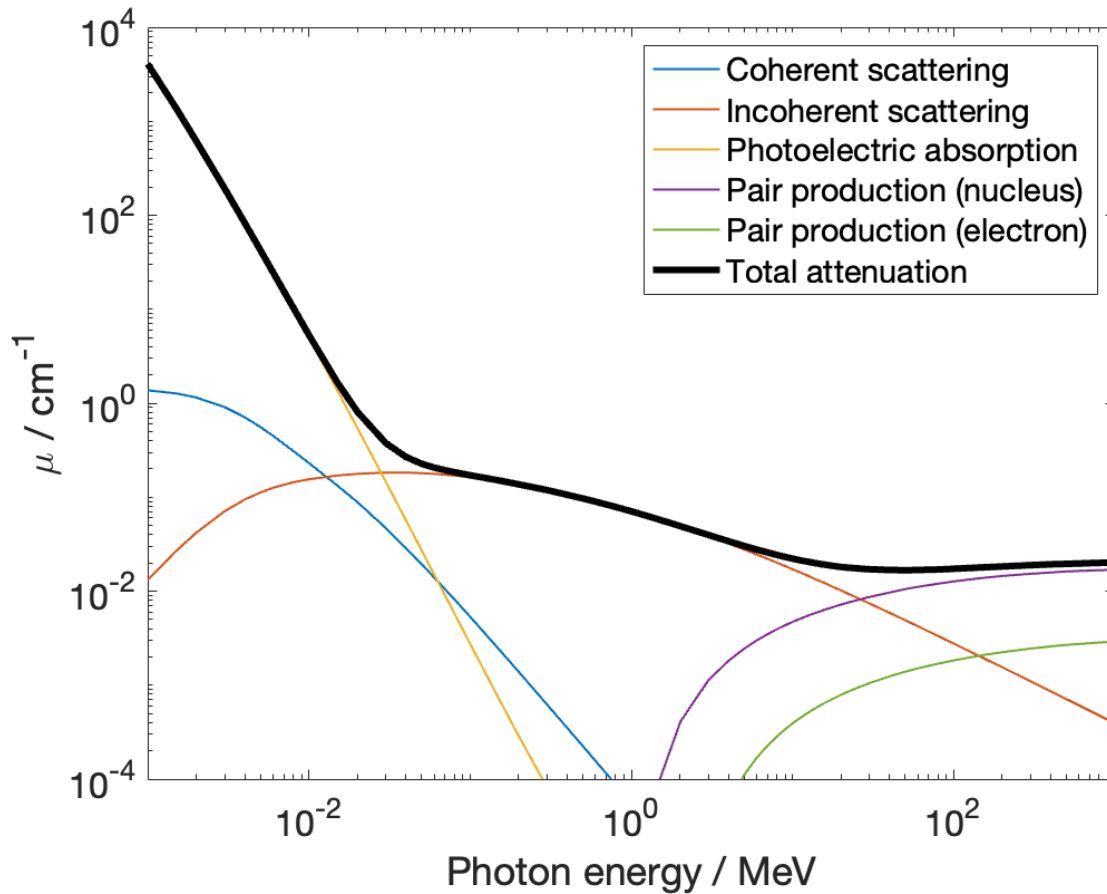


Figure 2.2: Linear attenuation coefficients for water for the different interaction types. The sum of the linear attenuation coefficients from each type of interaction is equal to the total linear attenuation shown in black. Data from [43]. Assumes density of water is 1 g/cm^3 .

2.3.2 Stopping power and linear-energy transfer (LET) of massive particles

Massive charged particles such as protons deposit their energy differently from photons. Charge particles experience a retarding force as they interact with the electrons and nuclei in the material they move through.

Stopping Power is defined as the energy loss per unit path length of a charged particle (such as a proton) traveling through matter. The linear stopping power S is given by $S = -\frac{dE}{dx}$, where dE is the mean energy lost by the particle in traveling a small distance dx in the medium. The negative sign indicates the particle is losing energy. Linear stopping power has units of energy per length (e.g. MeV/cm) and is often separated into the electronic stopping power—from inelastic collisions with electrons causing ionization/excitation of atoms—and nuclear stopping power—from elastic collisions with nuclei. The electronic stopping power dominates for therapeutic proton energies (10s-100s MeV). Note, protons can also lose energy through the emission of bremsstrahlung (radiative stopping power) but this is only important for ions at extremely high energies.

The stopping power $S = -\frac{dE}{dx}$ of a proton with velocity v (relative velocity $\beta = v/c$) and charge state Z in a material with electron density n_e and mean excitation energy I_e can be analytically described by the Bethe Bloch formula

$$S = -\frac{dE}{dx} = \frac{4\pi}{m_e c^2} \frac{n_e Z^2}{\beta^2} \left(\frac{e^2}{4\pi\epsilon_0} \right)^2 \left[\ln \left(\frac{2m_e c^2 \beta^2}{I_e (1 - \beta^2)} \right) - \beta^2 \right] \quad (2.10)$$

where c is the speed of light, ϵ_0 is the vacuum permittivity, and m_e and e are the electron rest mass and charge, respectively [44, 45]. Rather than evaluate Eq. 2.10 for every proton

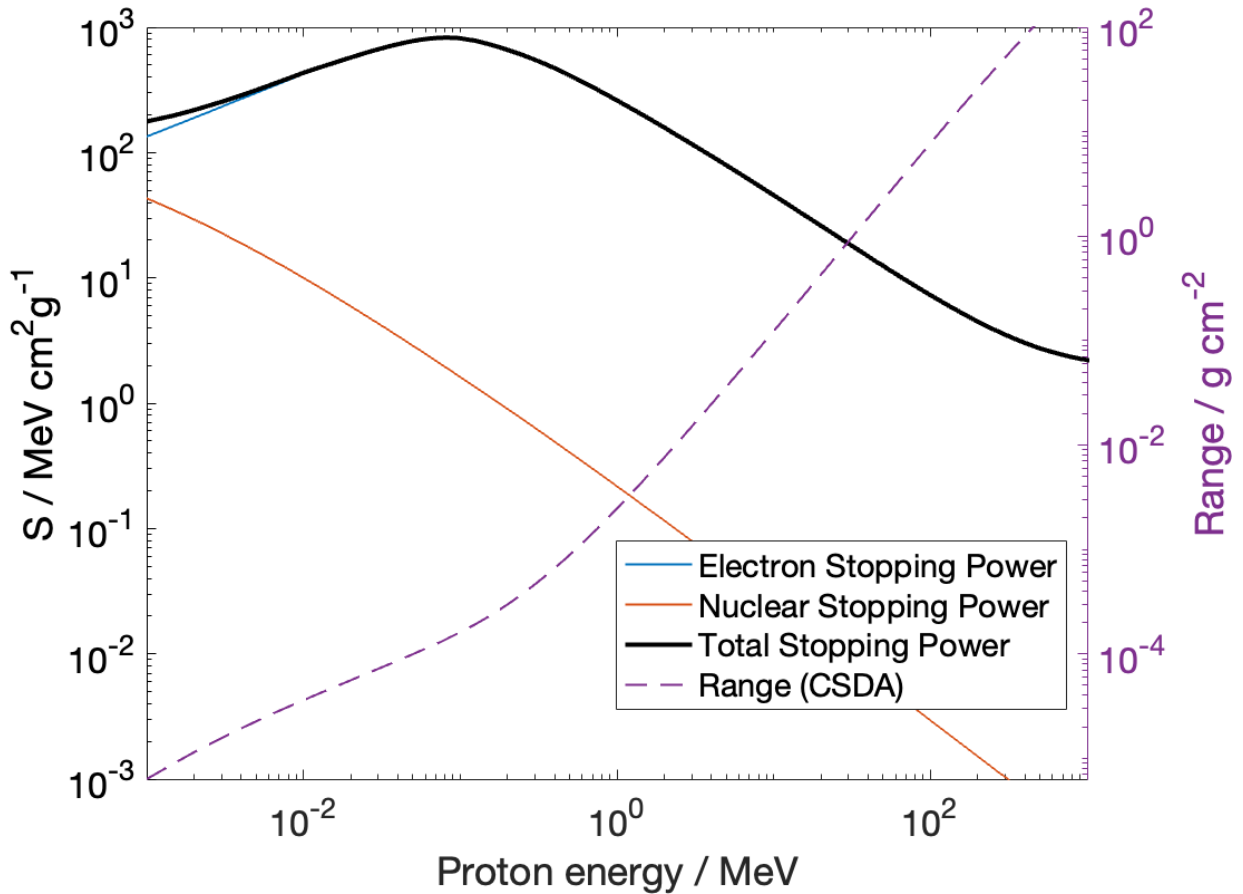


Figure 2.3: Mass stopping power and range in water for various proton energies. The electron stopping power (blue) makes up the majority of the total stopping power (black). The range is calculated using the continuous slowing down approximation (CSDA).

energy, it is easier reference online databases for these values, such as PSTAR [46], which are based on this formula and supplemented with empirical data for low energy protons (< 0.5 MeV) where the Bethe-Bloch model is less valid.

For convenience, stopping power is frequently expressed as a mass stopping power (per density), S/ρ , in units of $\text{MeV cm}^2/\text{g}$. Mass stopping power is normalized by material density to enable comparison across materials.

Linear Energy Transfer (LET) is closely related to stopping power, but with a focus on the energy *deposited* into the medium as opposed to the energy *lost* by the particle.

Formally, LET is defined as the average energy imparted to the medium per unit distance by a charged particle. The LET accounts for energy that remains in a small local region around the particle trajectory while excluding the energy carried away by secondary particles (like energetic delta-ray electrons or bremsstrahlung photons that may deposit energy far from the region of interaction). In practice, for heavy charged particles like protons, the unrestricted LET (with no cut-off for secondary electron energy) is numerically very similar to the total electronic stopping power. Thus, in radiotherapy contexts, the terms LET (usually expressed in keV/m) and linear stopping power are often used interchangeably when referring to the protons energy deposition rate in tissue. It is important to note, however, that conceptually stopping power refers to energy loss of the particle (regardless of where that energy goes), whereas LET refers to energy deposited locally in the medium.

Stopping power and LET directly link to dose deposition. The absorbed dose D (energy deposited per unit mass, in J/kg or Gy) from a proton beam can be estimated by multiplying the stopping power by the beam fluence (number of protons per unit area). For a monochromatic proton beam of energy E and fluence $\Phi = \frac{dN}{dA}$, the dose deposited into a medium D_{med} of density ρ can be calculated using

$$D_{\text{med}} = \Phi \frac{S(E)}{\rho}. \quad (2.11)$$

For a polychromatic beam, the dose deposited can be estimated by integrating the stopping power over the whole spectrum as

$$D_{\text{med}} = \int \Phi_E \frac{S(E)}{\rho} dE, \quad (2.12)$$

where Φ_E is the spectral proton fluence (number of particles at energy E per unit area).

In essence, high stopping power (high LET) means more energy is deposited in a short distance, yielding a higher local dose. This underpins the formation of the Bragg peak and is central to proton dosimetry calculations.

The Bragg peak refers to the pronounced peak in dose deposition that occurs near the end of a protons range in matter. It arises because protons lose energy more rapidly as they slow down (higher stopping power at lower velocity). A Bragg curve is a plot of the protons linear energy transfer (or dose) as a function of depth in the medium. At the surface (entrance), a proton beam deposits a relatively low dose (called the dose plateau). With increasing depth, the dose gradually rises as the proton slows, then peaks sharply just before the protons come to rest, and drops to essentially zero beyond the range. A picture of this behavior in Fig. 2.4. This behavior is in stark contrast to the depth-dose of photons, which exhibit an exponential attenuation with no sharp end-of-range peak.

It is this property that gives proton therapy its clinical advantage: by adjusting the proton beam energy, the Bragg peak can be positioned to cover the tumor at a specific depth, delivering a high dose to the tumor while sparing the surrounding normal tissues.

2.3.3 Monte Carlo radiation transport

The energy deposition of ionization radiation can be effectively simulated using Monte Carlo methods [47]. Computer simulations that use Monte Carlo methods rely on repeated random sampling of probability distributions in order to model processes that are too complex to simulate deterministically.

Geant4 [48] is a general-purpose simulation toolkit that provides accurate modeling of particle interactions with matter, making it invaluable for replicating proton beam transport

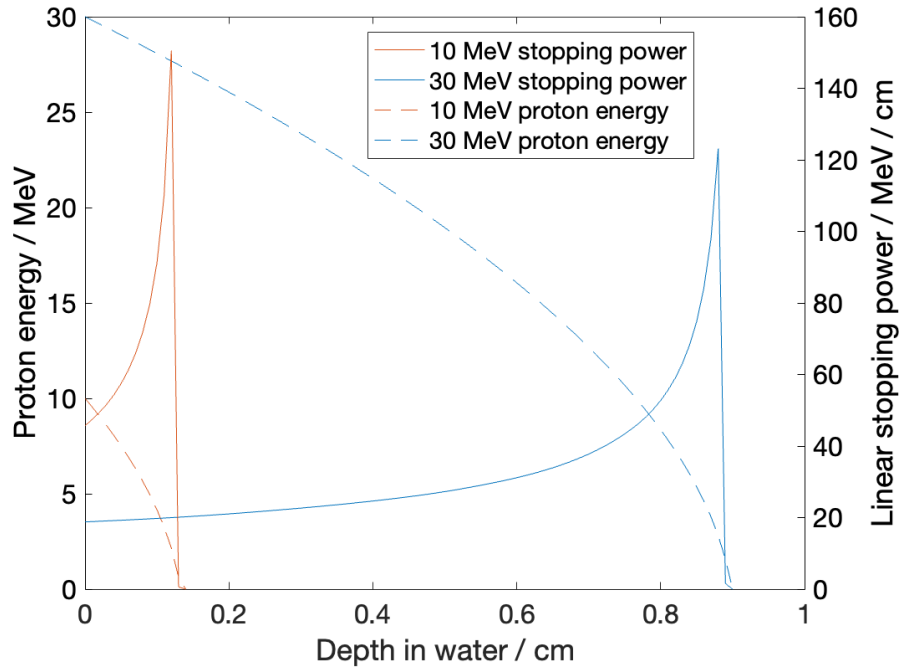


Figure 2.4: Energy deposition of 10 MeV and 30 MeV protons in water over 1 cm. Protons deposit most of their energy near the end of their range.

and energy deposition in complex geometries. Building upon Geant4, the TOPAS (TOol for Particle Simulation) platform [49] offers a user-friendly interface tailored to medical physics applications, greatly facilitating the setup of comprehensive proton therapy simulations.

Monte Carlo methods are particularly valuable when dealing with non-conventional beam sources, such as proton beams generated by laser-driven accelerators. Unlike the quasi-monoenergetic beams from conventional cyclotron-based proton therapy, laser-accelerated proton beams emerge from the target with broad energy spectra and large angular divergence. This intrinsic spread can be harnessed to create unique dose profiles—for example, a broadband proton spectrum can be shaped to produce a spread-out Bragg peak that covers a greater depth range in tissue—but it also means the resulting dose distributions are more complex and not readily handled by simple analytical dose models [50]. MC simulations excel in this scenario by explicitly tracking each proton and its interactions, thereby capturing

the true three-dimensional dose distribution delivered by such unconventional sources.

Chapter 3. Exploring the extremes of radiobiology across different modalities and exposure environments

3.1 Introduction to radiation therapy

Radiation therapy (also called radiotherapy) is a cancer treatment that uses ionizing radiation to kill cancer cells and shrink tumors [51]. Radiotherapy is the current standard of care for > 50% of all cancer patients [52], but its use is limited by access to facilities and healthy tissue toxicity [29].

Proton beam therapy [53] exploits the unique energy deposition characteristics of protons to deliver dose to tumors with high precision. Unlike photons (X-rays) which deposit energy exponentially with depth, protons deposit relatively low dose in the entrance region and a sharply peaked high dose near the end of their range (the Bragg peak).

There is a long history of radiation therapy research at the Lawrence Berkeley National Laboratory (LBNL). The 184-inch cyclotron at LBNL was the site of the first use of protons beams in cancer treatment back in 1958, work led by John H. Lawrence, the brother of the founder Ernest O. Lawrence [26]. Radiobiology research continues at LBNL with evermore sophisticated radiation sources. Presented here is the work to establish these new radiation sources (or exposure environments) to serve as platforms for radiobiological research. This includes characterizing and performing dosimetry on multiple exposure environments at LBNL including the Advanced Light Source's 3.2.1 and 3.3.1 beamlines.

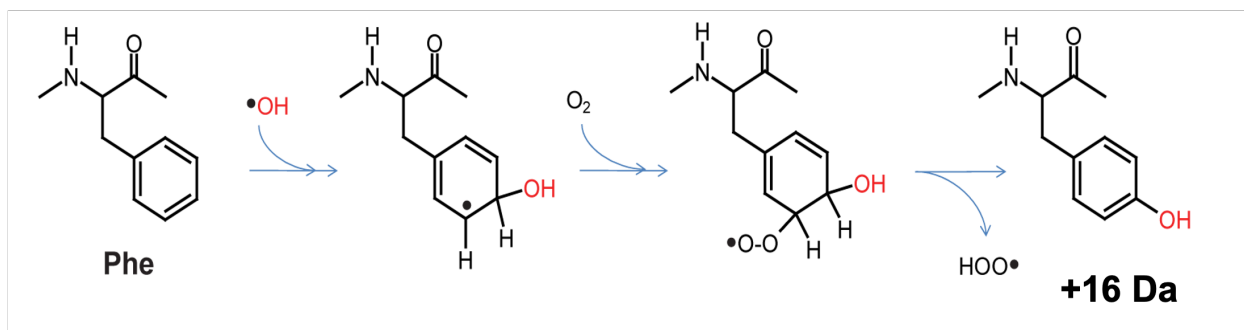


Figure 3.1: Example of phenylalanine modification by a hydroxyl radical.

3.1.1 The FLASH effect

One of the most promising recent innovations in the field of radiation oncology is the discovery of the FLASH effect [18]. The FLASH effect refers to the enhanced differential sparing between normal and tumor tissues when irradiated at ultra-high dose rates, much higher than those used in current clinical use. The effect has been observed in different *in vivo* animal models—such as mice [16, 54], mini-pigs and cats [17]—and with different beam modalities—such as electrons [16], protons [55], and photons [56].

However, the underlying mechanism of the FLASH effect is still not well understood. While there are numerous candidates that have attempted to explain this phenomenon, such as radiolytic oxygen depletion [57], self-annihilation of radicals [58], and altered immune system response [59] it likely involves a combination of factors.

One approach we have taken to study the FLASH effect is a reductionist approach to achieve a molecular level understanding of radiation damage.

Radiolysis—radiation-induced chemical decomposition—of water during exposure to ionizing radiation creates hydroxyl radicals. These radicals are highly reactive and can lead to damage or modification of nearby organic molecules. Figure 3.1 shows an example of the modification of phenylalanine (a type of peptide). The hydroxyl radical attacks the oxygen in

solution and fixes the modification in place leading to a +16 Da (amu) increase in molecular weight of the polypeptide.

And modifications by hydroxyl radicals can be detected using liquid chromatography-mass spectrometry (LC-MS) [60]. The retention time increases with the modification and the proportion of modified peptides can be quantified. The modifications can be expressed as a fraction modified with respect to the dose delivered.

Using the exposure environments outlined below, we exposed short peptides made of 6 to 16 amino acid residues to radiation and quantified radiation-induced damage to the peptides. The biological results of the work done at the Advanced Light Source's 3.3.1 beamline is published in [27].

This chapter will detail an important step in establishing these experimental platforms to study radiobiology: dosimetry.

3.2 Dosimetry methods

Dosimetry is the method of measuring the dose absorbed by a material (usually biological tissue or water) from different types of ionizing radiation. Due to the differences between the exposure environments, such as the particle type and energy spectrum, dosimetry has to be performed specifically and carefully in each environment before they can be used for research purposes. The dosimetry tools described in this section were used to determine the dose deposition of the various radiation sources used for radiobiology experiments.

3.2.1 Radiochromic film

Radiochromic film (RCF) is a type of dosimeter widely used in radiation dosimetry due to its high spatial resolution and near-tissue equivalence [61]. The active layer of the RCF is sensitive to ionizing radiation and undergoes a change in color which can be directly related to the dose that would be absorbed by a sample in that environment. More precisely, it consists of radio-sensitive chemicals which polymerize into optically opaque polymers upon irradiation. This is a chemical reaction which takes approximately 24 hours to complete, although most of the development occurs in the first hour. As the film develops after being exposed to ionizing radiation, the transmittance T of light through the film decreases, i.e. it becomes more opaque. This change in opacity can be directly related to the absorbed dose.

The change in opacity is quantified by the Optical Density (OD), the log of the ratio of the initial light intensity I_0 and the transmitted light intensity I ,

$$OD = -\log_{10} \frac{I}{I_0} = -\log_{10} T. \quad (3.1)$$

The OD can be measured using different readout sources, often a photo spectrometer or flatbed scanner.

To account for differences in the opacity between separate film pieces from manufacturing error, it is recommended to subtract an unexposed film's OD from the OD of the exposed film—resulting in a netOD—so that the change in opacity is solely due to radiation exposure. The netOD-dose response for a given film can be determined by delivering a range of known doses from an independently characterized source of radiation and measuring the associated netOD for each dose.

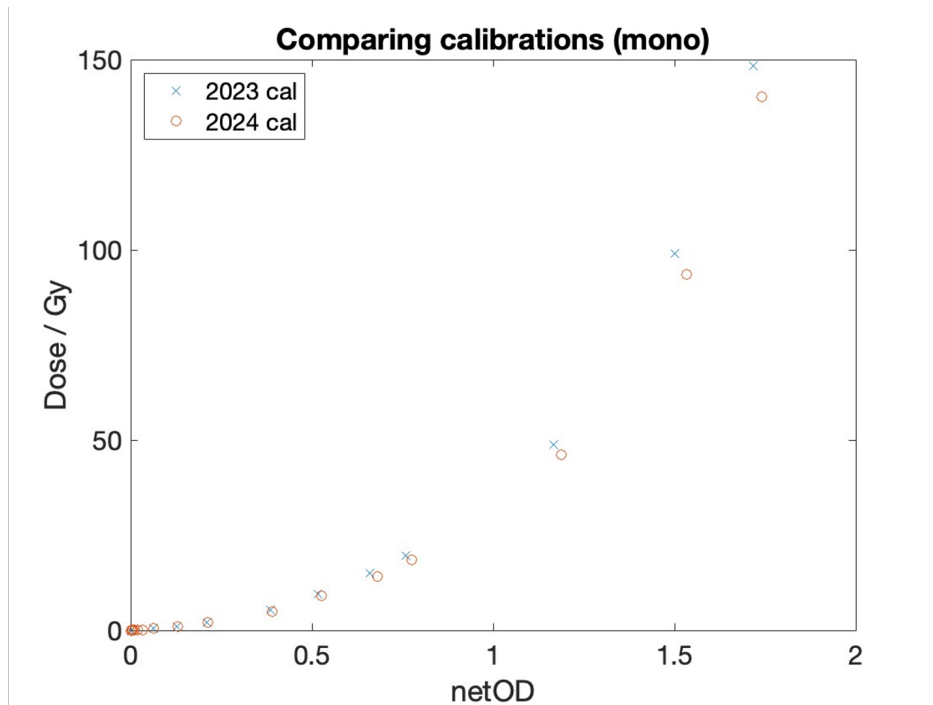


Figure 3.2: Calibration curves of the RCF (EBT3) used in the two radiobiological experiments outlined in Ch 5

The response curves are not absolute however as they depend on a number of factors [62]:

- Film model, lot number, and chemical composition
- Radiation type (photons, electrons, protons, alpha), radiation energy
- Readout system used, including scanner model and wavelength of light used to measure the OD
- Time between exposure and processing.

The two models of film used in this work are GAFchromic HD-V2 and GAFchromic EBT-3, both produced by Ashland (Bridgewater, NJ). The two models differ in their structure (see Fig. 3.3), their chemical compositions (see Table 3.1, and the range of doses they are designed to measure. HD-V2 has a recommended dose range from 10-1000 Gy while EBT-3 has a recommended dose range from 0.01-20 Gy [62]. While the films are near-tissue (water)

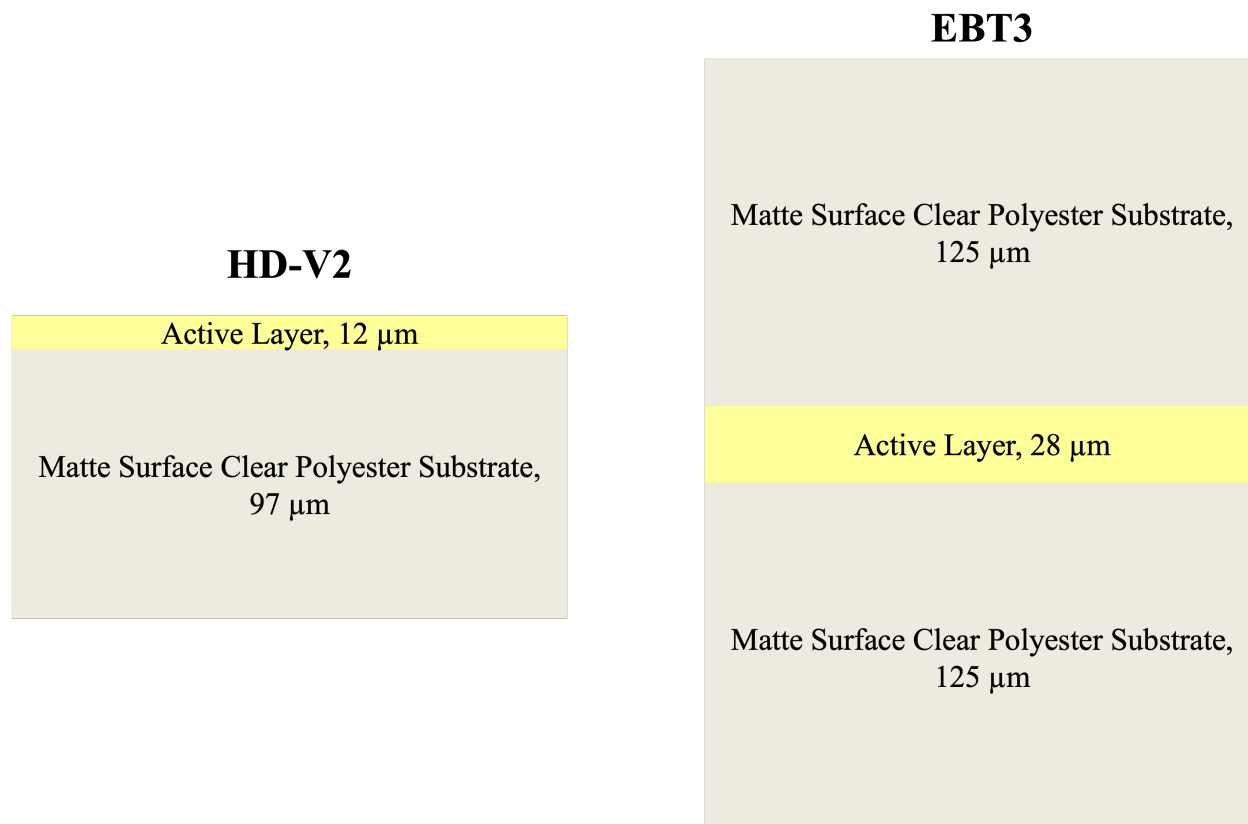


Figure 3.3: Structure of GAFChromic HD-V2 (left) and EBT3 (right) dosimetry film.

equivalent, due to the difference in material makeup and density, the dose deposited will be slightly different between film and sample. The chemical compositions and structures of the RCF were used in simulations to estimate the conversion between the measured dose in the films to the dose deposited in the actual samples.

All of the films presented in this thesis were scanned using an EPSON Expression 12000XL scanner with all image correction features turned off, at a typical resolution of 200 dpi (127 $\mu\text{m}/\text{pixel}$) in transmission mode. The scanned images were saved as 16-bit grayscale and 48-bit color TIFF files. Scanning was typically conducted several days after irradiation to allow for stabilization of the optical density development after irradiation. The raw pixel values were converted to OD using a NIST-calibrated transparency step wedge that was included in every scan.

Film model	Composition by element and atom %									
	H	Li	C	N	O	Na	Al	S	Cl	Z_{eff}
HD-V2	58.2	0.62	27.7	0.40	11.7	0.48	0.27	0.05	0.62	7.63
EBT3	56.5	0.60	27.4	0.30	13.3	0.10	1.60	0.05	0.10	7.46

Table 3.1: Chemical composition (atomic%) and the effective atomic numbers Z_{eff} of the active layer of the RCF models used for dosimetry [62]. Both models have an active layer density of 1.2 g/cm³. Z_{eff} is a useful metric for comparing the dose deposition between different materials. The Z_{eff} of water is 7.42 indicating the active layer of EBT3 is closer to water-equivalent in terms of radiation interactions than that of HD-V2.

The OD to dose calibration (Fig. 3.2) was acquired by exposing films in triplicate with x-rays generated with a 320 KV x-ray tube (X-RAD320) and comparing the measured optical density with the dose measured with an Radcal ionization chamber.

3.3 Characterizing exposure environments for radiobiology research

3.3.1 X-ray tube (X-RAD320) for reference dosimetry and low dose detection

The BioEngineering & BioMedical Sciences (BBS) Department in the Biological Systems & Engineering (BSE) division at LBNL houses an X-Ray tube machine (X-RAD320, Precision X-ray) which has been routinely used by scientists for irradiations of cells and small animals.

An X-ray tube generates hard X-ray photons by colliding electrons with a high Z material target (typically tungsten). The electrons are thermionically emitted from a hot cathode into vacuum and then accelerated by a high voltage potential V_p (in units of kV often expressed as kVp when referring to the peak voltage). When the electrons collide with the target the interaction produces X-ray photons through bremsstrahlung—radiation produced by the

deceleration of a charged particle—and "Characteristic X-rays"—target dependent radiation produced when the vacancy of an inner shell electron (ionized by the incoming electron) is filled by an outer-shell electron. The X-ray spectrum produced is broadband with a maximum photon energy determined by the tube voltage $E_{\nu,\max} = eV_p$ while the lower edge can be controlled by a hardening filter. To compare between different machines, the spectrum is often described using the half-value layer (HVL)—the depth in a given material (usually aluminum or copper) at which half of the photons in the beam would be absorbed. The number of emitted X-ray photons can be adjusted by controlling the tube current and exposure time.

The XRAD-320 machine at LBNL is designed specifically for radiation therapy, having a highly homogeneous beam.

Operating at $V_p = 300$ kVp and with a 0.5 mm Cu beam hardening filter in place during irradiations, the machine was determined to have a HVL in Cu of 3 mm.

The dose rate is influenced by the:

- Photon spectrum: dependent on the tube potential V_p , the hardening filter, and source-to-sample distance (due to hardening in air)
- Photon flux: dependent on the tube current, hardening filter, source-to-sample distance (due to attenuation in air)
- Sample: dependent on the material, thickness, geometry

Absolute dosimetry was performed using a RadCal dosimeter (Rad-cal 10X6-0.18 ion chamber) to both determine the dose rate for a given machine setting and to monitor the dose applied to samples/RCF during irradiation.

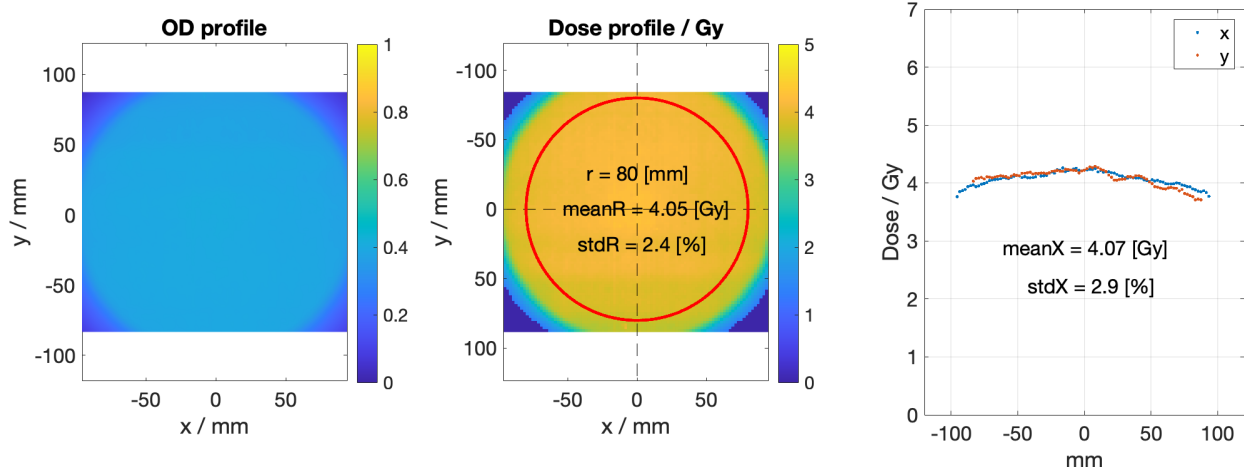


Figure 3.4: XRAD dose profile measured by EBT3 RCF.

The machine was used to calibrate our RCF. The XRAD machine was also used for conventional dose rate X-ray irradiations of both the *in vitro* (peptide) and the *in vivo* (mice) samples. When multiple samples were exposed, they were placed on a rotating platform to ensure uniform irradiation across all of them. The uniformity of the XRAD field was measured using RCF and is shown in Fig.3.4.

3.3.2 Synchrotron radiation at the Advanced Light Source (ALS)

Synchrotron light sources are large circular accelerators that generate high energy photon beams (synchrotron radiation) that can be used for many applications. As the electrons that orbit the storage ring in a synchrotron light source pass through a bending section (dipole), they emit radiation as they are transversely accelerated.

$$E_c = \hbar\omega_c = \frac{3\hbar c\gamma^3}{2\rho} \quad (3.2)$$

The critical energy E_c (or critical frequency ω_c) is a measure of the photon spectrum that divides the spectrum into two regions of equal radiated power.

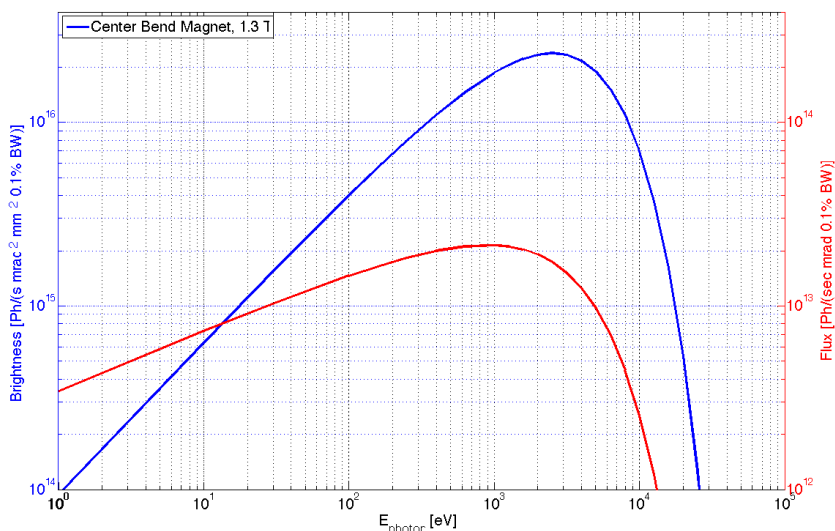


Figure 3.5: Photon spectrum of an ALS bend magnet (1.3 T) with an electron beam energy of 1.9 GeV and beam current of 500 mA [63].

The Advanced Light Source (ALS) beamline delivers a broadband X-ray beam with critical energy 3.1 keV from a 1.3T bending magnet [27].

The spectrum can be hardened by placing thin metal filters (attenuators) that preferentially absorb low energy X-rays. The high brilliance (flux) of synchrotron light sources makes them well-suited to studying high dose rate radiobiology [64].

Two beamlines at the ALS (Beamlines 3.2.1 and 3.3.1) have been established to explore ultra-high dose rate radiobiology at the molecular level.

3.3.2.1 ALS Beamline 3.2.1

At the ALS beamline (BL) 3.2.1, samples of peptides are suspended in solution and irradiated using the X-ray beam as shown in Fig. 3.6. To ensure an accurate dose is delivered to the samples, dosimetry was performed using radiochromic film to characterize the dose rate with varying levels of attenuation in the beamline.

Previous dosimetry of the beamline relied on a single piece of film to estimate the dose

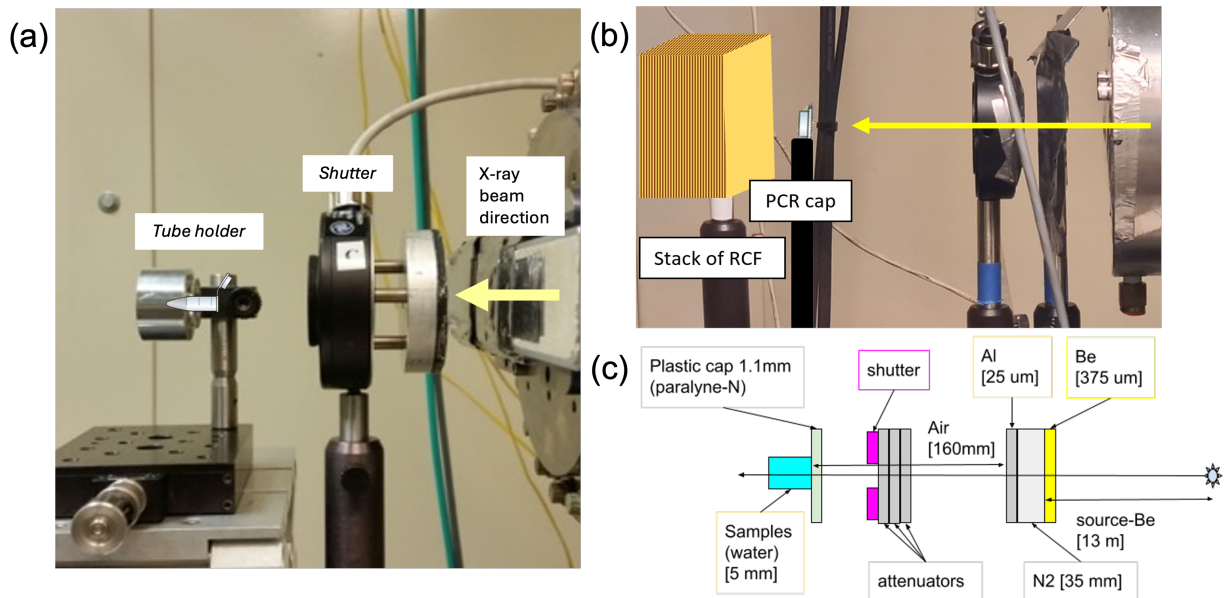


Figure 3.6: (a) Overview of ALS 3.2.1 irradiation platform. Samples are placed in solution in Eppendorf tubes held in the beam by a metal holder. A shutter controls the exposure time. The X-ray beam (entering from the right) passes through varying levels of attenuation attached to the shutter. (b) Dosimetry was performed using a stack (multiple pieces of film on top of each other) of RCF (EBT3) to measure the dose depth profile for different levels of attenuation. The plastic cap from the Eppendorf is placed in front of the stack to account for the attenuation in the material. (c) The MC model geometry built in TOPAS to simulate the beamline accounting for all the material present in the beamline that attenuates and hardens the beam spectrum.

rate. However, Monte Carlo simulations (TOPAS) of the beamline revealed that the beam significantly attenuates through the 5 mm thick sample lowering the average dose rate seen over the whole volume. Stacks of RCF were placed in the beamline to mimic the thickness of the sample and capture the dose rate at different depths for each attenuation thickness used. The average dose rate over the stack (accounting for the decreasing cross-sectional area of the water in the tube) was calculated and is shown in the table below.

The Monte Carlo simulations attempt to fully replicate the environment of BL 3.2.1 to account for attenuation and spectral shifting due to the matter present in the beamline (beam pipe exit, Be window, N₂ gas, plastic cap, air), but relies on assumptions for the synchrotron radiation properties based on the ALS beam parameters. The simulations give a 40% higher dose rate than as measured by RCF, but this difference is consistent across all thicknesses of attenuation which implies a systematic error, most likely in the synchrotron radiation assumptions. As RCF dosimetry was never performed with no attenuation present in the beamline, these simulations were used to extrapolate the dose rate of the beamline in that case.

The RCF dosimetry done here aimed to emulate the dose deposition in the samples in solution exposed at the ALS. However, the doses measured by subsequent layers in the RCF stack is not 1:1 with the dose deposited in water due to differences in absorption at these beam energies (10-30 keV). Simulations comparing the dose deposited in water vs. EBT3 were done with the TOPAS setup outlined above to account for this difference in absorption between the two cases.

When comparing the dose deposited into a single layer of RCF vs. water with equivalent thickness MC simulations showed near water-equivalence of the active layer of the film (less than 2% difference). However, the substrate in front of the active layer was found to be

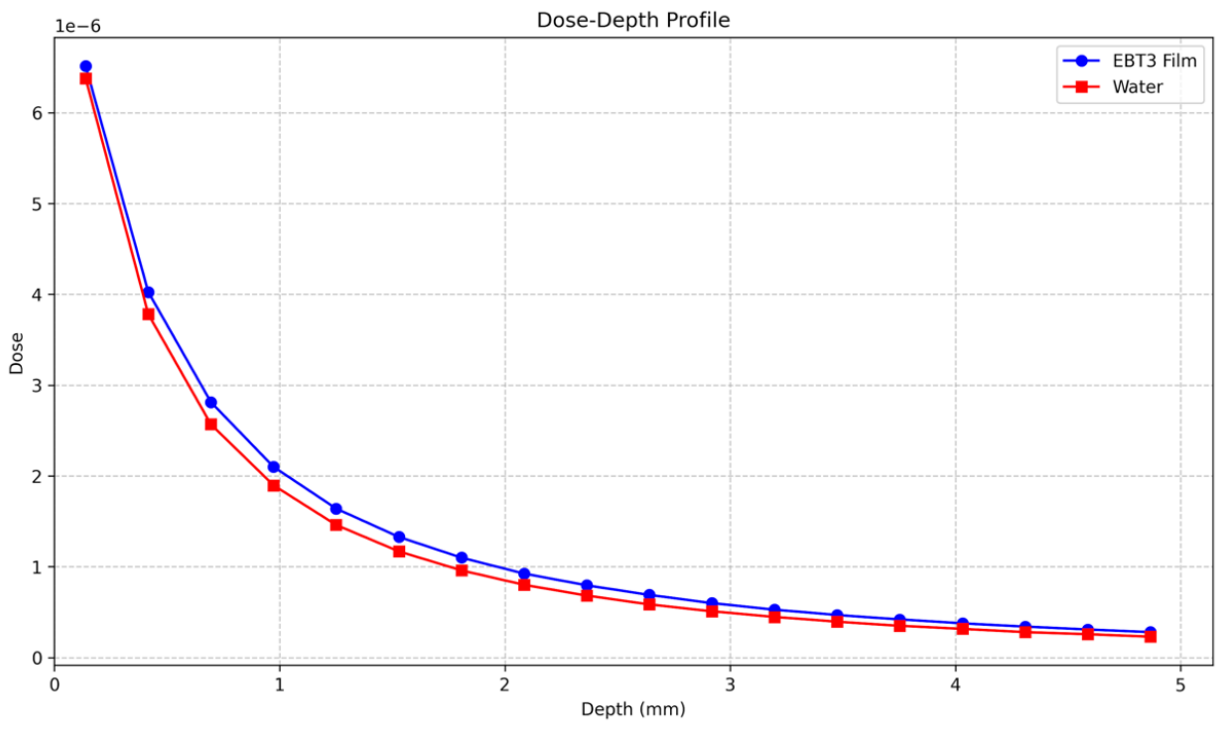


Figure 3.7: Simulated dose depth in each layer of the RCF stack and the dose deposited at an equivalent depth in water. The RCF would receive slightly more dose than the water sample at equivalent depths.

Attenuation / mm of Al	Dose rate in water / Gy s ⁻¹
0	3,970*
1	134
2.5	17.2
4.7	2.75
7.7	0.557

Table 3.2: Dose rates measured by RCF at the ALS 3.2.1 beamline (500 mA) with varying levels of aluminum attenuation present.*As RCF dosimetry was never performed with no attenuation present in the beamline, TOPAS simulations were used to extrapolate the dose rate of the beamline in that case.

slightly less attenuating than water. More photon flux would reach the active layer than at an equivalent depth in water (depth = 125 μm) causing the EBT3 to overestimate the dose deposited at that depth.

When simulating the full stack, the ratio between dose deposited in water and dose deposited in the film decreases with depth as each substrate attenuates the beam less than water. To account for this difference, the dose rate values for a given attenuation were scaled by a single correction factor. This correction factor was calculated using the simulated total dose deposited in the 5mm-thick water sample and the average of the dose deposited across each layer of the simulated RCF stack.

$$D(5 \text{ mm water sample}) = 0.925 \times \frac{1}{18} \sum_{i=1}^{18} D(\text{EBT3 film layer } i)$$

Using this correction factor, the doses as measured by the RCF were scaled to obtain the dose rate in water. The dose rates for varying levels of attenuation are shown in Table 3.2. These were used to set the exposure time of the shutter and dose applied to the samples.

3.3.2.2 ALS Beamline 3.3.1

An irradiation platform was established at the ALS beamline 3.3.1 to study dose rate effects on oxidative damage to peptides. This beamline differs from BL 3.2.1 in that the synchrotron radiation beam is focused with a platinum-coated X-ray mirror to a minimum beam size of $\sim 80\text{-}100\ \mu\text{m}$.

Sample exposure was done by streaming a liquid jet of sample solution through the X-ray beam. The samples were prepared in syringes connected to a high-pressure syringe pump that ejects the solution out of a $75\ \mu\text{m}$ jet nozzle at varying speeds of 4-20 m/s. As it travels from the nozzle to the sample collector below, it passes through the X-ray beam and the speed of the liquid determines the exposure time. A full description of this setup is described in [27] and [65].

Dosimetry on the 3.3.1 beamline was performed using GAFchromic HDv2 RCF due to the higher dose rate of the focused X-ray beam. A high dose rate calibration for this film type was used to convert from OD to dose from [66].

The films were placed at the focal position of the X-ray beam in place of the liquid jet and irradiated the day prior to sample irradiation. The films were irradiated with various exposure times and with varying levels of attenuation, resulting in doses applied to the film in the range of 1.48.4 kGy, to characterize the dose rate profile of the beamline. A Uniblitz XRS6 X-ray shutter (Vincent Associates, NY) was used to control the exposure time.

The X-ray intensity was not spatially uniform vertically, which resulted in a variable dose rate as the jet passed through the beam. The dose measured in each pixel in an RCF scan was divided by the exposure time of the RCF to calculate the dose rate measured in each pixel. The profile was then scaled by the exposure time per pixel of the liquid jet at the two

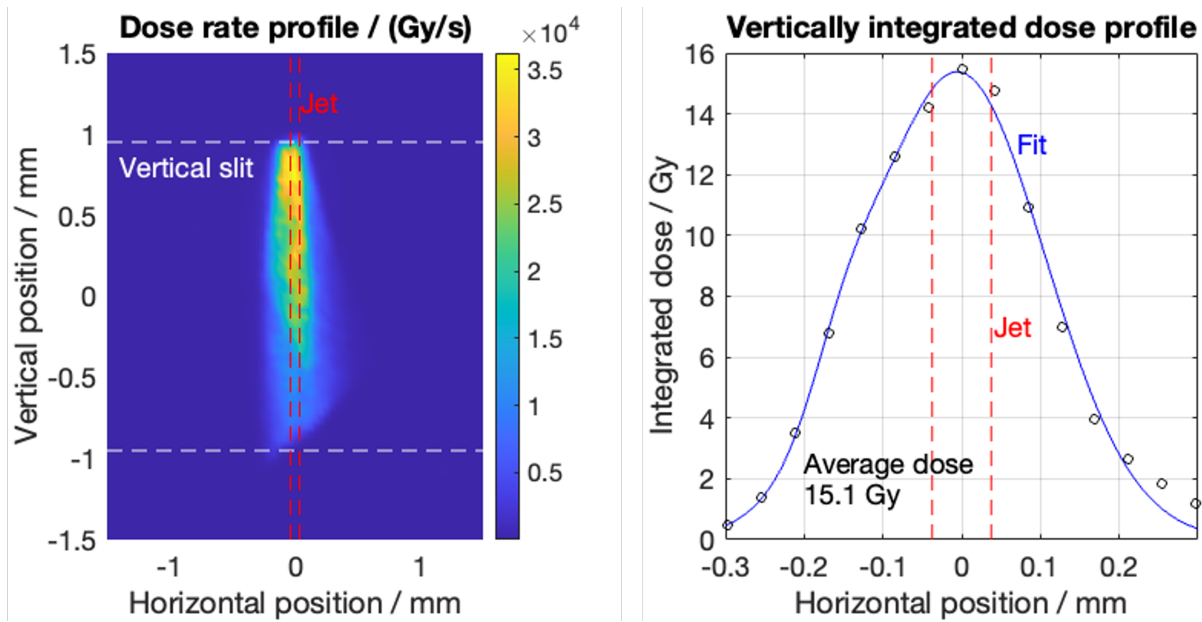


Figure 3.8: Example of dosimetry estimation at the ALS 3.3.1 beamline. (a) Dose profile of the X-ray beam measured by an RCF (left). (b) The vertically integrated dose is fit to a double Gaussian (right) and an average over $75 \mu\text{m}$ of the peak of the fit is reported as the dose absorbed by the sample present in the liquid jet.

speeds (4 and 20 m/s). The exposure time per pixel is the pixel width (42.3 μm) divided by the jet speed and represents the time the sample would be irradiated as it passes through the space that pixel represents. By then integrating the dose profile vertically, the non-uniformity of the X-ray intensity was taken into account, for the derivation of the radiation dose and dose rate received by the liquid jet.

There was also some slight non-uniformity in the horizontal X-ray intensity across the width of the water jet (75 μm). Due to the limited resolution of the RCF scans at that scale, the dose values reported in [27] were calculated by fitting the integrated dose profile to a double Gaussian and then averaging over the width of the water jet.

3.3.3 Laser driven proton beams

Precise evaluation of the absolute dose delivered by poly-energetic proton beams requires accurate knowledge of the proton energy spectrum [67].

Monte Carlo simulations (see Section 4.2.2) of the beam transport proved necessary for the dosimetry due to the linear energy transfer (LET) dependent response of the RCFs. Schollmeier et al. [68] has shown that, like other charged particle detectors, the RCF response is affected by LET, causing films to under-respond near the Bragg peak where the LET is highest. Schollmeier et al. found that the film detection efficiency η , the ratio of the measured dose to the expected dose, falls with increasing stopping power dE/dx as

$$\eta = 1 - 0.4 \exp[-4 \exp[-0.2dE/dx]]. \quad (3.3)$$

The stopping power for a given material is a function of the incident particle energy and the material properties. Lookup tables for many common materials are available through the NIST database [46]. Using Eq. 3.3 and the beam spectrum modeled with the MC code, the dose values measured by the RCFs were scaled to account for this LET effect.

The dosimetry of the laser-driven ion beams used in radiobiology experiments will be discussed more in Chapter 5.

Chapter 4. Modeling and design of compact permanent magnet-based transport systems for laser driven ion acceleration

In this chapter, we report on a design study for such compact ion beam transports, transporting up to 30 MeV protons to a dedicated sample site. Various configurations were explored and their performance was analyzed so that potential users of future LDIA facilities can choose the optimized configuration for their applications.

This work lays the foundation for the broader application of laser-driven ion beams by addressing two of their most significant challenges: large divergence and broadband energy spread. The tools and designs presented here will enable current and future laser-driven ion accelerator facilities to more effectively meet the diverse needs of users across various applications.

4.1 Permanent magnet-based optical elements

In order to take full advantage of the acceleration mechanism's compact nature, it is preferable for the beam transport to also be compact. This has proven to be a difficult task however, as LD ion beams are characterized by an initially large divergence and energy spread at the source. To accommodate such beams, transport systems using high gradient focusing elements have been utilized in the field, typically via pulsed solenoids [69, 70, 71] or permanent magnet quadrupoles (PMQs) [72, 73]. The beam transports based on PMQs have been demonstrated for up to 14 MeV laser-driven proton beams [74, 75, 76, 77]. An-

other option is to use an active plasma lens (APL) [78, 79, 80, 29]. For certain applications, APLs can be attractive due to the tunability of the focusing force and azimuthal symmetry though the radial acceptance of APLs is not readily expandable which limits its collection efficiency. Superconducting magnets [81, 82] can achieve a very strong field gradient with a large bore but, not only can they become prohibitively expensive, they require a large cryogenic apparatus which exceeds the size requirements. They also run the risk of quenching from being so close to the laser-plasma interaction. Lastly, if compactness is not required, electromagnets and hybrid designs with technologies mentioned above can provide extended capabilities [83].

We chose to focus on beam optical elements using permanent magnets considering the cost and space efficiency, relatively high field gradient, and their established performance under harsh laser-plasma environments. Sets of permanent magnets with specific magnetization vectors can be arranged in a Halbach arrangement [84] to achieve the same field profiles seen in typical electromagnetic optical elements (e.g. dipoles, quadrupoles, and sextupoles) but with higher fields. This special arrangement can boost the overall strength of a permanent magnet optic given the limited remanent magnetization of commercially available rare-earth ferromagnetic materials. In general, permanent magnet quadrupoles (PMQs) can achieve gradients of 100s T/m while their normal conducting electro-magnetic counterpart is typically limited to 1 T/m.

Permanent magnet quadrupoles (PMQs) are able to achieve this field strength with a relatively large bore (20 mm) which is important as a large bore leads to a larger beam admittance. And as the applications for LD accelerated beams generally require a large beam current, maximizing collection efficiency is crucial for the transport design.

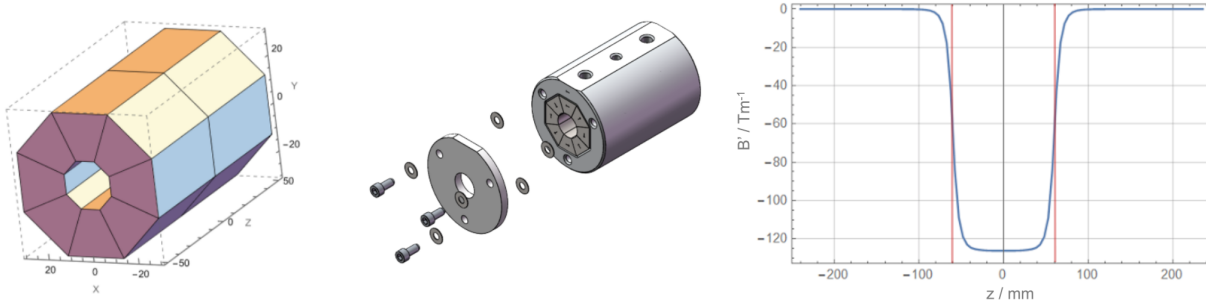


Figure 4.1: Design (left), technical drawing (middle), and simulated field gradient as function of the propagation axis z (right) of the permanent magnet quadrupoles. The physical length is 120 mm (shown in red) and other parameters were described in Table 4.1.

4.1.1 Permanent magnet quadrupoles (PMQ)

The magnetostatic simulation code RADIA [85] was used to design the PMQs. The magnets were based on an 8-azimuthal-segment Halbach array with 1.29 T of the bulk magnetization B_r . An example of the magnet geometry is shown in Fig. 4.1. This configuration is readily achievable for commercial vendors, and this bulk magnetization level is typical for a N40 grade NdFeB magnet, which is also commercially available at relatively low cost. Since the main purpose of this work is to explore different configurations of the transport systems, only the magnet length was varied to change the focusing strength of the PMQs for simplicity, while keeping the other parameters, such as inner radius and the magnetic field at the tip. The fixed properties of the PMQs used in this design work are shown below in Table 4.1.

The simulated field gradient for a 120 mm PMQ along the propagation axis z is shown in Fig. 4.1, where the maximum field gradient was 126.2 T/m with the magnet effective length of 120.2 mm giving $B_{tip} = 1.26$ T. The effective magnetic field at the surface of one of the magnet segments, B_{tip} , depends on the bulk magnetization, the magnet outer radius and the length. It was found that $B_{tip} = 1.16$ T was readily achievable for any length of the PMQs, and therefore used in this study.

Table 4.1: PMQ fixed parameters used for transport design. The length, number, and distance between the magnets were varied

Fixed parameters	Value
Inner radius	10 mm
Outer radius	30 mm
Bulk magnetisation B_r	1.29 T
Effective magnetic field at tip B_{tip}	1.16 T
Target - 1st PMQ drift space D_1	40 mm
Minimum magnet - magnet distance	80 mm
Minimum last magnet - output distance	40 mm

The magnetic fields in the COSY simulation are based on the built-in magnet distributions in COSY. One can see from Fig. 4.1 that the fringe fields taper off ($> 99\%$) about 40 mm from the physical edges of the magnet. Thus in COSY, the fringe fields on either side of each magnet were modeled using the most sophisticated approximation available in COSY which models them as falling according to the ENGE function outlined in [86]. The minimum drift length between the PMQs was set to 80 mm and between the last magnet and system output was set to 40 mm to avoid overlap of the fringe fields, which can reduce effective strength of the PMQs. The drift space between the target and the first PMQ D_1 was fixed to 40 mm for the same reason in addition to the beam collection efficiency being of primary concern. Between these values, the magnet and drift lengths were varied to find the optimal magnet locations to achieve focusing at the sample plane.

4.1.2 Permanent Magnet Dipoles

Depending on requirements from applications, dipole magnets may be desired to manipulate the energy spectrum of the beam after transport. Dipole magnets were considered for a number of transport designs discussed in this study, at different locations along the beamline. They were also designed using RADIA. They consist of a rectangular shape yoke made of 1018

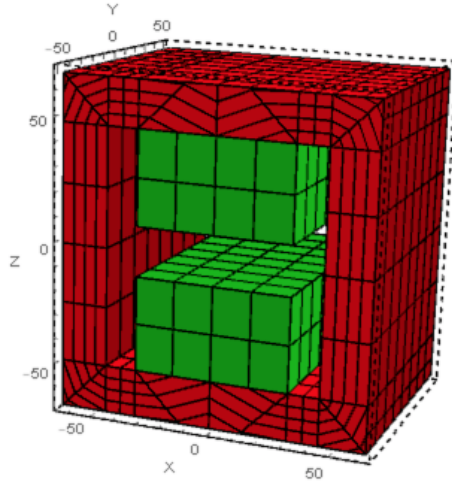


Figure 4.2: Illustration of the permanent magnet dipole. The yoke is indicated in red and the magnets are indicated in green. The segmentation is for simulation purposes.

Table 4.2: PMD parameters

Parameters	Value
Half gap	10 mm
Height	124.8 mm
Bulk magnetisation B_r	1.29 T
Effective magnetic field	0.89 T
Minimum magnet - magnet distance	80 mm

steel and NdFeB permanent magnet blocks as illustrated in Fig. 4.2. The bulk magnetization was assumed to be $B_r = 1.29$ T, identical to the PMQs discussed above.

The geometrical parameters of permanent magnet dipoles (PMDs) are summarized in Table 4.2. The gap of the dipole magnet was set to be 20 mm to match the inner radius of the PMQ. The magnet length was 50.8 mm to ensure flat magnetic field profile ($< 3\%$) within 20 mm horizontally. The longitudinal length was varied depending on different applications. RADIA simulations showed that the fringe field extends 40 mm on each side, therefore the same 80 mm minimum magnet to magnet distance was imposed to the design work.

Note that one can improve the dipole field strength and uniformity by employing Halbach

magnets. In this design study, such improvements were not essential to realize the proposed systems, and therefore this simple dipole design was employed.

4.2 Transport design and simulation methodology

4.2.1 COSY INFINITY

Particle optics simulation tools are typically divided into two categories: numerical field integrators and map codes. Numerical field integrators, such as TRACK [87], IMPACT [88], G4Beamline [89], and BDSIM [90], model the complete electromagnetic fields in a system and simulate the trajectories of individual particles by integrating the equation of motion. Numerical field integrators are robust in their description of the beam dynamics but can be computationally expensive, making them less suitable for rapid lattice optimization and simulating large particle numbers. Conversely, map codes like MADX [91], TRANSPORT [92], and TRACE-3D [93], model the transport system as transfer matrices to describe the action of each optical element on the beam in phase space. The elements of these transfer matrices are smooth functions of the transport parameters and can be quickly computed, allowing for rapid optimization. This approach is also favored for optimization tasks due to the ability to quickly analyze optical properties of the system represented by the elements of the transfer matrix. This enables quick visualization and aberration correction, making them highly advantageous for streamlining the design process and enhancing system performance.

In this work, we utilized COSY INFINITY [86], which combines the speed of traditional map codes with the precision of numerical field integrators. COSY is commonly used in the study of accelerator lattices, spectrographs, beam transports, electron microscopes,

and many other devices. Using differential algebraic techniques to perform the numerical integration of the fields, it calculates Taylor expansions of the transfer map to arbitrarily high order.

Given a configuration of magnets or electrostatic fields, COSY INFINITY can approximate the transfer map to high order and optimize magnet strengths and positions. The transfer map needs to be known to high order here as non-linear effects are important due to the large beam size and energy spread of LD ion beams. The trajectories of a collection of particles can then be calculated by applying the map to the particles' initial values of position and momentum. COSY provides particle tracking for a small number of particles and can plot their trajectory through the transport. The COSY output maps were used to evaluate the different investigated transport systems' angular acceptance and transmission efficiency.

To ensure calculations were performed up to the appropriate order, initial simulations of the beam performance were done at successively higher orders. Beam performance appeared to converge after 3rd order for the simplest designs (doublet, triplet, quartet) and after 5th order for most complicated designs (mirrored quartet). In general, this should be done for each transport configuration to ensure the accuracy of the simulation. All results shown below were calculated to 3rd order, unless otherwise specified.

4.2.2 Monte Carlo-based radiation transport and particle tracking

In order to simulate and analyze the performance of the transport systems with a large number of particles, a custom MATLAB script was written. This code integrates the high order transfer map generated in COSY with a Monte Carlo (MC) based radiation transport code.

The code works by first generating a large number of macro-particles ($> 10^6$) with initial parameters to match the beam emerging from the laser-plasma interaction, based on previous experiments (see 4.2.3 below). After the initial beam is prepared, each macro-particle's phase-space vector is passed through the map which calculates each macro-particle's final phase-space vector. The performance of each transport design was then evaluated by calculating the peak density, energy acceptance, and beam spot size of the output beam.

In addition to calculating the trajectories of a large number of particles, the code also models the energy deposition into matter along the beam path as well as the energy deposition inside the sample. This allows for the optimization of the transport to ensure a high dose per shot and a uniform dose profile, which is relevant for beam transport designed for the radiobiological applications in 4.4 and in the next chapter. This modeling accounts for effects of energy degradation and scattering on the beam spectrum and profile, while describing the dose deposition on the sample and a number of radiochromic films (RCF) placed in the beam for dosimetry, based on data from the Particle Data Group [94]. More information on the beamline setup and all relevant absorbers are described in the next chapter.

4.2.3 Input beam parameters

The initial parameters of the simulated particles in the beam were chosen to match those from typical laser driven ion accelerators, based on previous experiments at the BELLA Center, the relevant laser parameters of BELLA iP2, and theoretical descriptions of target normal sheath acceleration (TNSA) [6, 29, 25]. The maximum laser intensity in the focus for the BELLA iP2 is estimated at $\approx 5 \times 10^{21}$ W/cm². For this beamline, the TNSA energy

spectrum for the accelerated proton beam was modeled as,

$$\frac{dN}{dE} = 5 \times 10^{10} [\text{MeV}^{-1}] e^{-E/(7 [\text{MeV}])}, \quad (4.1)$$

where N is the number of protons in a beam and E the kinetic energy of the protons.

The initial position and propagation angle of each particle were assigned corresponding to a Gaussian distribution with a source size of 0.1 mm (FWHM) and beam divergence of 450 mrad (FWHM), respectively. The initial angular divergence in real laser plasma accelerated beams is a function of the particle's energy [95] though here it is treated as constant. Particles with an initial divergence larger than the angular acceptance of the first magnet are neglected for the rest of the calculation but are used to estimate the collection efficiency.

In this work, the collection efficiency η is defined as the percentage of particles at the specific nominal (design) energy E_0 that are successfully captured and delivered by the beam transport. This metric is useful because the primary objective of the transport system is to deliver particles with energies close to the nominal energy. Further, it allows one to compare the collection efficiency for the nominal energy independently of the energy acceptance.

4.3 Beam transport designs for applications of LDIA

4.3.1 Configuration design and performance

4.3.1.1 Doublet

The doublet consists of two PMQs, each providing focusing force in either the x- or the y-plane, and is a widely used configuration [74, 75, 76]. The system can be configured to achieve point-to-point imaging in both transverse planes ($M_{12} = M_{34} = 0$). As an example, the shortest doublet system can be designed by having all the drift lengths at their minimum. With two variables L_1 and L_2 to meet two conditions $M_{12} = M_{34} = 0$, the shortest (430 mm from source-to-focus) 30 MeV doublet was designed and illustrated in Fig. 4.3, where the beam envelope for the $E_0 = 30$ MeV beam is shown by the green lines, and the beam

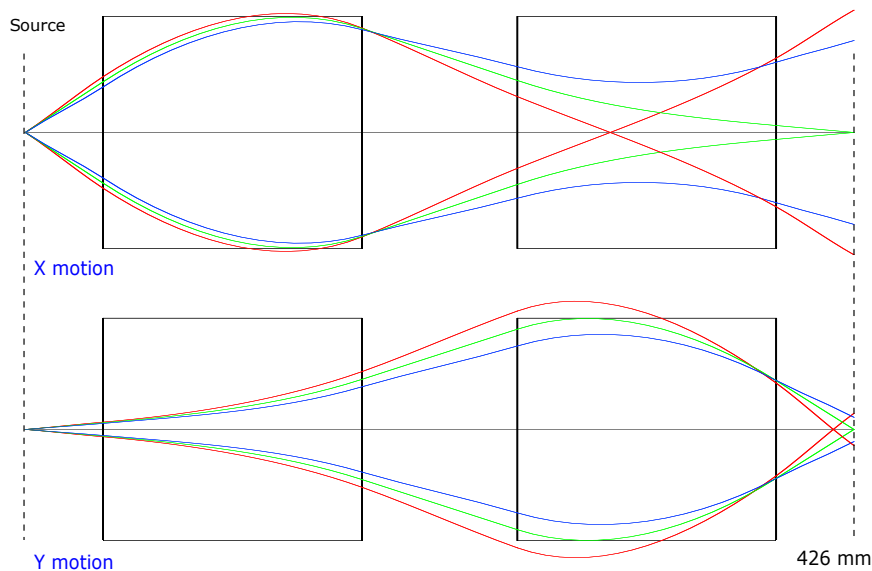


Figure 4.3: Illustration of the 430 mm doublet for $E_0 = 30$ MeV proton beam. The red, green and blue lines show the trajectories for proton beams with energies of $0.8 E_0$, E_0 , and $1.2 E_0$ with the maximum accepted divergence in each plane ($x' = 109$ mrad and $y' = 15$ mrad for $E_0 = 30$ MeV)

Table 4.3: Parameters of the systems, units are in mm for drift (D) and magnet lengths (L) and mrad for angular acceptance θ . Some designs were optimized to deliver beams of different nominal energies listed as E_0 in MeV.

Name	E_0	Length	θ_x	θ_y	D_1	L_1	D_2	L_2	D_3	L_3	D_4	L_4	D_5
Doublet	30	430	109	15	40	133.2	80	133.2	40				
Doublet	210	1000	48	6.2	157.7	133.2	412	133.2	157.7				
Doublet	30	750	109	15.9	40	126.3	80	55.3	448.3				
Doublet	30	1000	109	16.3	40	124.2	80	49.9	705.9				
Triplet	30	560	110	17.5	40	118	80	79.5	80	118	40		
Triplet	117	1000	48	9.5	97.5	118	282.5	79.5	170.4	118	131.3		
Triplet	30	1000	46.5	23.5	40	95.5	80	69.9	80	43.6	591.1		
Quartet	610	52	21.5	40	102.4	80	77.1	80	76.1	80	33.8	40	
Quartet	92	1000	24	14.5	59.6	102.4	225.3	77.1	133.8	76.1	198.2	33.8	132.4
Quartet	30	1000	28.5	32.5	40	66.6	80	67.9	80	60.6	80	27.2	496

envelopes for the kinetic energies $0.8 E_0$ and $1.2 E_0$ are shown by the red and blue lines, respectively.

As illustrated in Fig. 4.3, particles with different energy would have a different angular acceptance as the effective focusing of the PMQs is energy dependent. For simplicity, the angular acceptance angles θ_x and θ_y listed in Table 4.3 are given as the angular acceptance for particles with the nominal energy, E_0 .

One can see from Fig. 4.3 that the beam angular acceptance is limited by the first PMQ for the x plane, and by the second PMQ for the y plane. Since the second magnet is further downstream, and the beam gets further defocused by the first, angular acceptance is less in the y plane than the x plane. This is why in the final design, discussed in 4.4, the bore of the second magnet was enlarged to improve the overall collection efficiency. In the exploratory part of this paper, the bore sizes were fixed in order to compare different configurations.

Shown in Fig. 4.4 (left) is the transverse beam profile at the focal position on the right of Fig. 4.3 for the 430 mm doublet output and its energy spectrum (right). The transverse beam profile for the doublet is quite asymmetric, with different levels of magnification in the

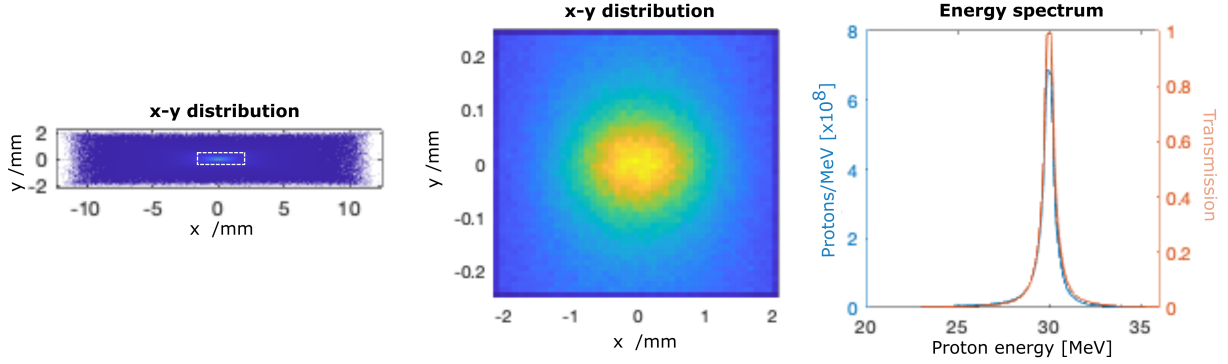


Figure 4.4: The output transverse beam profile of the 430 mm doublet (left is to scale, middle is zoomed in) and the output beam energy spectrum and energy-dependent normalized transmission through the beam line (right), within the limited transverse beam profile area of ± 1 FWHM indicated by the dashed white line in the left image.

x and y planes. Here the energy spectrum was evaluated by limiting the spatial integration of the beam particles to within one FWHM of the output spot size. This is equivalent to limiting the beam going into the spectrometer with an iris in the laboratory.

The performance parameters of the 430 mm doublet, namely the collection efficiency η , the peak density of the proton beam n_{1pk} at the output plane, the energy spread in FWHM δE , and output beam size in FWHM σ , are shown in Table 4.4. This configuration would capture 2.7% of 30 MeV protons generated at the source can be delivered to the output of the transport for the source parameters chosen for this study. In reality, the overall acceptance of a given beamline depends on the real source parameters and may be higher due to the energy-dependent divergence of LD ion beams [6].

One can design doublet systems of various sizes, and the solution may not be unique. For doublet designs, one can maximize the angular acceptance of the beam by minimizing the drift lengths, D_1 and D_2 . Also shown in Table 4.4 are performance parameters for the 30 MeV 750 mm and 1.0 m doublet systems with the minimum D_1 and D_2 , whose system parameters are shown in Table 4.3. The shorter system delivers higher proton density with

Table 4.4: Simulated beam transport results for doublet configurations of different lengths, including the collection efficiency η , peak ion density n_{1pk} , energy acceptance δE , and FWHM beam sizes σ_x, σ_y at the output plane.

Length [mm]	η [%]	n_{1pk} [$10^9/\text{mm}^2$]	δE [MeV]	σ_x [mm]	σ_y [mm]
430	2.70	16.7	0.65	0.76	0.034
750	2.86	3.4	1.15	1.5	0.161
1000	2.93	1.8	1.2	1.98	0.23

a narrower energy spread and smaller spot size. The longer system can provide larger beams with small improvement in the collection efficiency and focus symmetry. When an application demands high proton density, one might employ the shortest transport system that can be achieved from a technical implementation standpoint.

Once manufactured, the magnet strength cannot be varied for PMQs. Therefore, their locations have to be varied to focus particles with different energies. The mentioned 430 mm doublet was designed for 30 MeV, and could not focus lower energy protons because all the drift lengths were minimum. The same set of PMQs used in the 430 mm doublet configuration can be rearranged within a 1 m total system length to focus proton beams with nominal energy up to 210 MeV. The system parameters for the rearranged 430 mm doublet configuration to focus a 210 MeV proton beam (now 1000 mm in length) are also listed in Table 4.3 as as the doublet with $E_0 = 210$ MeV. These were estimated using the same beam described in Sec.4.2.3 but with a nominal energy of 210 MeV. Note that this comes with significant reduction of the angular acceptance since the first PMQ needs to be moved downstream, but shows some flexibility of the transport even after the magnets are constructed.

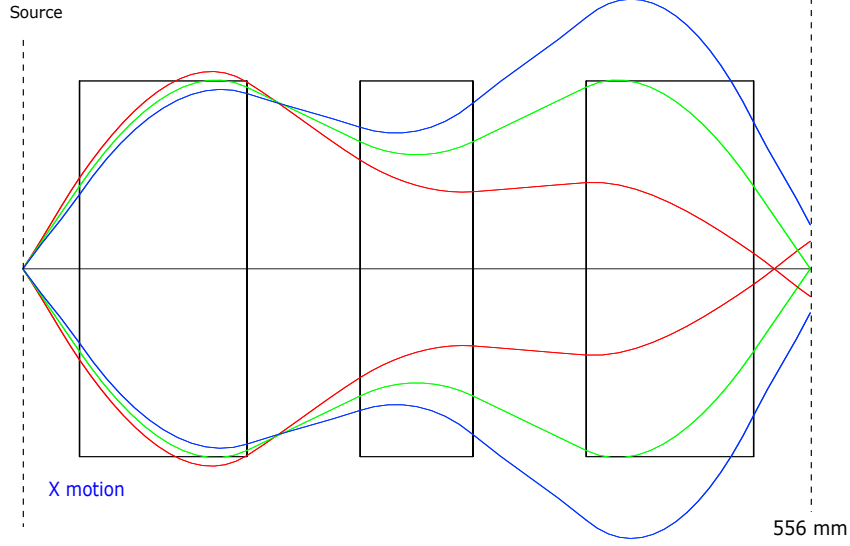


Figure 4.5: Illustration of the 560 mm triplet for $E_0 = 30$ MeV proton beam. The red, green and blue lines show the envelopes of $0.8 E_0$, E_0 , and $1.2 E_0$ proton beams. The half angle of the traces are 110 mrad for x and 17.5 mrad for y planes.

4.3.1.2 Triplet configuration improves beam size symmetry

The beam asymmetry can be improved by requiring the x and y magnification to be symmetric in the design (i.e. requiring $M_{11} = M_{33}$). This can be accomplished by adding another focusing magnet and thus another free parameter. The shortest triplet design with symmetric magnification ($M_{12} = M_{34} = 0, M_{11} = M_{33}$) and a system length of 560 mm is illustrated in Fig. 4.5. Note that the symmetric magnification does not mean that the x and y plane dynamics are identical. The beam divergence differs between the planes. For this design, all drift lengths were fixed to be the minimum length and all PMQ lengths L_1, L_2 and L_3 were treated as variables.

The system parameters and performance parameters for 0.56 m and 1.0 m triplets are shown in Table 4.3 and Table 4.5, respectively. While the solution for the 1.0 m triplet is not unique, D_2 and D_3 were kept minimum for comparison with the doublet performance. By comparing the shortest configurations, the triplet delivers the higher proton peak density

Table 4.5: Simulated beam transport results for different transport configurations, including the collection efficiency η , peak proton density n_{1pk} , energy acceptance δE , and FWHM beam sizes σ_x , σ_y at the output plane. The minimum achievable transport map coefficients are provided to highlight a given configuration’s symmetry with values closer to 1 in the x (M_{11}) and y (M_{33}) planes indicating point-to-point focusing and similar values indicating similar magnification. All configurations are designed with a nominal energy of $E_0 = 30$ MeV. The two configurations Quartet ($z=-200$) and Quartet ($z=+500$) are the same design as the 1 m Quartet design above it, but the performance is evaluated at a plane shifted from nominal focus. The energy acceptance for these are listed relative to the shifted spectral peak at these locations, 26 MeV (a) and 34 MeV (b). Results of the mirrored quartet (c) were simulated up to 5th order to ensure the accuracy of results.

Name	Length [mm]	η [%]	n_{1pk} [$10^9/\text{mm}^2$]	δE [MeV]	σ_{x1} [mm]	σ_{y1} [mm]	M_{11}	M_{33}
Doublet	430	2.2	18	0.75	0.84	0.034	7.3	0.14
Triplet	560	2.5	25	0.85	0.13	0.17	1.0	1.0
Quartet	610	1.5	24	0.85	0.15	0.19	1.1	1.1
Doublet	1000	2.3	2.0	1.4	2.1	0.23	17	1.2
Triplet	1000	1.5	5.1	1.4	0.36	0.53	2.8	2.8
Quartet	1000	1.3	6.6	1.2	0.34	0.35	2.4	2.4
Quartet ($z=-200$ mm)	800		11	1.7 ^a	0.38	0.48		
Quartet ($z=500$ mm)	1400		2.0	2.4 ^b	0.69	0.69		
Mirrored doublet	2000	2.3	23	0.85	0.105	0.22	1.0	1.0
Mirrored triplet	2000	1.5	21	0.65	0.13	0.17	1.0	1.0
Mirrored quartet ^c	2000	1.3	20	0.55	0.13	0.13	1.0	1.0
Quartet+Dipole	1000	1.6	5.3	0.85	0.344	0.342		

with much improved symmetry compared to the doublet, while the efficiency and the energy spread were comparable. When comparing the systems with the same length of 1 m, the triplet delivers again higher proton peak density with improved symmetry despite of significantly lower collection efficiency than the doublet. The energy spread was comparable. It is clear that some asymmetry still remains for the triplet designs. This is due to the asymmetry in the angular acceptance and chromatic aberrations. With insignificant cost to the available space, the triplet design would deliver better beam quality than the doublet for the applications envisioned for a laser-driven ion accelerator.

The drift lengths between the PMQs selected for these triplets can be changed to focus different energies in the same manner as studied for the doublet in the previous section. Extending the total system length to 1 m, the PMQs from the 560 mm triplet can be arranged to focus up to 117 MeV proton beams, and its system parameters are listed in Table 4.3 as the triplet with $E_0 = 117$ MeV. This energy is significantly lower than the doublet discussed in Sec. 4.3.1.1. If an application requires a wide range of energies including up to 200 MeV to be focused within the limited space, the doublet can be the best option, with the mentioned disadvantage of an asymmetric focus.

4.3.1.3 Improving magnification symmetry of the transport system with a quartet configuration

By adding a fourth focusing magnet, the magnification of the system, and thus the divergence of the beam at the output plane, can be made symmetric. The 1 m quartet design with symmetric magnification and divergence ($M_{12} = M_{34} = 0$, $M_{11} = M_{33}$, $M_{22} = M_{44}$) is illustrated in Fig. 4.6. The system parameters and performance parameters are shown in Table 4.3 and Table 4.5. The PMQs from the shortest quartet design (610 mm) can be arranged to focus 92 MeV proton beam with a 1 m total system length, and its system parameters are listed in Table 4.3 as the quartet with $E_0 = 92$ MeV.

One can see from Table 4.5 that the symmetry was further improved by the quartet designs for both shortest and 1 m cases, while other parameters were found to be comparable. While the energy acceptance, collection efficiency η , and energy acceptance δE of the quartet configurations that can be focused within 1 m was comparable to the triplet design, the added beam symmetry at the output can be beneficial. For the doublet and triplet configurations, the lower (higher) energy beam focus location in x and y planes are far from each other along

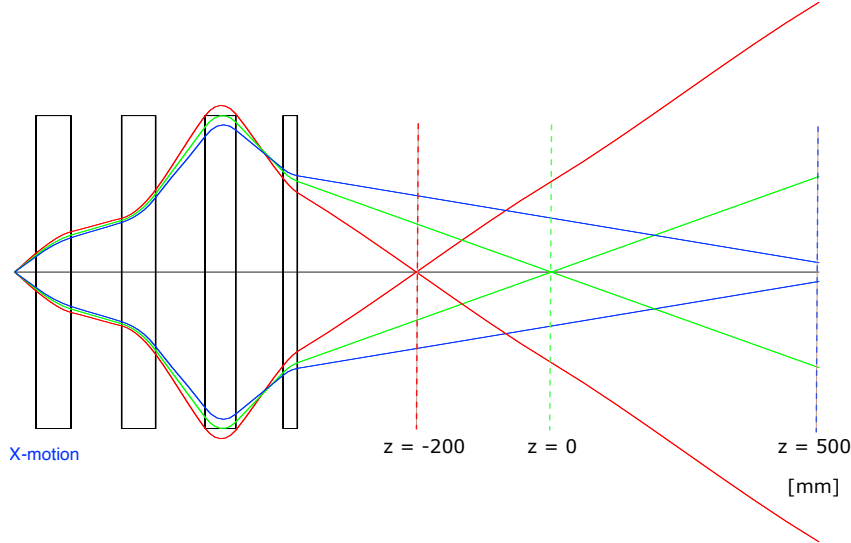


Figure 4.6: Illustration of the 1.0 m quartet for $E_0 = 30$ MeV proton beam. The red, green and blue lines show the envelopes of $0.85 E_0$, E_0 , and $1.15 E_0$ proton beams. The half angle acceptances of the traces are 28.5 mrad for x and 32.5 mrad for y planes. Indicated by the dashed red (blue) line represent the optimal sample locations for delivering a lower (higher) average energy beam.

z due to chromatic aberrations. In the quartet design, one of the leading terms for chromatic aberrations can be balanced between different planes along z , such as $M_{126} = M_{346}$ or $M_{226} = M_{446}$. For the 1 m quartet design, $M_{126} = M_{346}$ was also added to the requirements. With this, the quartet as a whole can focus more symmetrically, similar to an active plasma lens [79].

After other configurations are constructed, the longitudinal locations for the PMQs are the only free parameters that could be modified to vary the energy spectrum. For the quartet, it could more simply be done by varying the location of the sample to match the different focal position for a desired peak energy in the spectrum. This creates the effect of shifting the beam spectrum hitting the sample as off-energy particles would be defocused at these locations, lowering their relative intensity. The transverse profile and energy spectrum of the beam described in section B, transported with the 1 m quartet for different locations along z

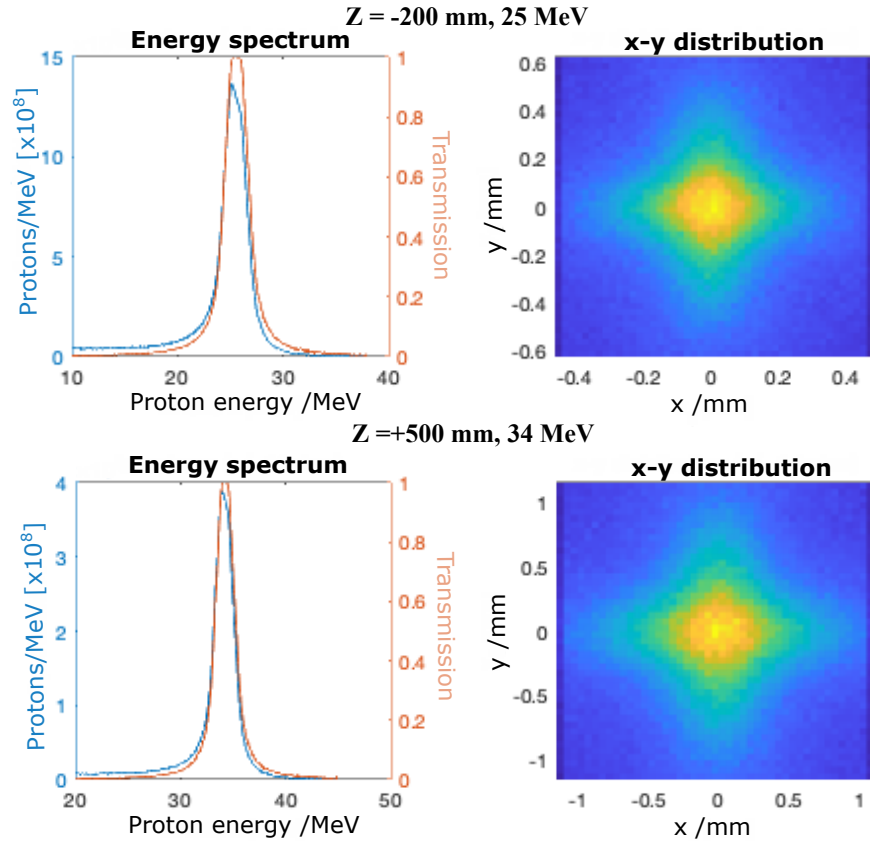


Figure 4.7: Simulated beam spectrum (left) and profile (right) at different target locations $z = -200$ mm (top) and $z = +500$ mm (bottom) relative to the 30 MeV focal location for the quartet design shown in Fig 4.6. This shows the target location can be used to tune the system to deliver different beam energies.

after the final PMQ, i.e, $z = -200$ mm (corresponding to a focused energy of 26.1 MeV) and $z = +500$ mm (corresponding to a focused energy of 34 MeV) with respect to the nominal output plane for a focused 30 MeV beam, are shown in Fig. 4.7, and performance parameters are listed in Table 4.5 as "Quartet ($z = -200$)" and "Quartet ($z = 500$)". Depending on the application, a rough spectral scan can be performed by moving the target location rather than moving each PMQs.

4.3.1.4 Mirrored design for 1 to 1 imaging

With the shortest designs, the magnification factor of the Quartet described in the previous section is close to 1 to 1 comparing the input beam with the transported beam at the output plane, and the 1 m Quartet design has a larger magnification as show in Table 4.5. When an application requires 1 to 1 imaging or a high proton fluence on the sample (keeping the first magnet close to the source for high collection efficiency) while the sample location is relatively far from the source, one can employ a mirrored design. This is simply repeating the same transport in a mirrored manner. Furthermore, an iris or pinhole can be placed at the first focus location to provide a narrower energy spread. Mirroring the system creates a new symmetry which can compensate for some higher order chromatic and spherical terms in the transfer map as shown in reference [96]. Shown in Table 4.5 is the performance estimate for the mirrored 1.0 m doublet (total length 2.0 m) with an iris opening matching the FWHM of the beam size. One can see that for all three configurations the mirrored design can provide similar peak proton densities and energy spreads. The doublet has a slightly higher peak density than triplet and quartet, while the quartet provides the lowest energy spread at the output plane. It is note-worthy that the mirrored design is 1-to-1 not only for imaging ($M_{11} = M_{33} = 1$) but also for divergence ($M_{22} = M_{44} = 1$). If an application requires a high peak density relatively far away from the source (≥ 3 m), the mirrored design becomes a reasonable option.

4.3.2 Controlling energy spread

The energy select-ability of PMQ-based focusing systems has been discussed in sections above, as indicated by the energy spread δE . This energy selection scheme is not perfect,

however, as a large number of the higher and lower energy particles can still make it through even if that constitutes a smaller fraction of the original particle numbers. As shown in Fig. 4.7 top left, the energy spectrum can have long low-energy tail. Some application may require complete removal of those high- and low-energy tails, and/or a narrower energy spread, e.g. for biological irradiation. Particles with different energies have different penetration depths and could lead to radiation damage at locations different from the targeted depth in the sample.

More precise energy selection can be realized by using dipole magnets in the transport beamline combined with a slit. By varying the slit location and size along the energy dispersion axis, one can control the energy and energy spread. However, this system introduces an energy dependent propagation angle, which may introduce inconvenience. Here we consider a pair of identical dipole magnets (dog-leg) and an optional slit. This way the propagation angle remains parallel to the input angle, although different energies of the beam now propagate along different axes with a lateral offset from the original propagation axis.

Illustrated in Fig. 4.8 is a 1.0 m quartet system with two 101.6 mm-long PMDs, its system and performance parameters and are shown in Table 4.3 and 4.5, respectively. The system was designed to satisfy $M_{12} = M_{34} = 0$, $M_{11} = M_{33}$, $M_{22} = M_{44}$, and is nearly identical to the 1m quartet design. Slight modifications in the magnet lengths are to compensate weak focusing forces from the PMDs. One can see that the energy spread was reduced from 1.05 to 0.85 MeV. Note that this is achieved without a slit, but by only taking into account the beam portion within the ± 1 FWHM beam size. The energy spread can be improved further by limiting the beam in the dispersion plane with a slit. The slight decrease in the peak density is from the removal of lower/higher energy particles contributions. From Fig. 4.8, the defocused 0.85 E and 1.15 E beams are still partially overlapped. The energy spread

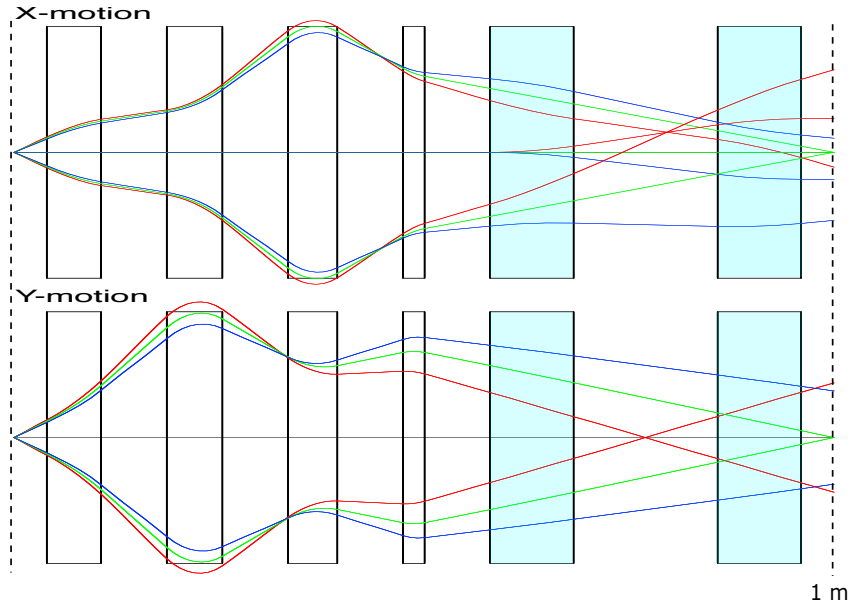


Figure 4.8: Illustration of the 1.0 m quartet with two dipole magnets from Sec. 4.1.2 with magnetic dispersion along the x axis (Dipole field oriented along y) for $E_0 = 30$ MeV proton beam. The red, green and blue lines show the envelopes of $0.85 E_0$, E_0 , and $1.15 E_0$ proton beams. The half angle of the traces are 28.5 mrad for x and 32.5 mrad for y planes. The dipole magnets are shown in blue.

can be improved by having longer drift length between two PMDs or using longer PMDs. Here, the total length was limited to 1 m to show what can be reasonably achieved within 1 m. Since the last drift lengths for the 1 m doublet and 1 m triplet are much longer, a narrower energy spread within the same length can be realized with only two dipoles. If an application demands a small energy spread while being compact, the doublet or triplet can become better options. Note that this design can also be mirrored to provide 1-to-1 imaging.

The energy spread can be better controlled using an Energy Selection System (ESS) as outlined in [83]. It consists of a set of four dipoles placed between the mirrored quadrupoles. Similar to a chicane bunch compressor or fragment separator, the dipoles are arranged to kick the beam off and back onto the longitudinal axis. Particles of different energies will take different paths through the system due to the velocity dependence of the Lorentz force and a beam block, or slit, can be arranged to only allow particles in a desired energy range

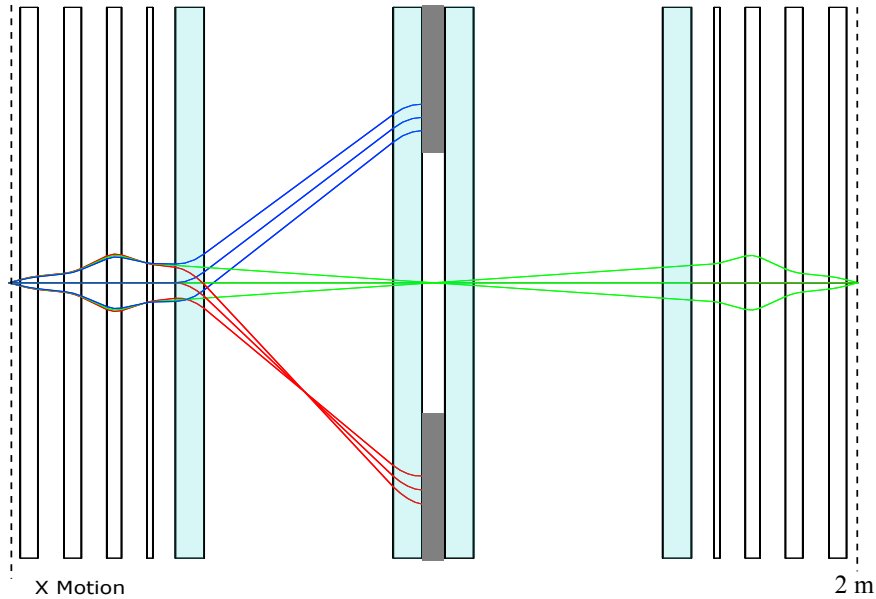


Figure 4.9: Mirrored quartet simple particle tracking. Higher energies (blue) and lower energies (red) are blocked by slit. Energy can be selected by changing magnet and slit (gray).

to pass through. A diagram of this design for the quartet is shown in Fig 4.9.

4.4 10 and 30 MeV Collimator designs for radiobiology at iP2

The previous work establishes the tools necessary to efficiently design beam transport systems for a variety of applications in laser-driven ion acceleration. Here, we present a beamline design suitable for radiobiology, particularly for high-dose-rate irradiation studies.

In radiobiological applications, uniform irradiation of samples is required to ensure accurate dose delivery. This necessitates a shift from point focusing to beam collimation to ensure a uniform beam spot, in this case, 7 mm in diameter. For thin biological samples (e.g. 2D cell cultures, mouse ears), the beam energy is able to be relaxed (10 MeV) to lower the necessary focusing strength of the transport while still achieving full penetration

Table 4.6: Magnet specifications for the 10 MeV and 30 MeV collimator schemes installed in iP2

iP2 magnet parameters	M1	M2	M3	M4
Inner radius (mm)	5	15	20	25
Gradient B' (T/m)	220	59.7	37.3	29
Effective length L_{eff} (mm)	50.25	50.10	57.90	60.10
Strength $B' \times L_{eff}$ (T)	11.0	2.99	2.40	1.92

in the sample. For thicker samples (> 1 mm) (e.g. peptides in solution), the beam energy needs to be higher in order to fully penetrate. The flexibility of the transport simulation tools discussed above enabled the development of a tailored design to meet these specific requirements.

A set of compact, permanent magnet quadrupoles (PMQs) were used for beam transport that had two configurations designed to collimate 10 MeV and 30 MeV proton beams, respectively. The first two PMQs were designed to collimate 10 MeV protons. A second set of PMQs could be moved into the beam path using linear stages to increase the overall focusing strength of the transport and for collimation of 30 MeV protons. The 30 MeV configuration allows the iP2 beamline to irradiate samples at larger penetration depths. After collimation, the beam is deflected downward by a permanent magnet dipole (0.5 T) for energy selection and spatial separation from the co-propagating neutrals and electrons. The specifications of the magnets are shown in 4.6.

The beam transport was designed to deliver as much dose to the sample as possible while maintaining a homogeneous dose distribution, both transversely and longitudinally, across the sample. To ensure longitudinal dose uniformity in the sample, there is a need to balance the energy spectrum so as to maximize the total charge delivered while applying an energy spectrum well away from the Bragg peak. The energy spectrum of the beam at the source

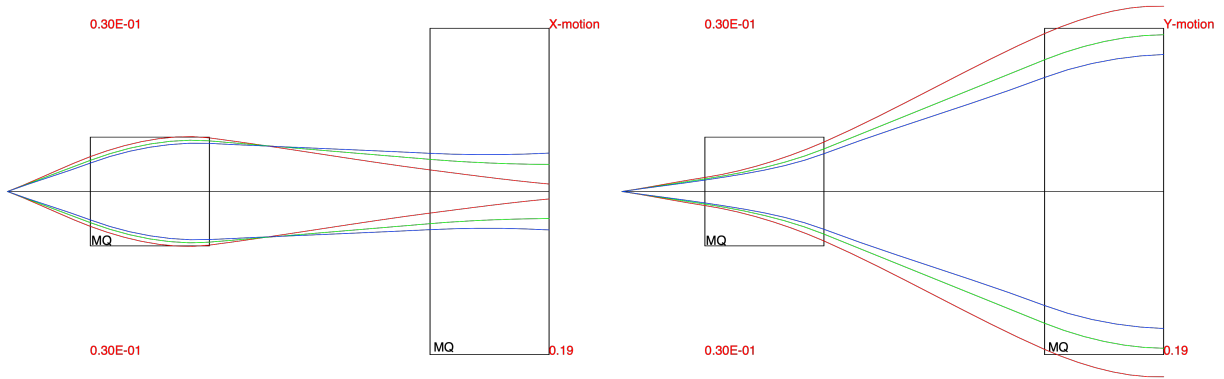


Figure 4.10: Illustration of the 10 MeV collimator for $E_0 = 10$ MeV proton beam. The red, green and blue lines show the trajectories for proton beams with energies of $0.8 E_0$, E_0 , and $1.2 E_0$ with the maximum accepted divergence in each plane ($x' = 82$ mrad and $y' = 33$ mrad for $E_0 = 10$ MeV)

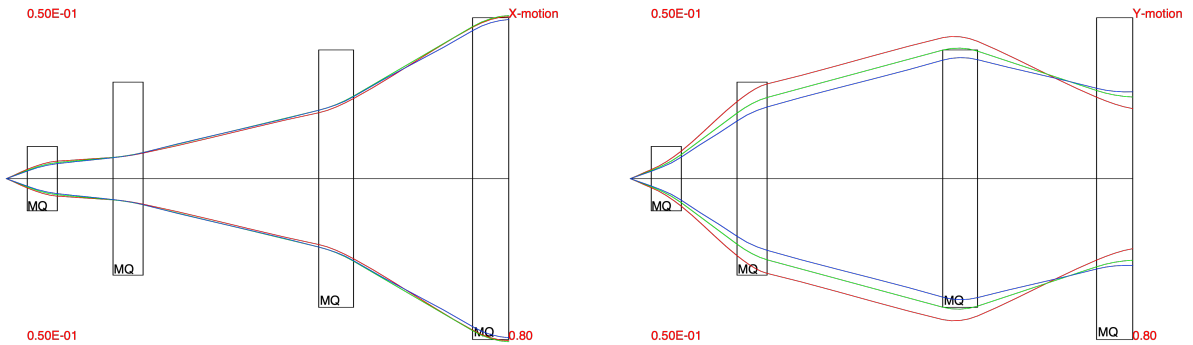


Figure 4.11: Illustration of the 30 MeV collimator for $E_0 = 28.5$ MeV proton beam. The red, green and blue lines show the trajectories for proton beams with energies of $0.8 E_0$, E_0 , and $1.2 E_0$ with the maximum accepted divergence in each plane ($x' = 37$ mrad and $y' = 36$ mrad for $E_0 = 10$ MeV)

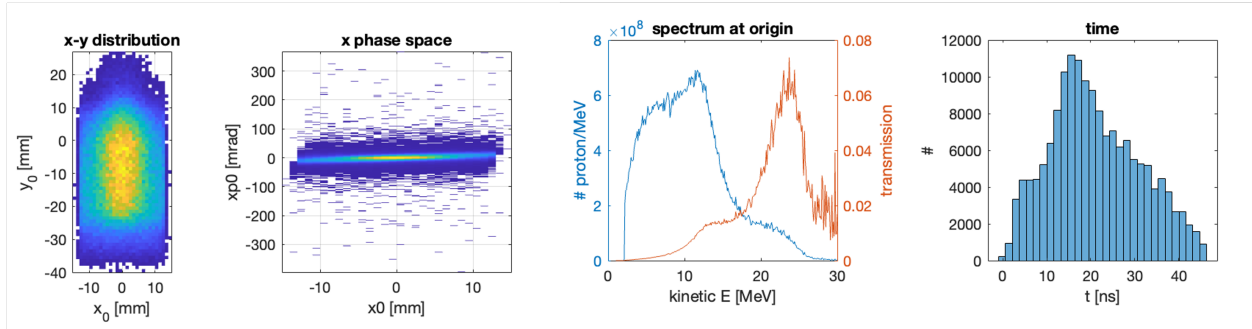


Figure 4.12: Monte Carlo simulation results of 30 MeV transport

is Maxwellian so the vast majority of the beam is of low energy (<10 MeV) and collecting only a small fraction ($<1\%$) of this part of the spectrum is enough to outweigh the energy deposited on the sample by the higher energy particles.

This design was implemented and used in an experiment at the BELLA Center’s iP2 beamline where the team irradiated *in vivo* samples to study ultra-high dose rate radiobiology, an application well-suited to LD ion beams due their high intensity. The results of this study and performance of the transport will be addressed in the following chapter.

4.5 Discussion

Presented here is a study of the collection and focusing of laser-driven proton beams with compact, permanent magnet-based beam optics. A wide range of compact designs were explored in this study, each with their own advantages and disadvantages. The doublet delivers the highest transport efficiency and can have the most compact footprint, but it suffers from an asymmetric beam spot at the output plane (sample site). The quartet produces the most symmetric beam spot at the sample site with a more uniform energy distribution, but is more costly than the other designs, because it requires more magnets, occupies more real estate in the experimental chamber, and is more prone to alignment

errors. Mirroring each configuration increases the proton spot quality and, thus, proton peak density at the sample site because of the compensation of aberrations, and allows for energy selection, either with just a slit or the energy selection system. This also doubles the number of magnets and total required length of the system. The choice of design thus depends on the application of the transport. We used the transport simulation tools established here to design a 10 MeV collimation system for the first *in vivo* normal tissue irradiation with laser driven protons.

For areas of future study, the effect of small perturbations or misalignment of the magnets on performance should be investigated along with other practical considerations like fringe fields. Although higher-order aberrations beyond the 3rd order were found to have minimal impact on beam performance, a more detailed investigation would be worthwhile. All the configurations still have rather significant chromatic aberrations which could affect the practicality of them for biological applications. A further study using higher order magnets (e.g. sextupoles and octupoles) to control for these effects should be done.

The work presented here is significant to the community of laser-driven ion beam researchers, as well as those involved in accelerator technology and high-energy physics. The designs developed in this study will enable more efficient ion collection and transport for LDIA applications ranging from cancer therapy to material science. Notably, the study provides a pathway to addressing the long-standing challenge of managing the large divergence and energy spread in a compact environment, which is a critical barrier to advancing LDIA technology.

Chapter 5. Implementation of beam transport for laser driven ion acceleration at the BELLA Center

Recently, LDIA have been utilized to explore the benefits of ultra-high dose rates in radiotherapy [97]. Irradiations with high dose rates ≥ 40 Gy/s have been shown to induce sparing of healthy tissues while maintaining equal tumor killing compared to conventional dose rate irradiations [16]. The FLASH effect is currently not well understood and its underlying mechanisms have not been fully explored due to limited access to conventional radiation sources that can achieve the necessary dose rates. An important open question currently is whether this effect is due to the instantaneous dose rate (dose delivered per pulse) or the average dose rate (dose delivered over the full exposure period) [5, 98].

Due to the ultra short pulse duration ($< \text{ps}$ at the source) of the beams they create, LDIA are well-suited to explore this effect. They also offer other potential benefits for use in radiotherapy. Their broadband energy spectra can be shaped to spread out the Bragg peak of the energy deposition, allowing for irradiation over a larger depth than with a conventional pencil beam scanning. Additionally, LD ion beams consist of multiple species, enabling access to different regimes of biological effectiveness.

To utilize LDIA for radiotherapy, the beams must be efficiently collected and transported to the sample location while maintaining their high intensity to achieve a high dose rate and uniform beam profile. The dose delivered to the sample also needs to be precisely monitored due to the inherent shot-to-shot variability of LDIA [99].

A previous radiobiology experiment at the BELLA Center was one of the first to deliver laser-driven protons to 2D cell cultures and showed a significantly higher survival rate of normal-cells compared to tumor-cells [29]. Using the BELLA PW's 13.5 m long focal length laser beamline (iP1) and a 1 mm diameter active plasma lens (APL) [79] to collect and focus the LDIA beam, the group was able to deliver proton pulses at ultra-high instantaneous dose rates of 10^7 Gy/s to cell monolayers over a 10 mm diameter spot size. However, this setup was limited in beam energy to ~ 2 MeV due to the achievable laser intensity at iP1. This beamline is optimized for generating laser-driven electron beams rather than ions. To be able to penetrate thicker *in vitro* and *in vivo* samples, the proton beam energy needed to be increased, requiring a higher laser intensity and more robust beam transport system.

Recently, an additional experimental chamber and short focal length laser beamline designed to deliver the higher laser intensities necessary for high energy laser-driven ion acceleration, called interaction point 2 (iP2), has been constructed [23, 24, 25]. This beamline has a sufficient intensity to generate proton beams at the energies necessary for irradiating thicker biological samples.

For this new laser beamline, a compact high-energy proton beam transport system is essential for further radiobiology studies of laser-accelerated proton beams. While the APL was sufficient for the iP1 setup, the small 1 mm diameter of the APL limits the overall collection efficiency of the ion beam, reducing the achievable dose per shot when moving to higher beam energies. Making the bore wider requires the use of unfeasible discharge currents. This motivated the use of permanent magnet quadrupoles which can achieve high field gradients (100s T/m) with a large bore (10-50 mm diameter), while remaining compact and requiring no bulky cooling system (as with superconductors) or high voltage (as with pulsed solenoids).

Presented here is the implementation of the two compact, permanent magnet-based beam transport configurations used to deliver laser-driven proton beams to *in vivo* and *in vitro* biological samples at the BELLA Center’s new iP2 beamline [25] in two recent experimental campaigns to explore ultra-high dose rate radiobiology. The two configurations differ by the nominal beam energy that they are designed to collimate. The original configuration, consisting of only the first two PMQs in Table 4.6, is designed to collimate 10 MeV protons and was used in the first *in vivo* experimental campaign. This campaign aimed to study radiation damage to normal tissue by irradiating mouse ear samples with LD proton beams at ultra-high instantaneous dose rates. In the followup campaign, the laser intensity was increased and the beam transport extended with a second pair of PMQs (M3 and M4 in Table 4.6) to increase the maximum beam energy in order to demonstrate iP2’s capability to irradiate thicker samples. In this second campaign, more mouse samples of different genetic strains were irradiated in addition to peptides dissolved in solution. The analysis of the biological results of these campaigns is ongoing, and beyond the scope of this thesis, but preliminary results are included to demonstrate the success of the campaigns and highlight the role of the beam transport implementation.

Also presented are the multiple ways we performed and verified the doses delivered to these samples. This was accomplished through the combination of calibrated radiochromic film (RCF) and an integrating current transformer (ICT) which were used to perform both online and off-line dosimetry.

5.1 The BELLA PetaWatt (PW) laser system

The experimental results presented in this chapter were acquired at the BELLA Center's PetaWatt (PW) laser system. The BELLA PW laser is a double-chirped pulse amplification (CPA)-based Ti:Sapphire laser system that can deliver up to 40 J of laser energy on target with a pulse duration down to ~ 35 fs (FWHM) with a maximum repetition rate of 1 Hz, making it one of the world's highest repetition rate PW lasers. A detailed discussion of the BELLA PW laser parameters including both spatial and temporal pulse properties is given in [20].

On the 13.5 m long focal length beamline, the final off-axis parabolic (OAP) mirror focuses the laser beam to a spot size of $52 \mu\text{m}$, yielding a peak intensity of $\sim 1.7 \times 10^{19} \text{ W/cm}^2$ [20]. Previously, high charge proton and ion beams had been accelerated with the BELLA PW up to 8 MeV energies with the long focal length beamline and $5 \mu\text{m}$ thick Ti [100].

5.1.1 High intensity beamline and target chamber, iP2

In 2022, the BELLA PW laser beamline was extended with an additional target chamber and beamline with a 0.5 m short focal length ($f/2.5$) off-axis parabolic mirror (OAP) in order to reach ultra-high laser intensity [25]. A schematic of the iP2 beamline and target chamber is shown in Fig. 5.1.

The OAP focuses the beam down to a focal spot size $w_0 = 2.3 \mu\text{m}$ ($2.7 \mu\text{m}$ FWHM) in both horizontal and vertical directions. At maximum compression (40 fs) and beam energy (40 J), this corresponds to final laser intensity of $I_L = \frac{2P_L}{\pi w_0^2} = 7 \times 10^{21} \text{ W/cm}^2$. The laser and This laser intensity is relevant for discovery research in high energy density science (HEDS),

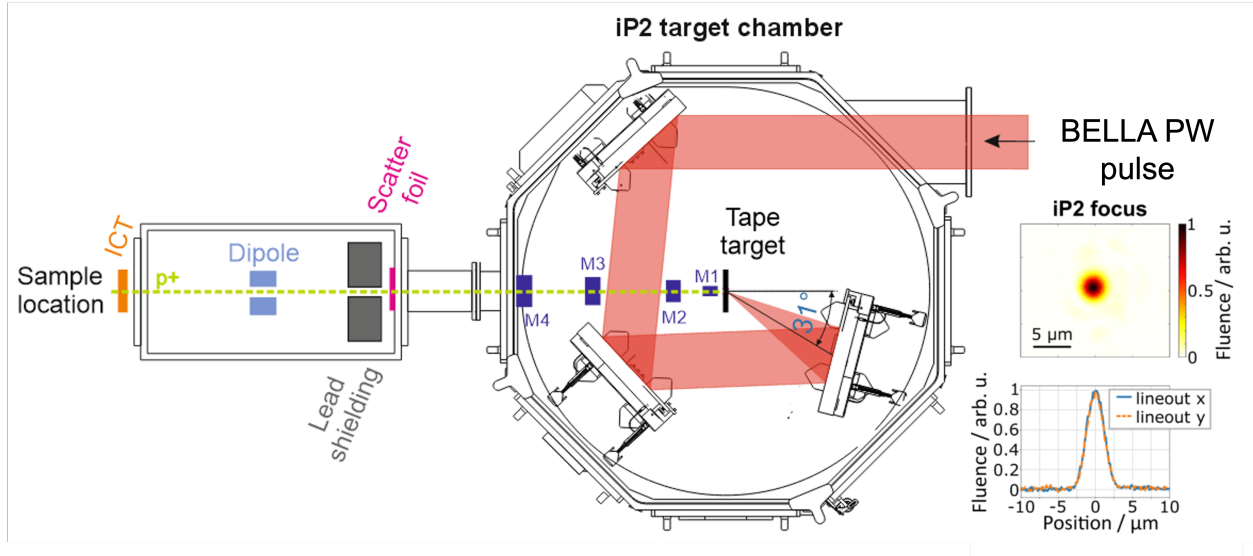


Figure 5.1: The iP2 target chamber setup for radiobiology experiments. The laser focal spot and intensity profile (measured at low power) are shown to the right of the chamber. The laser incidence angle on target was 31 deg with respect to the target normal to avoid having back reflections propagating back through the beamline and potentially damaging the laser. Adapted from [25].

ion acceleration, and strong field QED, as well as applications, e.g., in radiobiology and material science research.

5.2 Experimental setup and beam transport

An illustration of the proton beamline and experimental setup is shown in Fig. 5.2.

The BELLA PW laser was used to deliver pulses to a custom-designed tape drive target system where protons were accelerated in the laser interaction with the 13 μm thick Kapton tape via Target Normal Sheath Acceleration (TNSA).

For the first *in vivo* experiment, the laser was operated at 7 J, 60 fs pulse length, and defocused to a spot size of $w(z = +50 \mu\text{m}) = 6.1 \mu\text{m}$ optimized for the stable delivery of 8 MeV protons to the sample site at 2 Gy per shot. The laser operated at a reduced repetition rate of 0.05 Hz due to the time required to perform online dosimetry and advance the tape

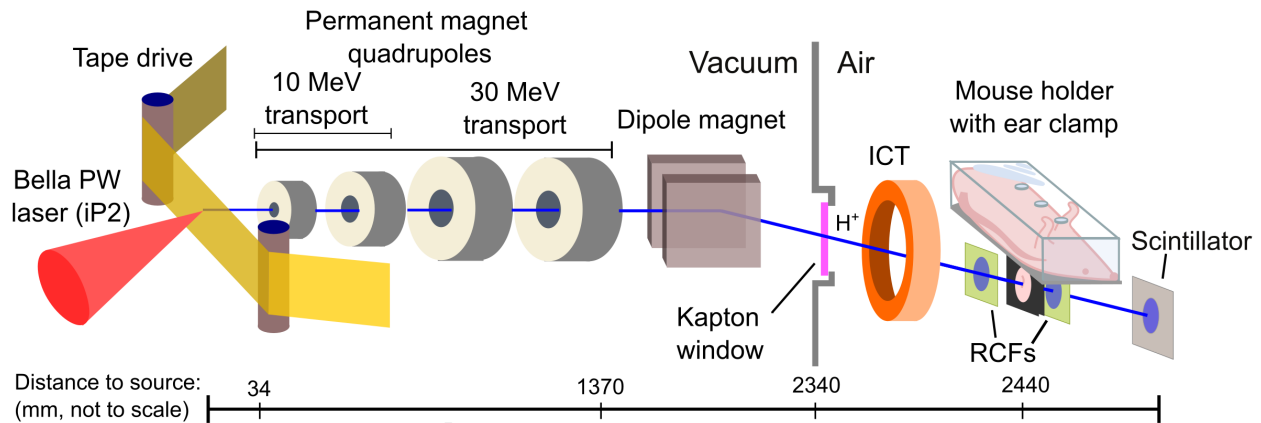


Figure 5.2: (a) Illustration of experimental setup for mouse ear irradiations. Components and distances are not to scale. The beam transport has two configurations designed to collimate 10 MeV and 30 MeV proton beams, respectively. The quadrupole magnets are mounted to motorized stages to easily switch from the 10 MeV transport to the 30 MeV transport by moving the additional quads into the beam path. The ICT is used to perform online dosimetry and is calibrated against RCFs placed at the sample location. RCFs are placed in front and behind each individual mouse ear sample during irradiation to verify the delivered dose.

drive to a new position to be fired upon.

For the second experimental campaign, the laser operated with 22 J pulse energy and 37 fs pulse length to achieve the higher intensity necessary to accelerate 30 MeV protons. It also operated at a higher repetition rate (0.2 Hz) after further automating the online dosimetry and improving the tape drive advancement software.

A set of compact, permanent magnet quadrupoles (PMQs) were used for beam transport that had two configurations designed to collimate 10 MeV and 30 MeV proton beams, respectively. The first two PMQs were designed to collectively collimate 10 MeV protons. A second set of PMQs could be moved into the beam path using linear stages to increase the overall focusing strength of the transport in order to collimate 30 MeV protons. This higher energy configuration allows for the irradiation of samples with larger penetration depths at the iP2 beamline.

After exiting the last PMQ, the beam passes through a 1 cm diameter aperture and

through a 25 μm thick Kapton foil to filter heavier ion species originating in the laser-target interaction, in addition to smoothing the proton beam profile at the sample site via scattering in the foil. The beam is then deflected downward by a permanent magnet dipole for energy selection and spatial separation from the co-propagating neutrals (X- and gamma rays) and electrons.

Lead shielding was implemented surrounding the proton beam axis that blocked x- and gamma rays along the direct line of sight between the laser target and the sample location.

The proton beam exits the vacuum chamber into air through a 25 μm thick Kapton window before passing through the aperture of the integrating current transformer (ICT) used to measure the charge delivered to the sample and perform online dosimetry (see ?? for more details). Before reaching the sample, the beam is collimated by a 7 mm aperture to shield the sample and define a consistent exposure area on the sample. Radiochromic film (RCF) was placed behind (and in front for the second campaign) of the samples to record the accumulated dose and profile over the entire irradiation. Finally, a scintillator placed behind sample holder was used to monitor the beam profile on-shot.

5.2.1 Magnet characterization and installation

The first two PMQs, M1 and M2, were manufactured and characterized by RadiaBeam. The integrated field strengths and gradients were measured with a 1D Hall probe by the manufacturer. The later two magnets, M3 and M4, were manufactured by Radial Magnets but were not fully characterized. Magnetic field measurements were taken at LBNL using a Hall probe (F.W. Bell 5170 transverse probe) in order to verify the field strength and gradient as shown in Fig. 5.3. The measured magnet parameters are shown in Table 4.6.

The magnets were installed on 4-axis tilt aligner stages (Newport 9071-V) to manually

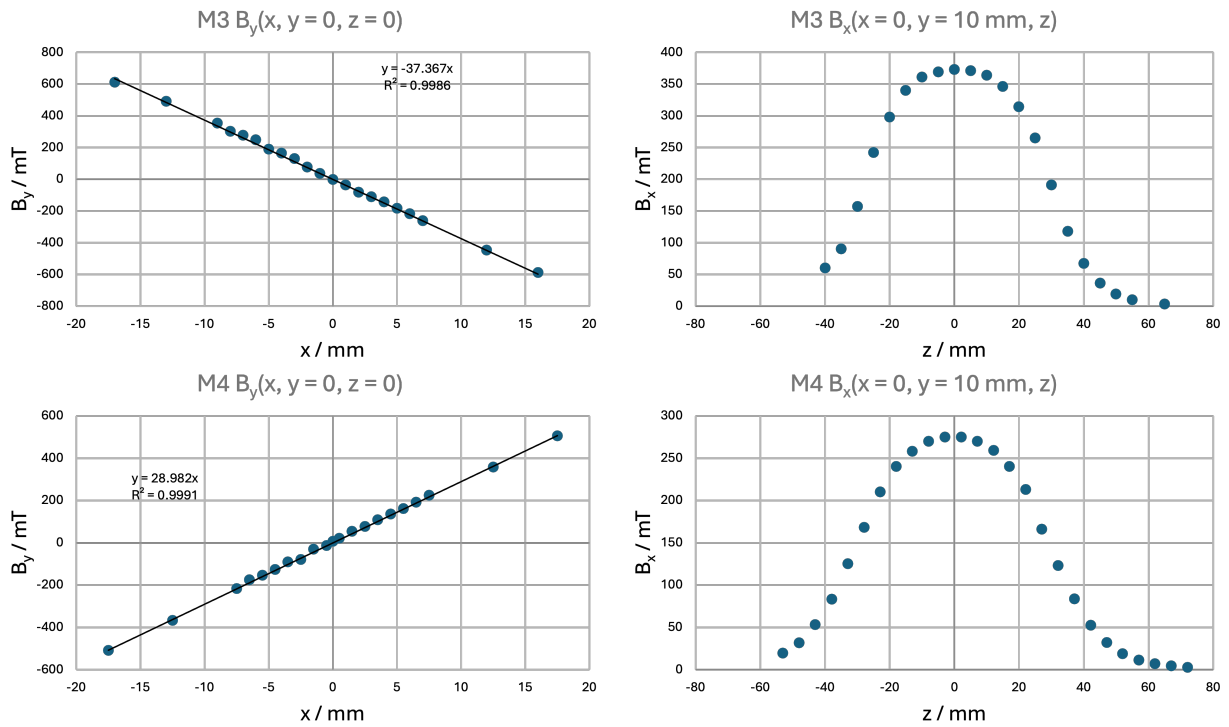


Figure 5.3: Hall probe measurements of the magnetic field inside the bore of magnets M3 (top) and M4 (bottom). The field gradient of each magnet (left) was verified by taking a linear fit of the magnetic field. The integrated field strength was estimated by integrating over field measurements taken 10 mm off the central axis.

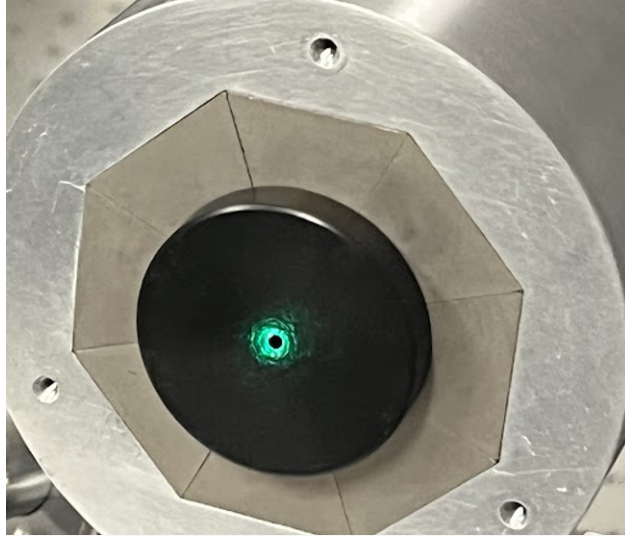


Figure 5.4: The longitudinal axes of the PMQs were aligned to the beam axis defined by a reference laser beam (green). Black plastic plugs with 1 mm diameter holes machined through the center were inserted into the bore of the magnet to act as irises for more accurate alignment.

adjust the yaw and pitch. These were then placed on motorized translation stages that could be remotely operated by the BELLA control system to move the magnets in and out of the beam path when necessary.

The magnets were aligned to a central beam axis defined by a reference laser beam that was independently aligned to the nominal proton beam axis normal to the tape target surface. Insertable plastic plugs were fixed on either side of the magnets with 1 mm holes machined at their center to act as irises in order to better align the central axis of the magnets to the reference laser. For each magnet, the position, yaw, and pitch were adjusted iteratively until the laser propagated through the center of both irises with minimal reflection.

5.3 Beam transport performance

In January of 2023, the first *in vivo* animal models were irradiated with ~ 8 MeV laser-driven protons to investigate radiation damage to normal tissue at ultra-high instantaneous

dose rates.

In April of 2024, a followup experiment was conducted to establish the capability of irradiating samples at higher ion energies, up to 30 MeV. Going to this energy is necessary to irradiate thicker samples uniformly.

5.3.1 Improved charge collection

The beam transport system successfully delivered over 1 Gy/shot to the samples in both experiments while maintaining a uniform dose profile. Measurements of the proton charge at the sample site with and without collimating the proton beam shows a roughly fourfold increase in charge with the transport, resulting in more than 1 Gy per shot on the samples.

The wide bore and strength of the PMQs allowed a large amount of charge to be collected, increasing the overall dose rate achievable at iP2.

A comparison between the charge collection with and without the two beam transport configurations is shown in Fig. 5.5. The charge was measured by the ICT placed immediately in front of the sample but before the beam was fully collimated by the 7 mm aperture. The figure shows the average charge collected over five shots as a function of the target position relative to the laser focus, z . The error bars represent the full range of charge reaching the ICT over five shots for each target position.

This scan of the target z position was done to determine the optimum position with the goal of both maximizing the dose and minimizing the shot-to-shot variability, but ultimately revealed interesting and unexpected results.

First, it is evident that the 10 MeV transport significantly increases the amount of charge reaching the ICT. At the best target location ($z = -150 \mu\text{m}$), the 10 MeV transport delivers 16 times more charge than with no transport present.

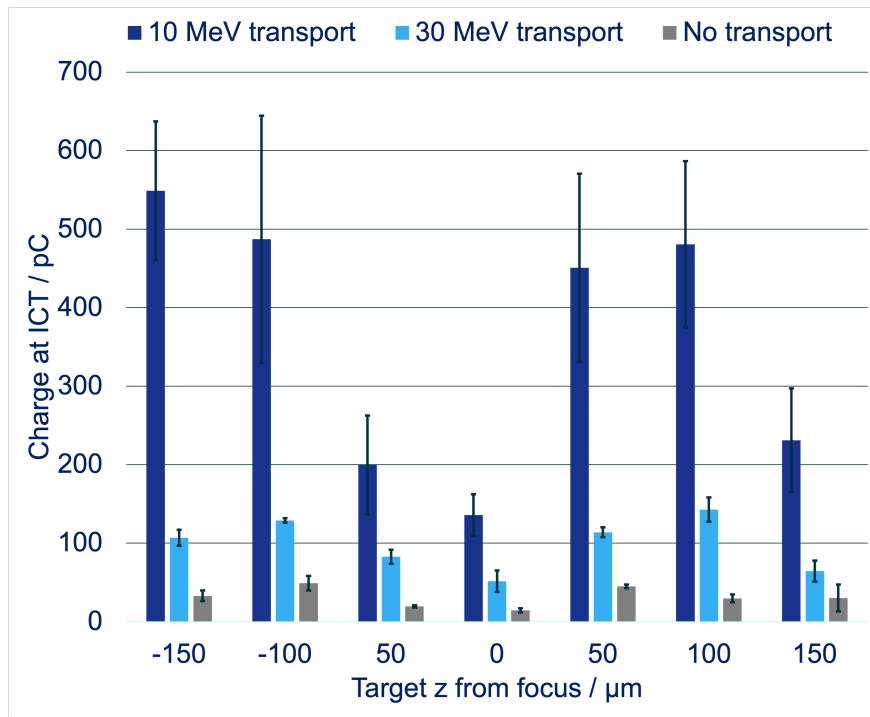


Figure 5.5: Comparison of the charge collected by the transport configurations as measured by the ICT placed before the sample, shown for different tape target positions relative to the laser focus. The error bars represent the full range of charge measured by the ICT over 5 shots for each target position.

The 30 MeV transport increases the charge delivered but less significantly than the 10 MeV transport. At best case ($z = 100 \mu\text{m}$), the 30 MeV delivers 4.8 times more charge than with no transport present. This is because the 30 MeV transport is designed to deliver a higher energy portion of the Maxwellian beam spectrum. The initial TNSA beam has orders of magnitude higher charge at lower energies than at higher ones. Due to the additional magnets in the 30 MeV transport, the lower energy part of the spectrum is effectively filtered resulting in less overall charge.

An interesting but unexpected result shown in Fig. 5.5 is the reduced charge measured by the ICT at target positions closest to focus. This is true with and without the transports moved in the beam path. TNSA theory predicts higher proton production with increasing laser intensity. The laser intensity impinging on the target is highest at focus so one would expect the highest charge when $z \sim 0$.

While it is unclear why we have seen the opposite behavior, it may be due to the TNSA-generated beam not being perfectly normal to the target surface at the highest laser intensities. Non-target-normal emission of protons has been reported when using ultra-high laser intensities at oblique incidence [101]. The ICT measures the beam charge after 2 m of propagation and after a lead aperture which may have blocked the main part of the beam if it was generated off the target normal direction. Future work should focus on determining the emission angle of the highest proton energies to better align it to the transport axis. This could be explored by rotating the target relative to the laser.

5.3.2 Uniform beam profile

The beam transport was designed to deliver as much proton dose to the sample as possible with a compact permanent magnet system while maintaining a homogeneous dose distribu-

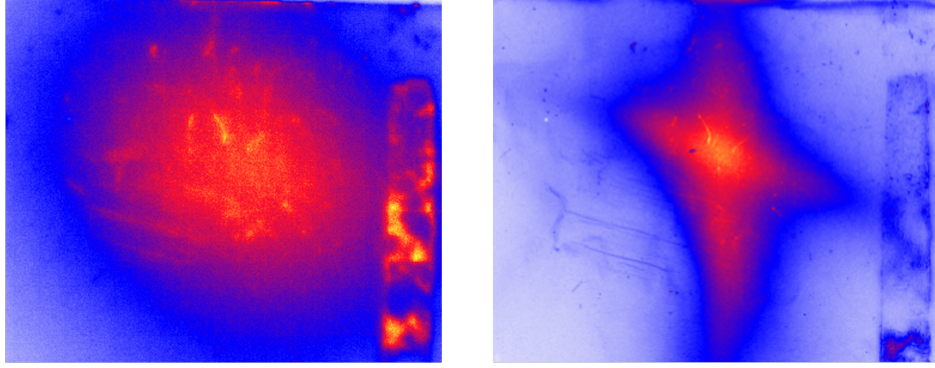


Figure 5.7: Comparison of the beam profile at the sample location as measured by the scintillator with (left) and without (right) the scattering foil in place. The foil effectively smooths out the beam profile to improve the lateral dose uniformity on the samples.

tion across the sample. Simulations of the transport ensured the correct placement of the transport elements to achieve a uniform dose profile.

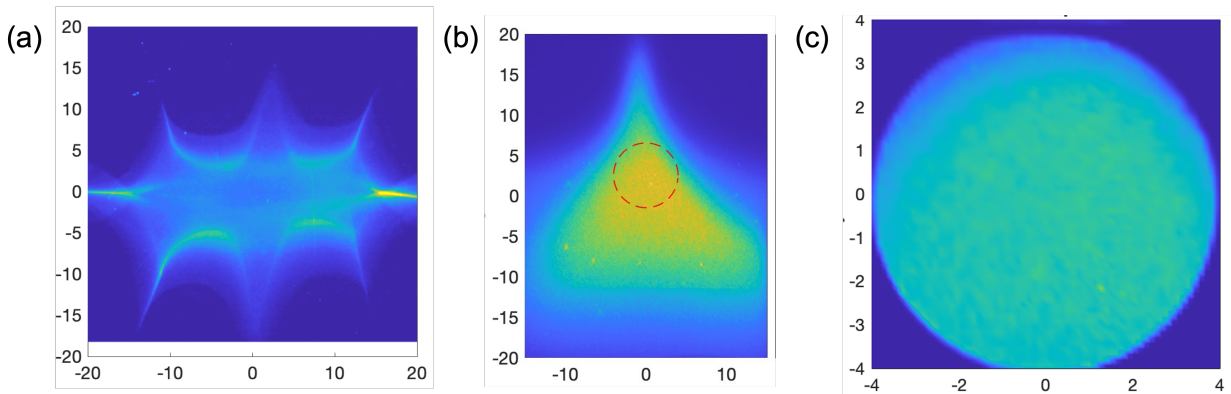


Figure 5.6: Beam profiles measured by RCF placed after the 10 MeV transport (a), at the sample location but before the final aperture shown in red (b), and at the sample location in the ear clamp (c). All distances are in mm.

The beam profile was also measured at various points along the beamline using RCF. A selection of them are shown in Fig. 5.6.

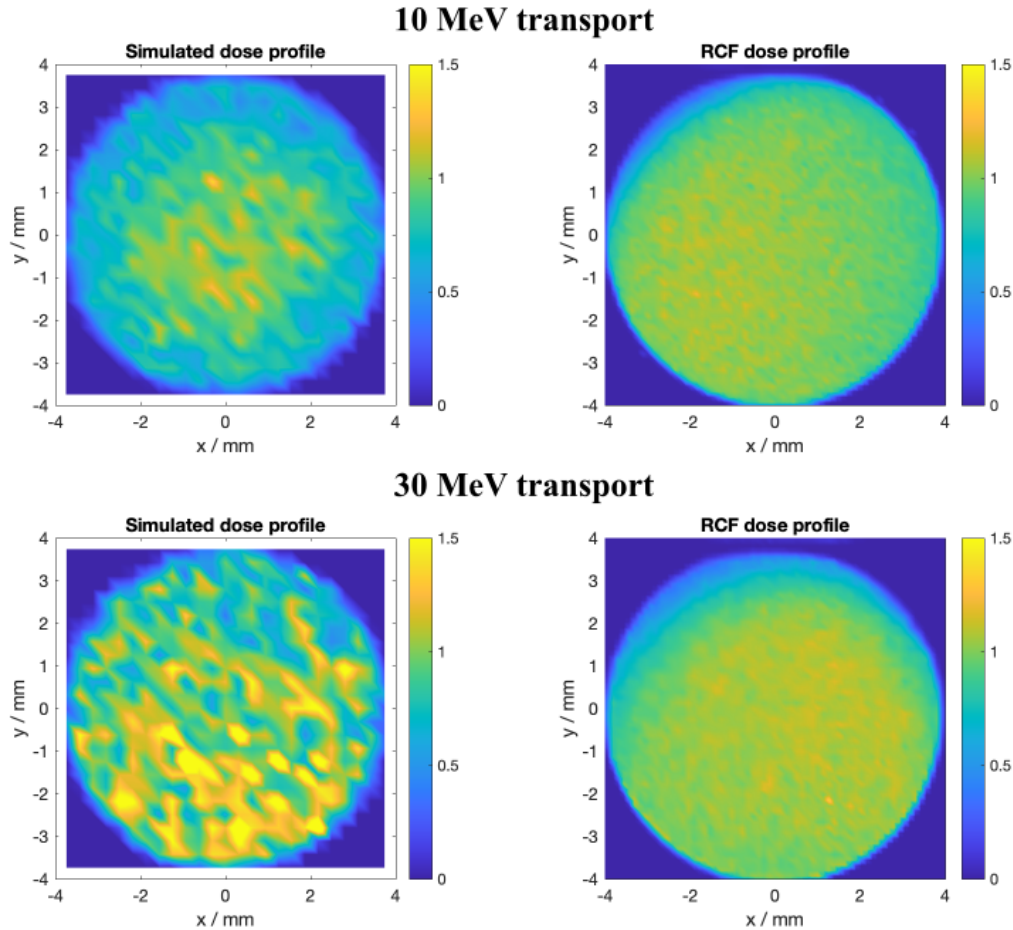


Figure 5.8: Comparison of simulated (left) and measured (right) dose profiles at the sample location, normalized to mean dose for the two transport configurations 10 MeV (top) and 30 MeV (bottom). The color bars are normalized to the mean dose in each profile.

Fig. 5.8 shows a representative of the simulated and measured beam profiles at the sample location for the two beam transport configurations. The overall lateral dose variation when using the 10 MeV transport was measured to be 7%, as measured by multiple RCF placed *in situ*. The 30 MeV transport delivered a less uniform beam during the 2024 campaign, with a lateral dose variation of 14%. This difference can be seen in Fig. 5.8 as there is slightly less dose deposited at the top of the profile in the 30 MeV case than in the 10 MeV case. This is likely due to the broader beam spectrum used in the latter case.

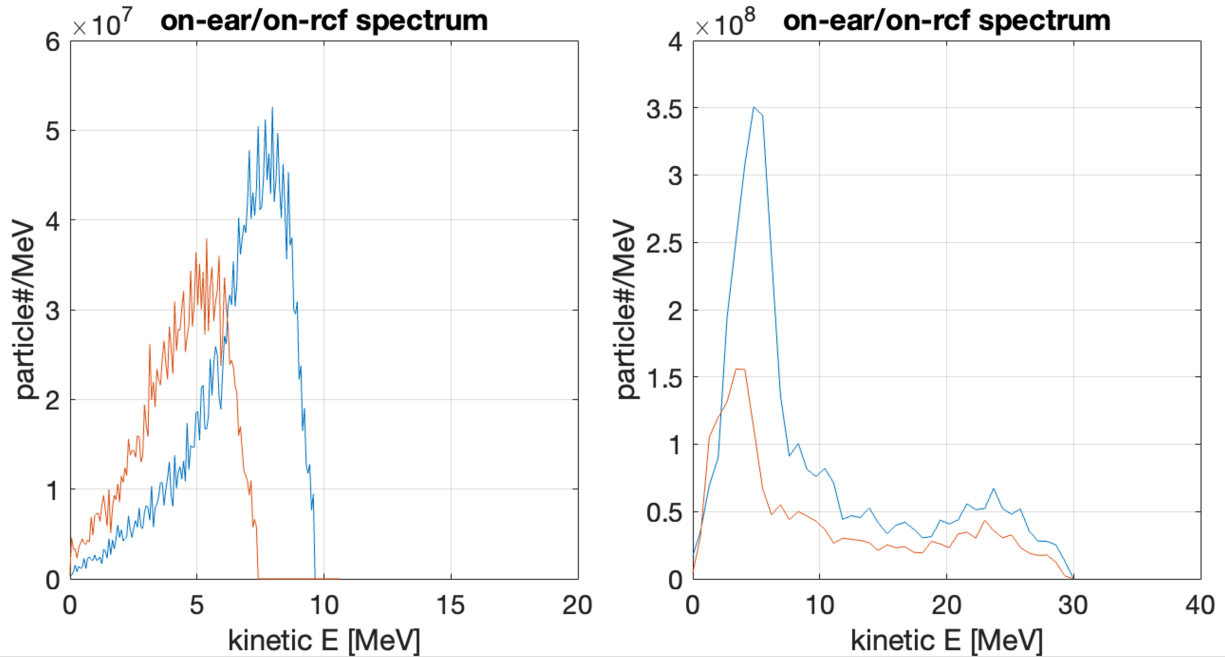


Figure 5.9: MC simulated proton spectra of the beam used in the 2023 campaign (left) and the measured proton spectra of the beam used in the 2024 campaign (right). Shown are both the beam spectra as delivered to the mouse ear (blue) and the spectra that reached RCF used for dosimetry following the sample.

The dipole magnet angularly disperses the beam by energy meaning higher energy protons will pass through the top of the sample while lower energy particles will pass through the bottom. As there were significantly more low energy particles than high energy particles in the 2024 campaign (see Fig. 5.9) and due to the fact that lower energy particles deposit more dose than high energy (higher LET), more dose is deposited in the bottom of the sample than at the top. The angle of the sample holder and the dipole were adjusted between the campaigns to account for this effect but this effort was limited due to geometric constraints.

5.4 Dosimetry of laser-driven protons for *in vivo* samples

At the BELLA Center’s iP2 beamline, we implemented a suite of diagnostics used for dosimetry. These diagnostics include multiple integrating current transformers (ICTs) for online charge measurements and calibrated radiochromic films (RCFs) to measure the dose profile and calibrate the ICT dosimetry. Monte-Carlo (MC) simulations of the beam allowed for us to predict the dose received by the sample and correct the linear energy transfer (LET)-dependent response of the RCFs.

5.4.1 Online dose monitoring with an Integrating Current Transformer

Dosimetry was performed during irradiation, and verified after, through a combination of on-shot charge measurements with an Integrating Current Transformer (ICT), accumulated dose measurements with RCFs, and Monte Carlo simulations of the beam.

Because the dose per proton bunch (shot) was limited to 1-2 Gy, the samples were irradiated with multiple pulses to reach the doses relevant for clinical radiation therapy (10-40 Gy). Due to the large shot-to-shot fluctuations of the proton bunch charge, online dosimetry needed to be performed to accurately apply the prescribed dose to each sample. For each shot, the delivered dose was estimated using the charge measured by the ICT (Bergoz model: ICT-122-070-05:1) placed before the sample. Before first biological samples were irradiated, and at least once per day over the course of the campaign, the dose measured by an *in situ* RCF placed into the sample holder was correlated to the summed charge

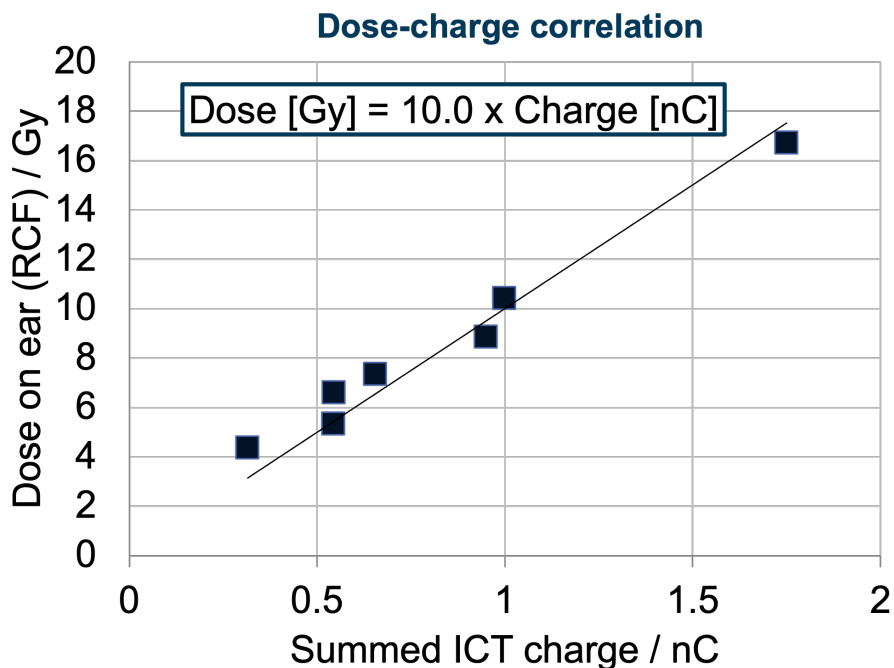


Figure 5.10: The charge-to-dose calibrations used to perform online dosimetry. The charge per ion pulse as measured by the ICT was correlated to the dose measured by RCF placed *in situ* and used to estimate the dose delivered on shot to account for any shot-to-shot fluctuations in the beam intensity. Data was accumulated over multiple shots.

measured by the ICT over multiple shots to establish a charge-to-dose conversion (see Fig. 5.10). This process has been used in radiobiology experiments at the BELLA Center before and is explained more in [99]. This technique allowed us to monitor the dose we delivered on each shot and adapt the number of shots to reach the prescribed dose for each sample (see Fig. 5.11 for examples).

Thanks to our adaptive irradiation protocol guided by online dosimetry, the sample-to-sample-variation (SSV) could be reduced to 5% (see Table 5.1), significantly lower than the 17% SSV in our previous study [29].

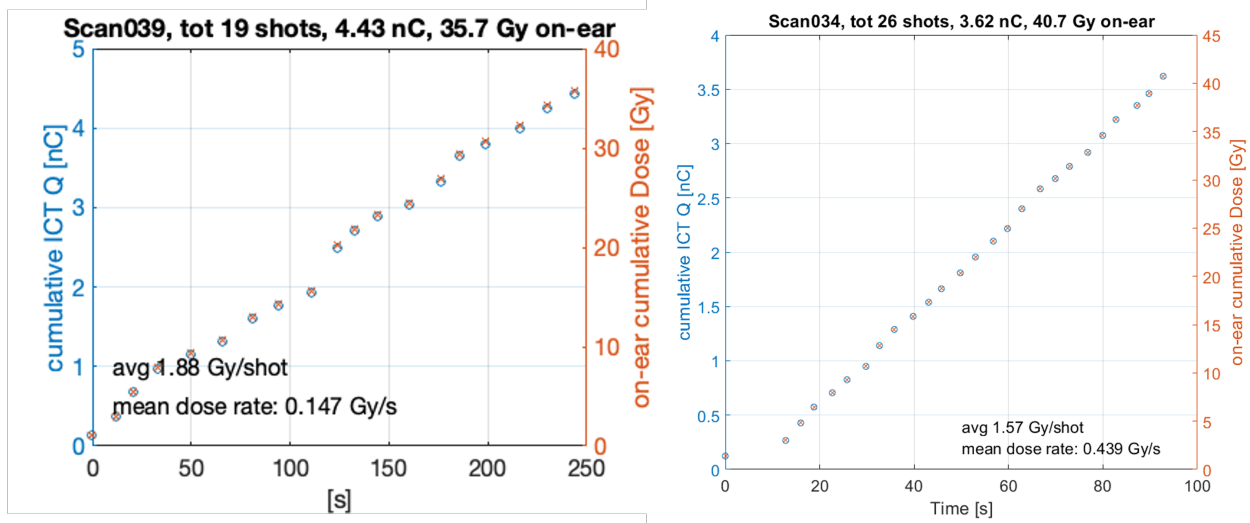


Figure 5.11: Accumulated charge and dose delivered to two of the mouse samples in 2023 (left) and 2024 (right).

5.4.2 Absolute dosimetry using radiochromic film

Radiochromic film (RCF, Ashland EBT-3) was used to verify the absolute dose delivered to samples and monitor the beam uniformity. These could only be processed after irradiation due to the time it takes for RCF to develop and be analyzed.

In the first experimental campaign, a film was placed at the back of the sample holder (17 mm from the sample). Monte Carlo simulations of the beam were used to convert the dose measured by this film to the dose applied to the sample and account for the LET-dependent response of the RCF. This process was iteratively improved through the course of the two campaigns.

The conversion factor $f(Q)$ between the dose value measured by the RCF M and the dose applied to the sample D_S is given by,

$$f(Q) = \frac{D_S}{M}. \quad (5.1)$$

This factor can be estimated by performing Monte Carlo simulations of the beam and modeling the energy deposited in tissue (approximated as water) and the active layer of the RCF (approximated as polycarbonate). It is dependent on the beam spectrum, represented by Q , due to the attenuation of the beam in the sample and air between the sample and the film.

The LET-dependent response of the RCF also needs to be taken into account. The MC model was updated to also calculate the dose that would be measured by the RCF M by scaling the energy deposited by each particle in the RCF active layer according to the factor η from 3.3.

By calculating both the expected dose on the RCF without LET dependence D_{film} and the expected dose with the LET-dependent under-response M , the measured dose can be scaled by a factor f_{LET} to represent the overall LET-dependent response of the film,

$$f_{\text{LET}} = \frac{D_{\text{film}}}{M}. \quad (5.2)$$

Thus the overall conversion factor between the measured RCF dose and the dose applied to the ear is,

$$f(Q) = \frac{D_S}{M} = \frac{D_S f_{\text{LET}}}{D_{\text{film}}}. \quad (5.3)$$

This factor is dependent on the beam spectrum Q which fluctuates both shot-to-shot and between irradiation days due to the differences in laser tuning. This is due to a variety of factors. These factors impact the electron temperature in the laser-plasma interaction which shifts the proton cutoff energy E_{max} and temperature E_{th} in the ion beam spectrum.

The ion beam spectrum was measured using a stack of RCF 52 mm from the tape target which gave an initial estimate of the temperature $E_{\text{th}} = 1.1$ MeV and cutoff energy $E_{\text{max}} = 10.6$ MeV. However, putting this beam spectrum into the MC model did not match

RCF measurements.

The ratio between the doses measured by the RCFs that were placed behind the sample were used as indirect spectral measurements to better determine the range of spectra to input into the MC model.

The ratio between the dose measured by RCF1 M_1 and RCF2 M_2 across the samples was found to vary with an average value of $M_1/M_2 = 6.6 \pm 1.2$. The spectral parameters E_{th} and E_{max} were varied to try to reproduce this ratio in simulation while accounting for the LET-dependent response of the film measurements.

Relying solely on films placed behind the sample introduced challenges in the dosimetry. As there is variation in both the geometry of the sample volume (ear thickness, number of veins, hair present) and the intensity and spectrum of the beam, the dose deposited onto the film is not perfectly correlated with the dose applied to the sample. Some of the films placed behind the sample showed irregular beam profiles. Cross-referencing these profiles and photographs of the sample in the holder revealed cases where tufts of hair or skin folds were present in the beam path, affecting the dose applied and the film measurement. In these cases, we had to rely on the dose estimated by the calibrated ICT. Thus, the absolute dose values are a combination of both the ICT and film measurements.

In the second campaign, a set of RCFs were placed directly in front (RCF-A) and behind (RCF-C) the *in situ* RCF (RCF-B) at the sample location during the ICT calibration shots to obtain conversion factors between the doses measured by RCFs A and C to the sample dose. Subsequently, new RCFs A and C were also placed in front and behind each of the samples during irradiations to verify the dose applied to each sample.

In order to obtain the actual dose measured by each RCF, the raw dose values were scaled according to the film detection efficiency η (Eq. 3.3). The average stopping power of

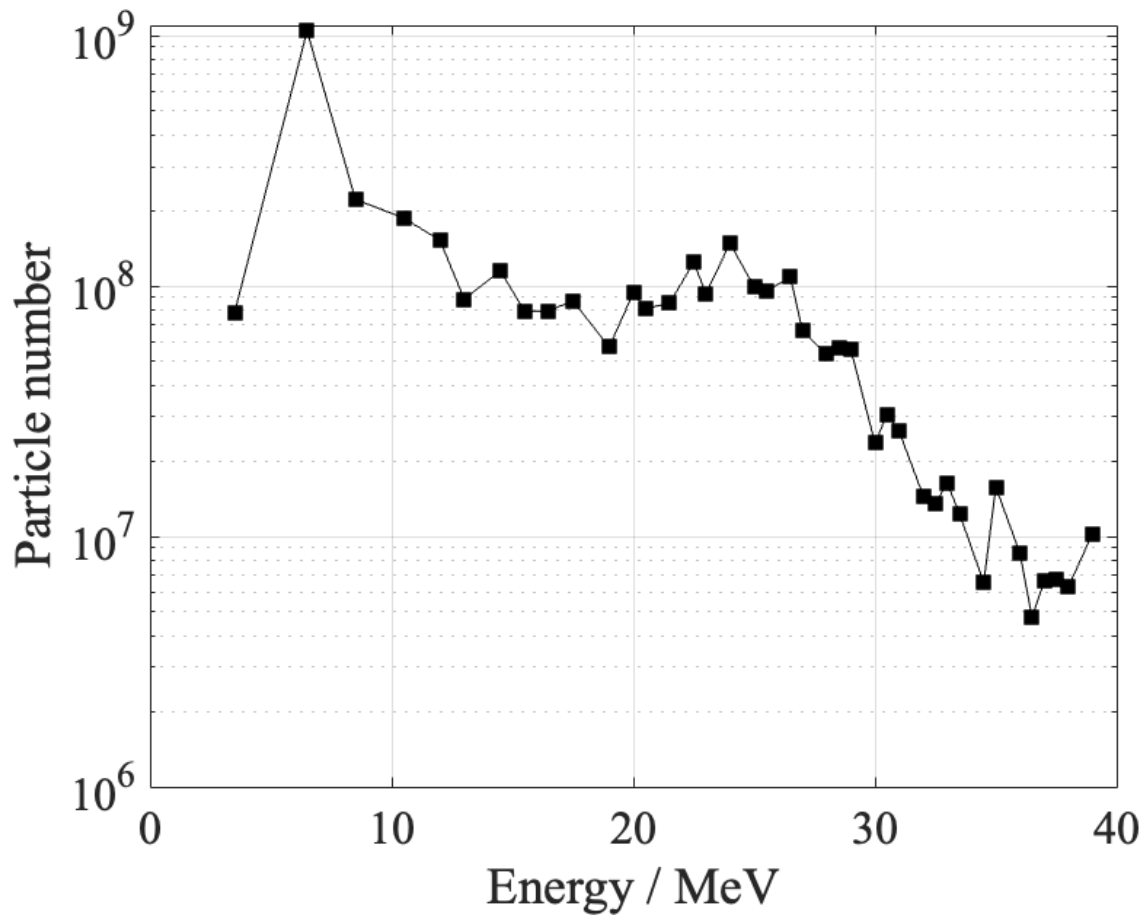


Figure 5.12: Beam spectrum measured upstream of the sample location using a stack of EBT3 RCF.

the beam at each of the RCFs was estimated by inputting the energy spectrum shown in Fig. 5.12 into the in-air portion of MC code. The film detection efficiency for each RCF was estimated to be $\eta = 0.767, 0.754, 0.804$ for RCFs A, B, and C respectively. To obtain the actual dose delivered to the sample, D_S , the doses measured by RCFs A and C for each sample, D_A and D_C , were scaled by the ratio of the doses measured by RCFs A and C, D_{A^*} and D_{C^*} , to the dose measured by the *in situ* RCF-B, D_{B^*} for each day:

$$D_S = \frac{1}{2} \left(D_A \frac{D_{B^*}}{D_{A^*}} + D_C \frac{D_{B^*}}{D_{C^*}} \right). \quad (5.4)$$

After the initial guidance provided by online charge measurements, this RCF analysis routine allowed us to determine the absolute dose delivered to each sample.

To ensure longitudinal dose uniformity along the depth of the thicker samples, there is a need to balance the energy spectrum so as to maximize the total charge delivered while applying an energy spectrum well away from the Bragg peak. The energy spectrum of the beam at the source is Maxwellian so the vast majority of the charge is of low energy (< 10 MeV) and collecting only a small fraction ($< 1\%$) of this part of the spectrum is enough to outweigh the energy deposited on the sample by the higher energy particles.

The energy spectrum of the beam delivered to the *in vitro* samples was measured using a stack of calibrated RCF (Gafchromic, EBT3) and is shown in Fig. 5.12. The process of unfolding the beam spectrum from the stacks is outlined in [68, 66].

There is an unexpected peak in the spectrum at ~ 7 MeV that was not present in the simulations of the beamline at that point. This is likely due to the transfer map representation of the beam dynamics being centered around a reference particle energy, $E_0 = 30$ MeV, far away from this portion of the spectrum. Protons with energies near this peak would be

close to their Bragg peak at the sample location and would thus dominate the dose deposited. While this complicated the dosimetry, the RCFs placed before and after the sample during irradiation allowed for us to see the impact of the spectrum on the dose profile. Future work on the beamline design and the simulations will address this difference between measured and simulated spectrum at the sample.

5.5 Biological results

With this work, we have established a platform that allows us to conduct ultra-high dose rate radiation damage tests to *in vivo* samples that can be compared to other irradiation modalities. The beam transports were used successfully to irradiate over 100 *in vivo* samples across the two campaigns.

For the 2023 campaign, the total dose, sample to sample variations (SSV), and dose error (Δ dose) are displayed for each sample group in Tab. 5.1. Thanks to our adaptive irradiation protocol guided by online dosimetry, the SSV could be reduced to 5%, significantly lower than the 17% SSV in our previous study [Bin]. The relative uncertainty on the total dose estimate over all samples and dose groups is 12 %, including sources of uncertainty like the SSV, the lateral dose variation, fluctuations in the proton source spectrum, uncertainties from the ICT and RCF calibrations [66].

The total dose and sample to sample variations (SSV) for the 2024 campaign are shown in Tab. 5.2. The applied doses ranged from approximately 30 to 70 Gy, with a sample-to-sample dose variation of ~ 10 % (standard deviation) within each day of the campaign. This variation partly results from changes in the proton spectrum over the course of a day, affecting the charge-to-dose calibration of the online dosimetry. Improving the stability of

Group	Sample size	Dose / Gy	SSV / %	ΔD / Gy
A (1 f)	7	50.6	2	5.4
B (1 f)	10	36	4	4.1
C (2 f)	7	42.1	9	5.7
D (4 f)	9	39.6	5	4.5

Table 5.1: Table of dosimetry results from the 2023 experiment for each mouse group. The groups A and B received the total dose in one fraction but are separated by the day of irradiation. Groups C and D were irradiated with fractions of the total dose over 2 and 4 subsequent days.

Group	Sample size	Dose / Gy	SSV / %	Δ Dose/ Gy
1	16	27.0	7	
2	16	57.5	11	
3	16	48.8	7	
4	19	40.1	3	

Table 5.2: Table of dosimetry results from the 2024 experiment for each mouse group separated by date of irradiation.

the proton spectrum is the subject of ongoing work and the details will be discussed in a future publication.

With this platform established, we investigated the radiation damage induced by LD protons on healthy tissues. Normal tissue damage of LD protons was assessed by measuring acute skin damage and late radiation-induced fibrosis in murine ears after high dose radiation exposure. To quantify the amount of damage to healthy tissue, the ear thickness was measured for 35 days after radiation exposure and compared to a sham cohort in the same period that was not irradiated. We also irradiated a cohort of mice each with 36 Gy and 40 Gy (acute) with conventional dose rate 300 kVp x-rays at an XRAD and conducted the same ear thickness measurements post irradiation. Preliminary results are of the 2023 experimental campaign are shown in Fig. 5.13 and will be further addressed in a future publication. The results of the 2024 campaign are still being analyzed.

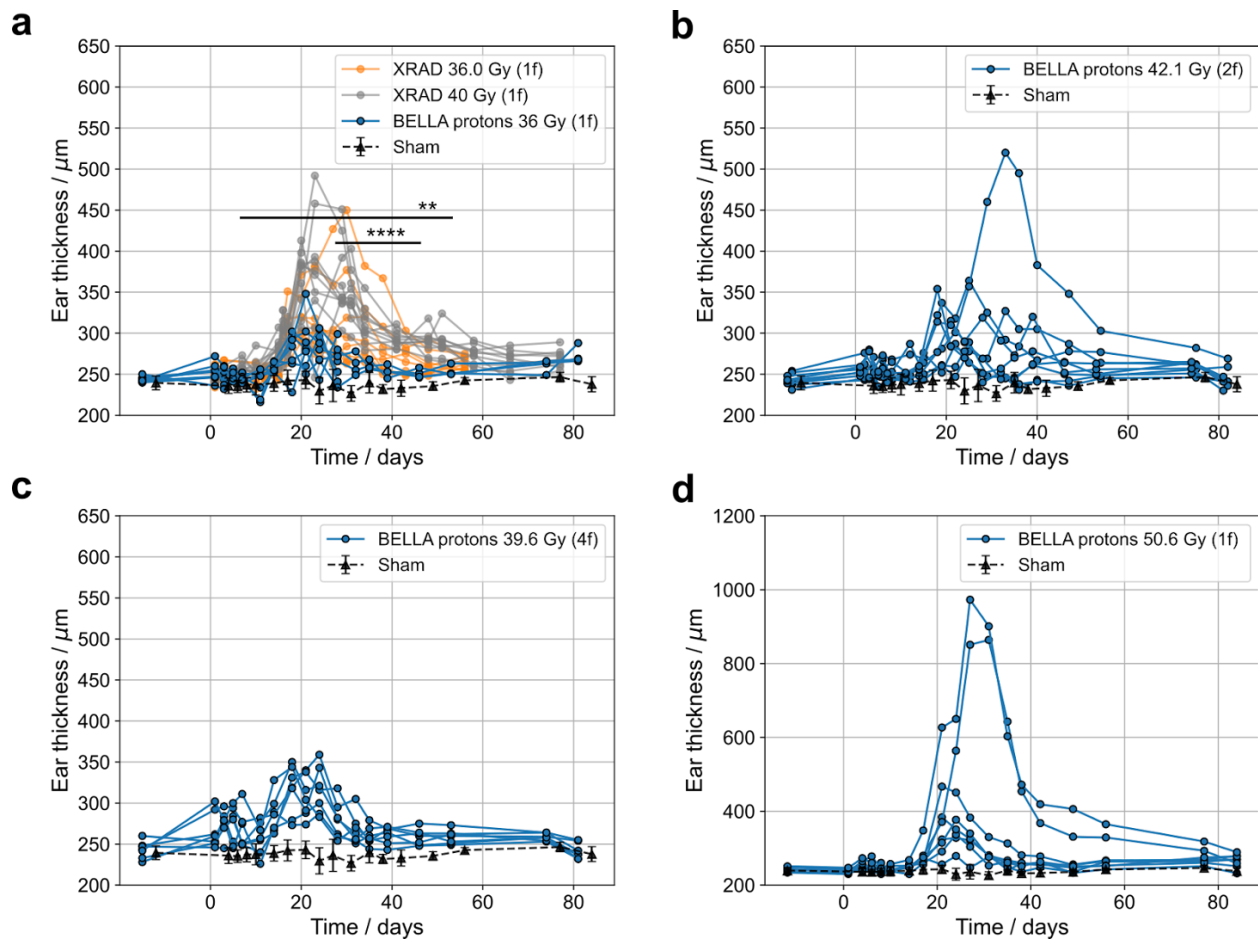


Figure 5.13: Development of ear thickness over time post irradiation. a) Mice ears irradiated with 36.0 Gy of BELLA protons within the same day (blue), 36 Gy of XRAD x-rays (orange), and 40 Gy of XRAD x-rays (grey). b) Mice ears irradiated with a total dose of 42.1 Gy of BELLA protons over two subsequent days, c) 39.6 Gy over four subsequent days, and d) 50.6 Gy within the same day. Black triangles indicate the ear thickness of the sham (control) cohort over the same time period.

5.6 Discussion

The implementation of the beam transport configurations at the BELLA Center's iP2 beamline represents a significant advancement in the practicality of utilizing laser-driven ion accelerators (LDIAs) for radiobiological research. By employing compact, permanent magnet-based beam transport configurations, we were able to deliver 10 or 30 MeV protons with high intensity and precision to biological samples. The inclusion of a comprehensive suite of diagnostics ensured accurate dose measurements and the ability to account for shot-to-shot variability inherent to LDIA. Future research directions will focus on further refining the beam transport and dosimetry systems to enhance their efficiency and accuracy.

The BELLA Center has demonstrated its capacity to accommodate further experiments in the radiobiological domain, particularly those exploring the ultra-high dose rate effects, such as the FLASH effect. This work underscores the Center's role as a hub for cutting-edge research in this field, offering a platform that can be utilized by researchers across different disciplines to explore the various applications of LDIA.

Chapter 6. Conclusion

This dissertation has presented an interdisciplinary investigation into the use of laser-driven ion accelerators (LDIAs) for the controlled delivery of radiation in ultra-high dose rate radiobiology. The work aimed to establish new capabilities for investigating the FLASH effect and provide enabling technologies and methodologies that address key challenges in beam transport, dosimetry, and biological experimentation.

Through the design and modeling of compact, permanent magnet-based beam transport systems, this work has demonstrated that laser-driven proton beams can be effectively collected, collimated, and delivered to biological targets with high intensity and spatial uniformity. These systems overcome the inherent limitations of LDIA sources—namely large divergence and broad energy spectra—by employing tailored magnetic optics configurations, including doublet, triplet, quartet, and mirrored arrangements. Each design was evaluated in terms of collection efficiency, energy spread, spatial symmetry, and dose delivery performance using high-order particle tracking and Monte Carlo radiation transport simulations.

At the Lawrence Berkeley National Laboratory's BELLA iP2 beamline, the beamline designs developed in this work were experimentally realized. Two distinct collimation configurations were implemented to deliver 10 and 30 MeV proton beams to *in vivo* and *in vitro* biological samples. This work marked a significant milestone with the successful irradiation of mouse ear tissue and peptide samples using LDIA proton beams at ultra-high instantaneous dose rates. The transport systems enabled precise, repeatable dose delivery across multiple campaigns, supported by robust dosimetry diagnostics. These diagnostics, validated by simulations, allowed for real-time monitoring and post-exposure verification of

dose, ensuring the integrity of the biological results.

Furthermore, this work contributed to the development of exposure environments across multiple modalities—including synchrotron X-rays and X-ray tube sources—in support of molecular-level investigations of radiation-induced damage. The systematic characterization of these environments enabled experiments on radiolytic peptide modifications and long-term tissue responses.

The results of this thesis support the viability of laser-driven ion beams as a tool for radiobiology research. The beam delivery platforms and diagnostic frameworks presented here offer new opportunities for studying the FLASH effect under controlled conditions and represent a foundational step toward more compact, accessible radiotherapy technologies. Importantly, the implementation of LDIA-based radiobiology platforms at BELLA iP2 establishes a model for future experimental campaigns, not only at LBNL but potentially at other emerging LDIA facilities worldwide.

BIBLIOGRAPHY

- [1] A. C. Begg, F. A. Stewart, and C. Vens, “Strategies to improve radiotherapy with targeted drugs,” *Nat. Rev. Cancer*, vol. 11, pp. 239–253, 4 2011.
- [2] G. Delaney, S. Jacob, C. Featherstone, and M. Barton, “The role of radiotherapy in cancer treatment: Estimating optimal utilization from a review of evidence-based clinical guidelines,” *Cancer*, vol. 104, pp. 1129–1137, 9 2005.
- [3] E. A. Blakely, “The 20th Gray lecture 2019: Health and heavy ions,” *Br. J. Radiol.*, vol. 93, p. 20200172, 11 2020.
- [4] K. Koka, A. Verma, B. S. Dwarakanath, and R. V. Papineni, “Technological Advancements in External Beam Radiation Therapy (EBRT): An Indispensable Tool for Cancer Treatment,” *Cancer Management and Research*, vol. 14, p. 1421, 2022.
- [5] R. Schulte, C. Johnstone, S. Boucher, E. Esarey, C. G. R. Geddes, M. Kravchenko, S. Kutsaev, B. W. Loo, F. Méot, B. Mustapha, K. Nakamura, E. A. Nanni, L. Obst-Huebl, S. E. Sampayan, C. B. Schroeder, K. Sheng, A. M. Snijders, E. Snively, S. G. Tantawi, and J. Van Tilborg, “Transformative Technology for FLASH Radiation Therapy,” *Applied Sciences*, vol. 13, p. 5021, 4 2023.
- [6] A. Macchi, M. Borghesi, and M. Passoni, “Ion acceleration by superintense laser-plasma interaction,” *Rev. Mod. Phys.*, vol. 85, pp. 751–793, 5 2013.
- [7] H. Daido, M. Nishiuchi, and A. S. Pirozhkov, “Review of laser-driven ion sources and their applications,” *Reports on Progress in Physics*, vol. 75, no. 5, p. 56401, 2012.
- [8] S. V. Bulanov and V. S. Khoroshkov, “Feasibility of using laser ion accelerators in proton therapy,” *Plasma Phys. Rep.*, vol. 28, no. 5, pp. 453–456, 2002.
- [9] C.-M. C. Ma, I. Veltchev, E. Fourkal, J. Li, W. Luo, J. Fan, T. Lin, and A. Pollack, “Development of a laser-driven proton accelerator for cancer therapy,” *Laser Physics*, vol. 16, pp. 639–646, 1 2006.
- [10] V. Malka, S. Fritzler, E. Lefebvre, E. D’Humières, R. Ferrand, G. Grillon, C. Albaret, S. Meyroneinc, J. P. Chambaret, A. Antonetti, and D. Hulin, “Practicability of protontherapy using compact laser systems,” *Med. Phys.*, vol. 31, no. 6, pp. 1587–1592, 2004.
- [11] T. Tajima, D. Habs, and X. Yan, “Laser acceleration of ions for radiation therapy,” *Rev. Accel. Sci. Technol.*, vol. 02, pp. 201–228, 1 2009.
- [12] W. Redjem, A. J. Amsellem, F. I. Allen, G. Benndorf, J. Bin, S. Bulanov, E. Esarey, L. C. Feldman, J. Ferrer Fernandez, J. Garcia Lopez, L. Geulig, C. R. Geddes, H. Hi-

- jazi, Q. Ji, V. Ivanov, B. Kanté, A. Gonsalves, J. Meijer, K. Nakamura, A. Persaud, I. Pong, L. Obst-Huebl, P. A. Seidl, J. Simoni, C. Schroeder, S. Steinke, L. Z. Tan, R. Wunderlich, B. Wynne, and T. Schenkel, “Defect engineering of silicon with ion pulses from laser acceleration,” *Communications Materials* 2023 4:1, vol. 4, pp. 1–10, 3 2023.
- [13] P. K. Patel, A. J. Mackinnon, M. H. Key, T. E. Cowan, M. E. Foord, M. Allen, D. F. Price, H. Ruhl, P. T. Springer, and R. Stephens, “Isochoric Heating of Solid-Density Matter with an Ultrafast Proton Beam,” *Phys. Rev. Lett.*, vol. 91, p. 125004, 9 2003.
- [14] P. Antici, J. Fuchs, S. Atzeni, A. Benuzzi, E. Brambrink, M. Esposito, M. Koenig, A. Ravasio, J. Schreiber, A. Schiavi, and P. Audebert, “Isochoric heating of matter by laser-accelerated high-energy protons,” *Journal De Physique IV*, vol. 133, pp. 1077–1079, 1 2006.
- [15] S. Malko, W. Cayzac, V. Ospina-Bohórquez, K. Bhutwala, M. Bailly-Grandvaux, C. McGuffey, R. Fedosejevs, X. Vaisseau, A. Tauschwitz, J. I. Apiñaniz, D. De Luis Blanco, G. Gatti, M. Huault, J. A. Hernandez, S. X. Hu, A. J. White, L. A. Collins, K. Nichols, P. Neumayer, G. Faussurier, J. Vorberger, G. Prestopino, C. Verona, J. J. Santos, D. Batani, F. N. Beg, L. Roso, and L. Volpe, “Proton stopping measurements at low velocity in warm dense carbon,” *Nature Communications* 2022 13:1, vol. 13, pp. 1–12, 5 2022.
- [16] V. Favaudon, L. Caplier, V. Monceau, F. Pouzoulet, M. Sayarath, C. Fouillade, M. F. Poupon, I. Brito, P. Hupé, J. Bourhis, J. Hall, J. J. Fontaine, and M. C. Vozenin, “Ultrahigh dose-rate FLASH irradiation increases the differential response between normal and tumor tissue in mice,” *Sci. Transl. Med.*, vol. 6, 7 2014.
- [17] M. C. Vozenin, P. De Fornel, K. Petersson, V. Favaudon, M. Jaccard, J. F. Germond, B. Petit, M. Burki, G. Ferrand, D. Patin, H. Bouchaab, M. Ozsahin, F. Bochud, C. Bailat, P. Devauchelle, and J. Bourhis, “The advantage of FLASH radiotherapy confirmed in mini-pig and cat-cancer patients,” *Clin. Cancer Res.*, vol. 25, pp. 35–42, 1 2019.
- [18] M. C. Vozenin, B. W. Loo, S. Tantawi, P. G. Maxim, D. R. Spitz, C. Bailat, and C. L. Limoli, “FLASH: New intersection of physics, chemistry, biology, and cancer medicine,” *Reviews of Modern Physics*, vol. 96, 7 2024.
- [19] “The ultra-fast cancer treatments which could replace conventional radiotherapy.”
- [20] K. Nakamura, H. Mao, A. J. Gonsalves, H. Vincenti, D. E. Mittelberger, J. Daniels, A. Magana, C. Toth, and W. P. Leemans, “Diagnostics, Control and Performance Parameters for the BELLA High Repetition Rate Petawatt Class Laser,” *IEEE Journal of Quantum Electronics*, vol. 53, no. 4, pp. 1–21, 2017.

- [21] W. P. Leemans, A. J. Gonsalves, H. S. Mao, K. Nakamura, C. Benedetti, C. B. Schroeder, C. Tóth, J. Daniels, D. E. Mittelberger, S. S. Bulanov, J. L. Vay, C. G. Geddes, and E. Esarey, “Multi-GeV electron beams from capillary-discharge-guided subpetawatt laser pulses in the self-trapping regime,” *Phys. Rev. Lett.*, vol. 113, 12 2014.
- [22] A. J. Gonsalves, K. Nakamura, J. Daniels, C. Benedetti, C. Pieronek, T. C. De Raadt, S. Steinke, J. H. Bin, S. S. Bulanov, J. Van Tilborg, C. G. Geddes, C. B. Schroeder, C. Tóth, E. Esarey, K. Swanson, L. Fan-Chiang, G. Bagdasarov, N. Bobrova, V. Gasilov, G. Korn, P. Sasorov, and W. P. Leemans, “Petawatt laser guiding and electron beam acceleration to 8 GeV in a laser-heated capillary discharge waveguide,” *Phys. Rev. Lett.*, vol. 122, 2 2019.
- [23] C. Toth, D. Evans, A. J. Gonsalves, M. Kirkpatrick, A. Magana, G. Mannino, H.-S. Mao, K. Nakamura, J. R. Riley, S. Steinke, T. Sipla, D. Syversrud, N. Ybarrolaza, and W. P. Leemans, “Transition of the BELLA PW laser system towards a collaborative research facility in laser plasma science,” *AIP Conference Proceedings*, vol. 1812, no. 1, p. 110005, 2017.
- [24] S. Hakimi, L. Obst-Huebl, A. Huebl, K. Nakamura, S. S. Bulanov, S. Steinke, W. P. Leemans, Z. Kober, T. M. Ostermayr, T. Schenkel, A. J. Gonsalves, J.-L. Vay, J. van Tilborg, C. Toth, C. B. Schroeder, E. Esarey, and C. G. R. Geddes, “Lasersolid interaction studies enabled by the new capabilities of the iP2 BELLA PW beamline,” *Physics of Plasmas*, vol. 29, no. 8, p. 83102, 2022.
- [25] L. Obst-Huebl, K. Nakamura, S. Hakimi, J. T. D. Chant, A. Jewell, B. Stassel, A. M. Snijders, A. J. Gonsalves, J. van Tilborg, Z. Eisentraut, Z. Harvey, L. Willingale, C. Toth, C. B. Schroeder, C. G. R. Geddes, and E. Esarey, “High power commissioning of BELLA iP2 up to 17 J,” *Applying Laser-driven Particle Acceleration III: Using Distinctive Energetic Particle and Photon Sources*, vol. 12583, p. 1258305, 2023.
- [26] J. H. LAWRENCE, C. A. TOBIAS, J. L. BORN, R. K. McCOMBS, J. E. ROBERTS, H. O. ANGER, B. V. LOW-BEER, and C. B. HUGGINS, “Pituitary irradiation with high-energy proton beams: a preliminary report,” *Cancer research*, vol. 18, pp. 121–34, 2 1958.
- [27] S. Gupta, J. L. Inman, J. De Chant, L. Obst-Huebl, K. Nakamura, S. M. Costello, S. Marqusee, J. H. Mao, L. Kunz, R. Paisley, M. C. Vozenin, A. M. Snijders, and C. Y. Ralston, “A Novel Platform for Evaluating Dose Rate Effects on Oxidative Damage to Peptides: Toward a High-Throughput Method to Characterize the Mechanisms Underlying the FLASH Effect,” <https://doi.org/10.1667/RADE-23-00131.1>, vol. 200, pp. 523–530, 11 2023.
- [28] J. L. Inman, Y. Wu, L. Chen, E. Brydon, D. Ghosh, K. H. Wan, J. De Chant, L. Obst-Huebl, K. Nakamura, C. Y. Ralston, S. E. Celniker, J. H. Mao, P. H. Zwart, H. Y. N.

- Holman, H. Chang, J. B. Brown, and A. M. Snijders, “Long-term, non-invasive FTIR detection of low-dose ionizing radiation exposure,” *Scientific Reports* 2024 14:1, vol. 14, pp. 1–12, 3 2024.
- [29] J. Bin, L. Obst-Huebl, J. H. Mao, K. Nakamura, L. D. Geulig, H. Chang, Q. Ji, L. He, J. De Chant, Z. Kober, A. J. Gonsalves, S. Bulanov, S. E. Celniker, C. B. Schroeder, C. G. Geddes, E. Esarey, B. A. Simmons, T. Schenkel, E. A. Blakely, S. Steinke, and A. M. Snijders, “A new platform for ultra-high dose rate radiobiological research using the BELLA PW laser proton beamline,” *Scientific Reports* 2022 12:1, vol. 12, pp. 1–15, 1 2022.
- [30] F. Kroll, F.-E. Brack, C. Bernert, S. Bock, E. Bodenstern, K. Brüchner, T. E. Cowan, L. Gaus, R. Gebhardt, U. Helbig, L. Karsch, T. Kluge, S. Kraft, M. Krause, E. Lessmann, U. Masood, S. Meister, J. Metzkes-Ng, A. Nossula, J. Pawelke, J. Pietzsch, T. Püschel, M. Reimold, M. Rehwald, C. Richter, H.-P. Schlenvoigt, U. Schramm, M. E. P. Umlandt, T. Ziegler, K. Zeil, and E. Beyreuther, “Tumour irradiation in mice with a laser-accelerated proton beam,” *Nature Physics*, vol. 18, no. 3, pp. 316–322, 2022.
- [31] R. A. Snavely, M. H. Key, S. P. Hatchett, I. E. Cowan, M. Roth, T. W. Phillips, M. A. Stoyer, E. A. Henry, T. C. Sangster, M. S. Singh, S. C. Wilks, A. MacKinnon, A. Offenberger, D. M. Pennington, K. Yasuike, A. B. Langdon, B. F. Lasinski, J. Johnson, M. D. Perry, and E. M. Campbell, “Intense High-Energy Proton Beams from Petawatt-Laser Irradiation of Solids,” *Physical Review Letters*, vol. 85, p. 2945, 10 2000.
- [32] P. Mora, “Plasma Expansion into a Vacuum,” *Physical Review Letters*, vol. 90, p. 4, 5 2003.
- [33] M. Passoni and M. Lontano, “Theory of light-ion acceleration driven by a strong charge separation,” *Physical Review Letters*, vol. 101, 9 2008.
- [34] M. Borghesi, J. Fuchs, S. V. Bulanov, A. J. Mackinnon, P. K. Patel, and M. Roth, “Fast Ion Generation by High-Intensity Laser Irradiation of Solid Targets and Applications,” *Fusion Science and Technology*, vol. 49, no. 3, pp. 412–439, 2006.
- [35] P. Sommer, J. Metzkes-Ng, F. E. Brack, T. E. Cowan, S. D. Kraft, L. Obst, M. Rehwald, H. P. Schlenvoigt, U. Schramm, and K. Zeil, “Laser-ablation-based ion source characterization and manipulation for laser-driven ion acceleration,” *Plasma Physics and Controlled Fusion*, vol. 60, p. 054002, 3 2018.
- [36] J. Fuchs, T. E. Cowan, P. Audebert, H. Ruhl, L. Gremillet, A. Kemp, M. Allen, A. Blazevic, J. C. Gauthier, M. Geissel, M. Hegelich, S. Karsch, P. Parks, M. Roth, Y. Sentoku, R. Stephens, and E. M. Campbell, “Spatial uniformity of laser-accelerated

- ultrahigh-current mev electron propagation in metals and insulators,” *Physical Review Letters*, vol. 91, p. 255002, 12 2003.
- [37] T. E. Cowan, J. Fuchs, H. Ruhl, A. Kemp, P. Audebert, M. Roth, R. Stephens, I. Barton, A. Blazevic, E. Brambrink, J. Cobble, J. Fernández, J. C. Gauthier, M. Geissel, M. Hegelich, J. Kaae, S. Karsch, G. P. Le Sage, S. Letzring, M. Manclossi, S. Meyeroneinc, A. Newkirk, H. Pépin, and N. Renard-LeGalloudec, “Ultralow emittance, multi-MeV proton beams from a laser virtual-cathode plasma accelerator,” *Physical Review Letters*, vol. 92, p. 204801, 5 2004.
- [38] A. V. Kuznetsov, T. Z. Esirkepov, F. F. Kamenets, and S. V. Bulanov, “Efficiency of ion acceleration by a relativistically strong laser pulse in an underdense plasma,” *Plasma Physics Reports*, vol. 27, pp. 211–220, 3 2001.
- [39] J. Park, S. S. Bulanov, J. Bin, Q. Ji, S. Steinke, J. L. Vay, C. G. Geddes, C. B. Schroeder, W. P. Leemans, T. Schenkel, and E. Esarey, “Ion acceleration in laser generated megatesla magnetic vortex,” *Physics of Plasmas*, vol. 26, 10 2019.
- [40] T. Esirkepov, M. Borghesi, S. V. Bulanov, G. Mourou, and T. Tajima, “Highly efficient relativistic-ion generation in the laser-piston regime,” *Physical Review Letters*, vol. 92, 4 2004.
- [41] S. S. Bulanov, E. Esarey, C. B. Schroeder, S. V. Bulanov, T. Z. Esirkepov, M. Kando, F. Pegoraro, and W. P. Leemans, “Radiation pressure acceleration: The factors limiting maximum attainable ion energy,” *Physics of Plasmas*, vol. 23, 5 2016.
- [42] M. Berz, K. Makino, and W. Wan, *An introduction to beam physics*. CRC Press, 1st ed., 12 2014.
- [43] M. Berger, J. Hubbell, J. C. Seltzer, J. Coursey, R. Sukumar, D. Zucker, and K. Olsen, “XCOM: Photon Cross Sections Database — NIST,” *NIST Standard Reference Database 8*, vol. 87, 11 2010.
- [44] H. Bethe, “Zur Theorie des Durchgangs schneller Korpuskularstrahlen durch Materie,” *Annalen der Physik*, vol. 397, pp. 325–400, 1 1930.
- [45] F. Bloch, “Zur Bremsung rasch bewegter Teilchen beim Durchgang durch Materie,” *Annalen der Physik*, vol. 408, pp. 285–320, 1 1933.
- [46] M. Berger, J. Coursey, M. Zucker, and J. Chang, “Stopping-Power & Range Tables for Electrons, Protons, and Helium Ions — NIST,” *NIST Standard Reference Database*, vol. 124, 2017.
- [47] P. Andreo, “Monte Carlo simulations in radiotherapy dosimetry,” *Radiation Oncology*, vol. 13, pp. 1–15, 6 2018.

- [48] S. Agostinelli, J. Allison, K. Amako, J. Apostolakis, H. Araujo, P. Arce, M. Asai, D. Axen, S. Banerjee, G. Barrand, F. Behner, L. Bellagamba, J. Boudreau, L. Broglia, A. Brunengo, H. Burkhardt, S. Chauvie, J. Chuma, R. Chytracsek, G. Cooperman, G. Cosmo, P. Degtyarenko, A. Dell’Acqua, G. Depaola, D. Dietrich, R. Enami, A. Feliciello, C. Ferguson, H. Fesefeldt, G. Folger, F. Foppiano, A. Forti, S. Garelli, S. Giani, R. Giannitrapani, D. Gibin, J. J. Gomez Cadenas, I. Gonzalez, G. Gracia Abril, G. Greeniaus, W. Greiner, V. Grichine, A. Grossheim, S. Guatelli, P. Gumplinger, R. Hamatsu, K. Hashimoto, H. Hasui, A. Heikkinen, A. Howard, V. Ivanchenko, A. Johnson, F. W. Jones, J. Kallenbach, N. Kanaya, M. Kawabata, Y. Kawabata, M. Kawaguti, S. Kelner, P. Kent, A. Kimura, T. Kodama, R. Kokoulin, M. Kossov, H. Kurashige, E. Lamanna, T. Lampen, V. Lara, V. Lefebure, F. Lei, M. Liendl, W. Lockman, F. Longo, S. Magni, M. Maire, E. Medernach, K. Minamimoto, P. Mora de Freitas, Y. Morita, K. Murakami, M. Nagamatu, R. Nartallo, P. Nieminen, T. Nishimura, K. Ohtsubo, M. Okamura, S. O’Neale, Y. Oohata, K. Paech, J. Perl, A. Pfeiffer, M. G. Pia, F. Ranjard, A. Rybin, S. Sadilov, E. di Salvo, G. Santin, T. Sasaki, N. Savvas, Y. Sawada, S. Scherer, S. Sei, V. Sirotenko, D. Smith, N. Starkov, H. Stoecker, J. Sulkimo, M. Takahata, S. Tanaka, E. Tcherniaev, E. Safai Tehrani, M. Tropeano, P. Truscott, H. Uno, L. Urban, P. Urban, M. Verderi, A. Walkden, W. Wander, H. Weber, J. P. Wellisch, T. Wenaus, D. C. Williams, D. Wright, T. Yamada, H. Yoshida, and D. Zschesche, “Geant4a simulation toolkit,” *Nuclear Instruments and Methods in Physics Research Section A: Accelerators, Spectrometers, Detectors and Associated Equipment*, vol. 506, pp. 250–303, 7 2003.
- [49] J. Perl, J. Shin, J. Schümann, B. Faddegon, and H. Paganetti, “TOPAS: An innovative proton Monte Carlo platform for research and clinical applications,” *Med. Phys.*, vol. 39, no. 11, pp. 6818–6837, 2012.
- [50] E. Fourkal, J. S. Li, W. Xiong, A. Nahum, and C. M. Ma, “Intensity modulated radiation therapy using laser-accelerated protons: a Monte Carlo dosimetric study,” *Physics in medicine and biology*, vol. 48, pp. 3977–4000, 12 2003.
- [51] “Radiation Therapy for Cancer - NCI.”
- [52] G. Delaney, S. Jacob, C. Featherstone, and M. Barton, “The role of radiotherapy in cancer treatment,” *Cancer*, vol. 104, pp. 1129–1137, 9 2005.
- [53] W. D. Newhauser and R. Zhang, “The physics of proton therapy,” *Physics in medicine and biology*, vol. 60, p. R155, 4 2015.
- [54] P. Montay-Gruel, K. Petersson, M. Jaccard, G. Boivin, J. F. Germond, B. Petit, R. Doenlen, V. Favaudon, F. Bochud, C. Bailat, J. Bourhis, and M. C. Vozenin, “Irradiation in a flash: Unique sparing of memory in mice after whole brain irradiation with dose rates above 100Gy/s,” *Radiother. Oncol.*, vol. 124, pp. 365–369, 9 2017.

- [55] O. Zlobinskaya, C. Siebenwirth, C. Greubel, V. Hable, R. Hertenberger, N. Humble, S. Reinhardt, D. Michalski, B. Röper, G. Multhoff, G. Dollinger, J. J. Wilkens, and T. E. Schmid, “The effects of ultra-high dose rate proton irradiation on growth delay in the treatment of human tumor xenografts in nude mice,” *Radiat. Res.*, vol. 181, no. 2, pp. 177–183, 2014.
- [56] P. Montay-Gruel, A. Bouchet, M. Jaccard, D. Patin, R. Serduc, W. Aim, K. Peterson, B. Petit, C. Bailat, J. Bourhis, E. Bräuer-Krisch, and M. C. Vozenin, “X-rays can trigger the FLASH effect: Ultra-high dose-rate synchrotron light source prevents normal brain injury after whole brain irradiation in mice,” *Radiotherapy and Oncology*, vol. 129, pp. 582–588, 12 2018.
- [57] R. Abolfath, D. Grosshans, and R. Mohan, “Oxygen depletion in FLASH ultra-high-dose-rate radiotherapy: A molecular dynamics simulation,” *Medical Physics*, vol. 47, pp. 6551–6561, 12 2020.
- [58] R. Labarbe, L. Hotoiu, J. Barbier, and V. Favaudon, “A physicochemical model of reaction kinetics supports peroxy radical recombination as the main determinant of the FLASH effect,” *Radiotherapy and Oncology*, vol. 153, pp. 303–310, 12 2020.
- [59] J. Y. Jin, A. Gu, W. Wang, N. L. Oleinick, M. Machtay, and F. M. (Spring) Kong, “Ultra-high dose rate effect on circulating immune cells: A potential mechanism for FLASH effect?,” *Radiotherapy and Oncology*, vol. 149, pp. 55–62, 8 2020.
- [60] G. Xu and M. R. Chance, “Hydroxyl radical-mediated modification of proteins as probes for structural proteomics,” *Chemical Reviews*, vol. 107, pp. 3514–3543, 8 2007.
- [61] I. J. Das, ed., *Radiochromic Film*. Boca Raton: CRC Press, 1st ed., 10 2017.
- [62] A. Niroomand-Rad, S. T. Chiu-Tsao, M. P. Grams, D. F. Lewis, C. G. Soares, L. J. Van Battum, I. J. Das, S. Trichter, M. W. Kissick, G. Massillon-JL, P. E. Alvarez, and M. F. Chan, “Report of AAPM Task Group 235 Radiochromic Film Dosimetry: An Update to TG-55,” *Medical Physics*, vol. 47, pp. 5986–6025, 12 2020.
- [63] “ALS Machine Information.”
- [64] J. C. Crosbie, R. L. Anderson, K. Rothkamm, C. M. Restall, L. Cann, S. Ruwanpura, S. Meachem, N. Yagi, I. Svalbe, R. A. Lewis, B. R. Williams, and P. A. Rogers, “Tumor Cell Response to Synchrotron Microbeam Radiation Therapy Differs Markedly From Cells in Normal Tissues,” *International Journal of Radiation Oncology*Biological*Physics*, vol. 77, pp. 886–894, 7 2010.
- [65] M. Rosi, B. Russell, L. G. Kristensen, E. R. Farquhar, R. Jain, D. Abel, M. Sullivan, S. M. Costello, M. A. Dominguez-Martin, Y. Chen, S. Marqusee, C. J. Petzold, C. A. Kerfeld, D. P. DePonte, F. Farahmand, S. Gupta, and C. Y. Ralston, “An automated

liquid jet for fluorescence dosimetry and microsecond radiolytic labeling of proteins,” *Communications Biology* 2022 5:1, vol. 5, pp. 1–10, 8 2022.

- [66] J. H. Bin, Q. Ji, P. A. Seidl, D. Raftrey, S. Steinke, A. Persaud, K. Nakamura, A. Goncalves, W. P. Leemans, and T. Schenkel, “Absolute calibration of GafChromic film for very high flux laser driven ion beams,” *Review of Scientific Instruments*, vol. 90, p. 53301, 5 2019.
- [67] S. D. Kraft, C. Richter, K. Zeil, M. Baumann, E. Beyreuther, S. Bock, M. Bussmann, T. E. Cowan, Y. Dammene, W. Enghardt, U. Heibig, L. Karsch, T. Kluge, L. Laschinsky, E. Lessmann, J. Metzkes, D. Naumburger, R. Sauerbrey, M. Schürer, M. Sobiella, J. Woithe, U. Schramm, and J. Pawelke, “Dose-dependent biological damage of tumour cells by laser-accelerated proton beams,” *New J. Phys.*, vol. 12, 8 2010.
- [68] M. Schollmeier, M. Geissel, A. B. Sefkow, and K. A. Flippo, “Improved spectral data unfolding for radiochromic film imaging spectroscopy of laser-accelerated proton beams,” *Rev. Sci. Instrum.*, vol. 85, no. 4, p. 043305, 2014.
- [69] T. Burris-Mog, K. Michel, F. Nürnberg, S. Busold, M. Bussmann, O. Deppert, G. Hoffmeister, M. Joost, M. Sobiella, Tauschwitz, B. Zielbauer, V. Bagnoud, T. Herrmannsdoerfer, M. Roth, and T. Cowan, “Laser accelerated protons captured and transported by a pulse power solenoid,” *Phys. Rev. ST Accel. Beams*, vol. 14, pp. 7–13, 1 2011.
- [70] D. Jahn, D. Schumacher, C. Brabetz, J. Ding, S. Weih, F. Kroll, F. E. Brack, U. Schramm, A. Blažević, and M. Roth, “First application studies at the laser-driven LIGHT beamline: Improving proton beam homogeneity and imaging of a solid target,” *Nucl. Instrum. Meth. A*, vol. 909, pp. 173 – 176, 2018.
- [71] F. E. Brack, F. Kroll, L. Gaus, C. Bernert, E. Beyreuther, T. E. Cowan, L. Karsch, S. Kraft, L. A. Kunz-Schughart, E. Lessmann, J. Metzkes-Ng, L. Obst-Huebl, J. Pawelke, M. Rehwald, H. P. Schlenvoigt, U. Schramm, M. Sobiella, E. R. Szabó, T. Ziegler, and K. Zeil, “Spectral and spatial shaping of laser-driven proton beams using a pulsed high-field magnet beamline,” *Sci. Rep.*, vol. 10, p. 9118, 12 2020.
- [72] J. K. Lim, P. Frigola, G. Travish, J. B. Rosenzweig, S. G. Anderson, W. J. Brown, J. S. Jacob, C. L. Robbins, and A. M. Tremaine, “Adjustable, short focal length permanent-magnet quadrupole based electron beam final focus system,” *Phys. Rev. ST Accel. Beams*, vol. 8, p. 72401, 7 2005.
- [73] T. Eichner, F. Grüner, S. Becker, M. Fuchs, D. Habs, R. Weingartner, U. Schramm, H. Backe, P. Kunz, and W. Lauth, “Miniature magnetic devices for laser-based, tabletop free-electron lasers,” *Phys. Rev. ST Accel. Beams*, vol. 10, p. 82401, 8 2007.

- [74] S. Ter-Avetisyan, M. Schnürer, R. Polster, P. V. Nickles, and W. Sandner, “First demonstration of collimation and monochromatisation of a laser accelerated proton burst,” *Laser and Particle Beams*, vol. 26, no. 4, pp. 637–642, 2008.
- [75] M. Schollmeier, S. Becker, M. Geissel, K. Flippo, A. Blazevic, S. Gaillard, D. Gautier, F. Grüner, K. Michel, M. Kimmel, F. Nürnberg, P. Rambo, U. Schramm, J. Schreiber, J. Schüttrumpf, J. Schwarz, N. Tahir, B. Atherton, D. Habs, and M. Roth, “Controlled Transport and Focusing of Laser-Accelerated Protons with Miniature Magnetic Devices,” *Phys. Rev. Lett.*, vol. 101, p. 55004, 1 2008.
- [76] M. Nishiuchi, I. Daito, M. Ikegami, H. Daido, M. Mori, S. Orimo, K. Ogura, A. Sagisaka, A. Yogo, A. S. Pirozhkov, H. Sugiyama, H. Kiriya, H. Okada, S. Kanazawa, S. Kondo, T. Shimomura, M. Tanoue, Y. Nakai, H. Sasao, D. Wakai, H. Sakaki, P. Bolton, I. W. Choi, J. H. Sung, J. Lee, Y. Oishi, T. Fujii, K. Nemoto, H. Souda, A. Noda, Y. Iseki, and T. Yoshiyuki, “Focusing and spectral enhancement of a repetition-rated, laser-driven, divergent multi-MeV proton beam using permanent quadrupole magnets,” *Applied Physics Letters*, vol. 94, no. 6, p. 61107, 2009.
- [77] T. F. Rösch, Z. Szabó, D. Haffa, J. Bin, S. Brunner, F. S. Englbrecht, A. A. Friedl, Y. Gao, J. Hartmann, P. Hilz, C. Kreuzer, F. H. Lindner, T. M. Ostermayr, R. Polanek, M. Speicher, E. R. Szabó, D. Taray, T. Tóké, M. Würzl, K. Parodi, K. Hideghéty, and J. Schreiber, “A feasibility study of zebrafish embryo irradiation with laser-accelerated protons,” *Rev. Sci. Instrum.*, vol. 91, no. 6, p. 63303, 2020.
- [78] W. K. H. Panofsky and W. R. Baker, “A Focusing Device for the External 350Mev Proton Beam of the 184Inch Cyclotron at Berkeley,” *Rev. Sci. Instrum.*, vol. 21, no. 5, pp. 445–447, 1950.
- [79] J. van Tilborg, S. Steinke, C. G. R. Geddes, N. H. Matlis, B. H. Shaw, A. J. Gonsalves, J. V. Huijts, K. Nakamura, J. Daniels, C. B. Schroeder, C. Benedetti, E. Esarey, S. S. Bulanov, N. A. Bobrova, P. V. Sasorov, and W. P. Leemans, “Active Plasma Lensing for Relativistic Laser-Plasma-Accelerated Electron Beams,” *Phys. Rev. Lett.*, vol. 115, p. 184802, 10 2015.
- [80] C. A. Lindström, E. Adli, G. Boyle, R. Corsini, A. E. Dyson, W. Farabolini, S. M. Hooker, M. Meisel, J. Osterhoff, J.-H. Röckemann, L. Schaper, and K. N. Sjobak, “Emittance Preservation in an Aberration-Free Active Plasma Lens,” *Phys. Rev. Lett.*, vol. 121, p. 194801, 11 2018.
- [81] W. Wan, L. Brouwer, S. Caspi, S. Prestemon, A. Gerbershagen, J. M. Schippers, and D. Robin, “Alternating-gradient canted cosine theta superconducting magnets for future compact proton gantries,” *Phys. Rev. ST Accel. Beams*, vol. 18, p. 103501, 10 2015.

- [82] X. Zhang, K. Wang, K. Wang, Y. Li, J. Li, X. Yang, F. Wu, X. Yan, and K. Zhu, “Development of the superconducting solenoid for the compact laser plasma accelerator for proton therapy,” *Physica C: Superconductivity and its Applications*, vol. 632, p. 1354702, 5 2025.
- [83] F. Romano, F. Schillaci, G. A. P. Cirrone, G. Cuttone, V. Scuderi, L. Allegra, A. Amato, A. Amico, G. Candiano, G. De Luca, G. Gallo, S. Giordanengo, L. F. Guarachi, G. Korn, G. Larosa, R. Leanza, R. Manna, V. Marchese, F. Marchetto, D. Margarone, G. Milluzzo, G. Petringa, J. Pipek, S. Pulvirenti, D. Rizzo, R. Sacchi, S. Salamone, M. Sedita, and A. Vignati, “The ELIMED transport and dosimetry beamline for laser-driven ion beams,” *Nucl. Instrum. Meth. A*, vol. 829, pp. 153–158, 2016.
- [84] K. Halbach, “Design of permanent multipole magnets with oriented rare earth cobalt material,” *Nucl. Instrum. Meth.*, vol. 169, no. 1, pp. 1–10, 1980.
- [85] O. Chubar, P. Elleaume, and J. Chavanne, “A three-dimensional magnetostatics computer code for insertion devices,” *Journal of Synchrotron Radiation*, vol. 5, pp. 481–484, 5 1998.
- [86] K. Makino and M. Berz, “COSY INFINITY Version 9,” *Nucl. Instrum. Meth.*, vol. A558, pp. 346–350, 2005.
- [87] V. N. Aseev, P. N. Ostroumov, E. S. Lessner, and B. Mustapha, “Track: The New Beam Dynamics Code,” in *Proc. of the 2005 Particle Accelerator Conf.*, pp. 2053–2055, 2005.
- [88] J. Qiang and R. Ryne, “IMPACT: Integrated Map and Particle ACcelerator Tracking Code.”
- [89] K. B. Thomas J. Roberts, “G4BEAMLINE SIMULATIONS FOR DETECTOR DEVELOPMENT,” in *Proc. of EPAC08, Genoa, Italy*, pp. 1506–1507, 2008.
- [90] L. J. Nevay, S. T. Boogert, J. Snuverink, A. Abramov, L. C. Deacon, H. Garcia-Morales, H. Lefebvre, S. M. Gibson, R. Kwee-Hinzmann, W. Shields, and S. D. Walker, “BDSIM: An accelerator tracking code with particlematter interactions,” *Computer Physics Communications*, vol. 252, p. 107200, 2020.
- [91] “MADX.”
- [92] K. L. Brown, F. Rothacker, D. C. Carey, and F. C. Iselin, “TRANSPORT,” Tech. Rep. CERN-80-04, NAL-91, FERMILAB-NAL-091, UC-28, SLAC, 1983.
- [93] K. R. Crandall, “TRACE 3-D,” Tech. Rep. LA11054-MS, LANL, 1987.

- [94] R. L. Workman, V. D. Burkert, V. Crede, E. Klempt, U. Thoma, L. Tiator, K. Agashe, G. Aielli, B. C. Allanach, C. AMSler, M. Antonelli, E. C. Aschenauer, D. M. Asner, H. Baer, S. W. Banerjee, R. M. Barnett, L. Baudis, C. W. Bauer, J. J. Beatty, V. I. Belousov, J. Beringer, A. Bettini, O. Biebel, K. M. Black, E. Blucher, R. Bonventre, V. V. Bryzgalov, O. Buchmuller, M. A. Bychkov, R. N. Cahn, M. Carena, A. Ceccucci, A. Cerri, R. S. Chivukula, G. Cowan, K. Cranmer, O. Cremonesi, G. D’Ambrosio, T. Damour, D. De Florian, A. De Gouvêa, T. DeGrand, P. De Jong, S. Demers, B. A. Dobrescu, M. D’Onofrio, M. Doser, H. K. Dreiner, P. Eerola, U. Egede, S. Eidelman, A. X. El-Khadra, J. Ellis, S. C. Eno, J. Erler, V. V. Ezhela, W. Fetscher, B. D. Fields, A. Freitas, H. Gallagher, Y. Gershtein, T. Gherghetta, M. C. Gonzalez-Garcia, M. Goodman, C. Grab, A. V. Gritsan, C. Grojean, D. E. Groom, M. Grünewald, A. Gurtu, T. Gutsche, H. E. Haber, M. Hamel, C. Hanhart, S. Hashimoto, Y. Hayato, A. Hebecker, S. Heinemeyer, J. J. Hernández-Rey, K. Hikasa, J. Hisano, A. Höcker, J. Holder, L. Hsu, J. Huston, T. Hyodo, A. Ianni, M. Kado, M. Karliner, U. F. Katz, M. Kenzie, V. A. Khoze, S. R. Klein, F. Krauss, M. Kreps, P. Križan, B. Krusche, Y. Kwon, O. Lahav, J. Laiho, L. P. Lellouch, J. Lesgourgues, A. R. Liddle, Z. Ligeti, C. J. Lin, C. Lippmann, T. M. Liss, L. Littenberg, C. Lourenço, K. S. Lugovsky, S. B. Lugovsky, A. Lusiani, Y. Makida, F. Maltoni, T. Mannel, A. V. Manohar, W. J. Marciano, A. Masoni, J. Matthews, U. G. Meißner, I. A. Melzer-Pellmann, M. Mikhasenko, D. J. Miller, D. Milstead, R. E. Mitchell, K. Mönig, P. Molaro, F. Moortgat, M. Moskvic, K. Nakamura, M. Narain, P. Nason, S. Navas, A. Nelles, M. Neubert, P. Nevski, Y. Nir, K. A. Olive, C. Patrignani, J. A. Peacock, V. A. Petrov, E. Pianori, A. Pich, A. Piepke, F. Pietropaolo, A. Pomarol, S. Pordes, S. Profumo, A. Quadt, K. Rabbertz, J. Rademacker, G. Raffelt, M. Ramsey-Musolf, B. N. Ratcliff, P. Richardson, A. Ringwald, D. J. Robinson, S. Roesler, S. Rolli, A. Romaniouk, L. J. Rosenberg, J. L. Rosner, G. Rybka, M. G. Ryskin, R. A. Ryutin, Y. Sakai, S. Sarkar, F. Sauli, O. Schneider, S. Schönert, K. Scholberg, A. J. Schwartz, J. Schwiening, D. Scott, F. Sefkow, U. Seljak, V. Sharma, S. R. Sharpe, V. Shiltsev, G. Signorelli, M. Silari, F. Simon, T. Sjöstrand, P. Skands, T. Skwarnicki, G. F. Smoot, A. Soffer, M. S. Sozzi, S. Spanier, C. Spiering, A. Stahl, S. L. Stone, Y. Sumino, M. J. Syphers, F. Takahashi, M. Tanabashi, J. Tanaka, M. Taševský, K. Terao, K. Terashi, J. Terning, R. S. Thorne, M. Titov, N. P. Tkachenko, D. R. Tovey, K. Trabelsi, P. Urquijo, G. Valencia, R. V. Van De Water, N. Varelas, G. Venanzoni, L. Verde, I. Vivarelli, P. Vogel, W. Vogelsang, V. Vorobyev, S. P. Wakely, W. Walkowiak, C. W. Walter, D. Wands, D. H. Weinberg, E. J. Weinberg, N. Vermes, M. White, L. R. Wiencke, S. Willocq, C. G. Wohl, C. L. Woody, W. M. Yao, M. Yokoyama, R. Yoshida, G. Zanderighi, G. P. Zeller, O. V. Zenin, R. Y. Zhu, S. L. Zhu, F. Zimmermann, P. A. Zyla, J. Anderson, T. Basaglia, P. Schaffner, and W. Zheng, “Review of Particle Physics,” *Progress of Theoretical and Experimental Physics*, vol. 2022, 8 2022.
- [95] J. H. Bin, W. J. Ma, K. Allinger, H. Y. Wang, D. Kiefer, S. Reinhardt, P. Hilz, K. Khrennikov, S. Karsch, X. Q. Yan, F. Krausz, T. Tajima, D. Habs, and J. Schreiber, “On the small divergence of laser-driven ion beams from nanometer thick foils,” *Physics of Plasmas*, vol. 20, no. 7, p. 73113, 2013.

- [96] B. Erdelyi, J. Maloney, and J. Nolen, “Symmetry-based design of fragment separator optics,” *Phys. Rev. ST Accel. Beams*, vol. 10, p. 64002, 6 2007.
- [97] J. Metzkes-Ng, F. E. Brack, F. Kroll, C. Bernert, S. Bock, E. Bodenstern, M. Brand, T. E. Cowan, R. Gebhardt, S. Hans, U. Helbig, F. Horst, J. Jansen, S. D. Kraft, M. Krause, E. Leßmann, S. Löck, J. Pawelke, T. Püschel, M. Reimold, M. Rehwald, C. Richter, H. P. Schlenvoigt, U. Schramm, M. Schürer, J. Seco, E. R. Szabó, M. E. Umlandt, K. Zeil, T. Ziegler, and E. Beyreuther, “The dresden platform is a research hub for ultra-high dose rate radiobiology,” *Scientific Reports 2023 13:1*, vol. 13, pp. 1–12, 11 2023.
- [98] K. Liu, T. Waldrop, E. Aguilar, N. Mims, D. Neill, A. Delahoussaye, Z. Li, D. Swanson, S. H. Lin, A. C. Koong, C. M. Taniguchi, B. W. Loo, D. Mitra, and E. Schüler, “Redefining FLASH Radiation Therapy: The Impact of Mean Dose Rate and Dose Per Pulse in the Gastrointestinal Tract,” *International Journal of Radiation Oncology*Biography*Physics*, 10 2024.
- [99] L. D. Geulig, L. Obst-Huebl, K. Nakamura, J. Bin, Q. Ji, S. Steinke, A. M. Snijders, J. H. Mao, E. A. Blakely, A. J. Gonsalves, S. Bulanov, J. Van Tilborg, C. B. Schroeder, C. G. Geddes, E. Esarey, M. Roth, and T. Schenkel, “Online charge measurement for petawatt laser-driven ion acceleration,” *Review of Scientific Instruments*, vol. 93, p. 103301, 10 2022.
- [100] S. Steinke, J. H. Bin, J. Park, Q. Ji, K. Nakamura, A. J. Gonsalves, S. S. Bulanov, M. Thévenet, C. Toth, J.-L. Vay, C. B. Schroeder, C. G. R. Geddes, E. Esarey, T. Schenkel, and W. P. Leemans, “Acceleration of high charge ion beams with achromatic divergence by petawatt laser pulses,” *Phys. Rev. Accel. Beams*, vol. 23, p. 21302, 2 2020.
- [101] K. Zeil, J. Metzkes, T. Kluge, M. Bussmann, T. E. Cowan, S. D. Kraft, R. Sauerbrey, and U. Schramm, “Direct observation of prompt pre-thermal laser ion sheath acceleration,” *Nature Communications 2012 3:1*, vol. 3, pp. 1–6, 6 2012.